Die approbierte Originalversion dieser Dissertation ist an der Hauptbibliothek der Technischen Universität Wien aufgestellt (http://www.ub.tuwien.ac.at).

The approved original version of this thesis is available at the main library of the Vienna University of Technology (http://www.ub.tuwien.ac.at/englweb/).

Dissertation

Grain Boundaries in High Temperature Superconductors

ausgeführt zum Zwecke der Erlangung
des akademischen Grades eines
Doktors der technischen Wissenschaften
unter der Leitung von

Univ.Prof. Dr.phil. Dr.h.c. Harald W. Weber

E141

Atominstitut der Österreichischen Universitäten
eingereicht an der Technischen Universität Wien
Fakultät für Physik

von

DI Karl Robert Schöppl
e9355291
Margaretengürtel 6/19
1050 Wien

Wien, Mai 2009

Contents

1 Theory **5**
- 1.1 Introduction . . . 5
- 1.2 Ginzburg Landau model . . . 6
  - 1.2.1 Critical fields . . . 6
  - 1.2.2 Isolated Abrikosov flux-line . . . 7
  - 1.2.3 Abrikosov flux-line lattice . . . 8
  - 1.2.4 Anisotropic GL description . . . 9
- 1.3 Lawrence Doniach model . . . 10
  - 1.3.1 Pancake vortices . . . 12
  - 1.3.2 Josephson vortices . . . 12
  - 1.3.3 Layered superconductors with Josephson coupling . . . 13
  - 1.3.4 Flux line pinning . . . 14
- 1.4 Low angle grain boundaries . . . 16

2 "Grain boundary" films **19**
- 2.1 Sample . . . 19
- 2.2 Transport measurements . . . 20
  - 2.2.1 Handling thin film samples . . . 20
  - 2.2.2 Mounting the sample . . . 21
  - 2.2.3 Transition temperature . . . 22
  - 2.2.4 Self field critical current . . . 23
  - 2.2.5 Rotational measurements . . . 25
  - 2.2.6 Grain boundary free track . . . 26
  - 2.2.7 Grain boundary tracks . . . 27
    - Grain boundary angle scaling . . . 28
    - Elastic single vortex model . . . 30
    - Numerical approach . . . 32
    - Alternative solution for the numerical approach . . . 33
    - Parametrisation . . . 36
    - Inclusion of the pinning force density . . . 38
    - Comparison with the numerical iteration . . . 40
    - Vortex breaking limit . . . 43
    - Evaluation of ϵ_1 . . . 46
    - Results and discussion . . . 50

Tables and figures of the evaluation results 52

3 Two axis probe **63**
3.1 Introduction 63
3.2 Initial design considerations 63
3.3 Current design 67
3.3.1 Top mount 67
3.3.2 Probe shaft 68
3.3.3 Goniometer head 68
3.3.4 Sample holder and spring loaded contacts 70
3.3.5 Goniometer geometry 74
3.3.6 Sample alignment and goniometer inconsistencies 75
3.3.7 Wiring 80
3.3.8 Stepper motors 81
3.3.9 Sample heater 81
3.3.10 Electrical grounding 82
3.3.11 Bearings 83
3.3.12 Hall probes 83
3.3.13 Measurement program 84
3.4 Measurement setup 85

Bibliography **86**

Abstract

The main goal of this work was to design and build a two axis goniometer for transport measurements that can be used at low temperatures and high magnetic fields. The goniometer should be used in a liquid He cooled gas flow cryostat equipped with a superconducting 6 T split coil magnet. With this kind of probe the sample can be oriented in any direction with respect to the applied magnetic field.

The probe is targeted to characterise the angular dependence of the critical current density of patterned high temperature superconducting thin films. It is well established that grain boundaries play a dominant role in limiting the transport critical currents in high temperature superconducting materials. Superconducting thin films grown on bi-crystalline substrates provide an isolated grain boundary with well defined misorientation angles and directions of the adjacent grains. Such samples in combination with a two axis probe allow detailed studies of the transport properties of a grain boundary in an applied magnetic field in dependence of the field direction and temperature. Effects like vortex channeling observable only on samples with high crystalline quality were of special interest in this work.

Transport measurements were performed on a 200 nm thick $YBa_2Cu_3O_{7-\delta}$ thin film grown by pulsed laser deposition on a 5° [001]-tilt grain boundary bi-crystal $SrTiO_3$ substrate. It was prepared at the Department of Material Science at the University of Cambridge.

The patterned thin film provided four 10 μm wide tracks crossing the grain boundary at angles of 90 °, 60 °, 45 ° and 30 °. One track, not crossing the grain boundary, was used to compare the intergrain and intragrain critical currents achieved. Besides the transition temperature and the self field critical current density at 77 K extensive angular dependent measurements were performed at temperatures from 40 K to 80 K and magnetic fields ranging from 1 to 6 T. The magnetic field was rotated in the *ab* plane of the sample. The symmetrical drop of the intergrain critical current density, when the field is aligned in the grain boundary plane, was observed on all grain

boundary tracks. An attempt was made to describe the angular dependence with an elastic single vortex model. Good agreement with the measured critical current densities was achieved.

Zusammenfassung

Der Hauptteil dieser Arbeit befasste sich mit der Planung und Umsetzung eines Zweiachsengoniometers für Transportstrommessungen. In einem bereits bestehenden Messaufbau, der aus einem, mit flüssig He gekühltem Gasflußkryostaten, besteht, welcher mit einer 6 T Helmholtzspule ausgestattet ist, ermöglicht dieser Probenstab eine beliebige Ausrichtung einer Probe im Magnetfeld.

Der Probenstab ist in erster Linie für Niederstrommessungen an supraleitenden Dünnfilmen ausgelegt. Der Stromtransport in Hochtemperatursupraleitern ist meist wesentlich durch Korngrenzen bestimmt. Biaxiale Dünnschichttechnologie erlaubt die Herstellung von isolierten und wohl definierten Korngrenzen. Sie sind hervorragend dazu geeignet, die Transporteigenschaften von Korngrenzen im Detail zu studieren. Ein Zweiachsengoniometer erlaubt die Untersuchung von winkelabhängingen Effekten wie "vortex channelling" bei verschiedenen Feldern und Temperaturen.

Die Tranportstrommessungen wurden an einer 200 nm dicken, strukturierten, $YBa_2Cu_3O_{7-\delta}$ Dünnschicht durchgeführt. Der Film wurde mit Hilfe von Laserablation auf einem 5° [001]-verkippten $SrTiO_3$ Korngrenzensubstrat gezüchtet. Diese Probe wurde am Institut für Materialforschung an der Universtität Cambridge hergestellt.

Der strukturierte Film hatte vier 10 μm breite Stege, welche die Korngrenze in den Winkeln 90°, 60°, 45° und 30° kreuzten. Ein weiterer Steg, welcher nicht über die Korngrenze verlief, wurde zum Vergleich der gemessenen Stromdichten an den Krongrenzen herangezogen. Neben der Sprungtemperatur und der kritischen Stromdichte im Selbstfeld bei 77 K wurden Rotationsmessungen bei Temperaturen von 40 K bis 80 K und Magnetfeldern von 1 bis 6 T gemessen. Das Feld wurde parallel zu den *ab* Ebenen der Dünnschicht rotiert. Das symmetrische Einbrechen der kritischen Stromdichte, wenn das Feld parallel zur Korngrenzenebene ausgerichtet ist, wurde an allen Stegen mit Korngrenze festgestellt. Es wurde versucht, die gemessene Winkelabhängigkeit mit einem Flusslinienmodell, welches die

Elastizität einer einzelnen Flusslinie berücksichtigt, zu beschreiben. Die gemessene Winkelabhängigkeit stimmt gut mit dem Modell überein.

Chapter 1

Theory

1.1 Introduction

The superconducting state is usually characterised by zero electrical resistance and by perfect diamagnetism of the superconducting material. The transition from normal conducting to superconducting behaviour takes place at a material dependent *transition temperature* T_c and it is a true thermodynamic transition. In *type-I superconductors* the magnetic flux penetrates only a thin surface layer of thickness λ (*magnetic penetration depth*) and the inner stays field free ("Meisser state"). Electrical transport currents are restricted to this surface layer. Above a *thermodynamic critical field* H_c the material becomes normal conducting.

High-T_c superconductors and also application relevant low-T_c materials are *type-II superconductors*. They exhibit a different behaviour, because they allow a partial penetration of magnetic flux in the form of flux-lines and transport currents can flow over the whole cross section of a sample. Flux-lines carry a magnetic flux density of $\Phi_0 = h/2e = 2.07 \cdot 10^{-15}\,\mathrm{Wb}$. Without pinning they can move freely in the material, which leads to energy losses in combination with transport currents, implying a non zero resistance. There are two critical fields, H_{c1} and H_{c2}. Below H_{c1} a type-II superconductor is in the Meissner state and behaves like a type-I superconductor. Between H_{c1} and H_{c2} flux-lines appear ("mixed state") and above H_{c2} the material is normal conducting.

The investigation and understanding of the flux-line behaviour is a central topic in superconductivity research.

1.2 Ginzburg Landau model

The Ginzburg Landau (GL) theory is a phenomenological model. It is based on the Landau theory for phase transitions of the second order and, therefore, is only valid near the superconducting transition. It allows a spatial description of the superconducting phase. The GL theory introduces a complex order parameter $\Psi(\boldsymbol{r}) = |\Psi(\boldsymbol{r})|\, e^{i\varphi(r)}$, where $|\Psi(\boldsymbol{r})|^2$ represents the density of the superconducting charge carriers (*Cooper pairs*). The free energy density difference between the superconducting and normal conducting state ($\Delta f = f_\mathrm{s} - f_\mathrm{n}$) is postulated as a series expansion of the form

$$\begin{aligned} \Delta f(\boldsymbol{A}, \Psi(\boldsymbol{r}), \boldsymbol{r}) &= \alpha(T)\,|\Psi(\boldsymbol{r})|^2 + \frac{\beta(T)}{2}\,|\Psi(\boldsymbol{r})|^4 \\ &+ \frac{\hbar^2}{4\,m}\left|(i\nabla + \frac{2e}{\hbar}\,\boldsymbol{A})\Psi(\boldsymbol{r})\right|^2 + \frac{\mu_0 H^2}{2}. \end{aligned} \tag{1.1}$$

The first two terms describe the second order phase transition, the next term represent the kinetic energy of the super-currents and the last term takes the magnetic energy density into account. $\boldsymbol{A}$ is the vector potential ($\boldsymbol{B} = \nabla \times \boldsymbol{A}$), m is the effective electron mass and e is the electron charge. A variation of Δf with respect to $\boldsymbol{A}$ and $\Psi(\boldsymbol{r})$ leads to the GL differential equations.

The GL theory introduces two characteristic length scales, *the magnetic penetration depth* λ and the *coherence length* ξ. λ determines how far the magnetic field can penetrate the superconductor at a normal-superconducting interface and ξ gives the length scale for the decay of the disturbance of the order parameter. The ratio $\kappa = \lambda/\xi$ is the *GL parameter* and its value determines the behaviour of the superconductor. For $\kappa < 1/\sqrt{2}$ the domain wall energy is positive and the superconductor is of type-I. In type-II superconductors the domain wall energy is negative and $\kappa > 1/\sqrt{2}$.

1.2.1 Critical fields

Within GL theory the critical fields for an isotropic superconductor are [4]

$$H_{\mathrm{c1}} \approx \frac{\Phi_0}{4\pi\mu_0\lambda^2}(\ln\kappa + 0.5), \quad H_\mathrm{c} = \frac{\Phi_0}{2\sqrt{2}\pi\mu_0\xi\lambda}, \quad H_{\mathrm{c2}} = \frac{\Phi_0}{2\pi\mu_0\xi^2} = \sqrt{2}\kappa H_\mathrm{c}\,. \tag{1.2}$$

The thermodynamic critical field H_c is defined by the condensation energy $\mu_0 H_c^2/2$. At $H = H_{c1}$ the Gibbs free energy of the superconductor without a vortex and with one vortex has to be equal, so flux lines can penetrate. H_{c1} is therefore connected with the self-energy of a single vortex, more exactly with the *free energy per unit length* ϵ_l

$$H_{c1} = \frac{\epsilon_l}{\Phi_0}\,. \tag{1.3}$$

The self-energy derived from (1.2) would be $L\Phi_0 H_{c1} = L(\Phi_0^2/4\pi\mu_0\lambda^2)(\ln\kappa + 0.5)$ and represents the general result for a curved flux-line with length L. The calculation for a straight flux-line, applying the modified London equation, results in $\epsilon_l = (\Phi_0^2/4\pi\mu_0\lambda^2)\ln\kappa$.

The GL parameter κ enters the relation between the upper critical field H_{c2} (field of first nucleation of the superconducting phase in the bulk) and the thermodynamical critical field H_c, $H_{c2} = \sqrt{2}\,\kappa\, H_c$. In a type-I superconductor $H_{c2} < H_c$ and the superconductor can be "supercooled" below H_c, where the order parameter jumps irreversibly to its bulk value (first order phase transition below T_c). In type-II superconductors $H_{c2} > H_c$ and $|\Psi(\boldsymbol{r})|^2$ sets in continuously at H_{c2} (second order phase transition below T_c).

1.2.2 Isolated Abrikosov flux-line

In the centre of an Abrikosov vortex the order parameter is suppressed. Therefore, ξ gives a measure for the core radius and λ for the distance of the decay of the circulating shielding currents around the core.

The general GL solution for the order parameter and the field of an isolated flux-line can only be achieved numerically. Outside the core the order parameter is nearly constant. In the extreme type-II limit ($\kappa \gg 1$) the core radius is far smaller than the vortex radius and over most of the vortex the superconductor will act like an ordinary London superconductor. As long as the vortex cores do not overlap, the London theory can be applied (for $H < 0.2H_{c2}$ and $\mu_0 H_{c2} \approx 100\,\mathrm{T}$ in YBCO) [4]. A single Abrikosov vortex can be described by the *modified London equation* [23]

$$\lambda^2 \nabla \times \boldsymbol{J} + \boldsymbol{H} = \boldsymbol{e}\frac{1}{\mu_0}\,\Phi_0\delta_2(\boldsymbol{r})\,. \tag{1.4}$$

The inhomogeneity at the right hand side accounts for the magnetic flux in the core at the position $\boldsymbol{r}$. It is found, that the field in the flux-line centre is roughly twice the

lower critical field, and the maximum vortex current is the depairing current [4].

1.2.3 Abrikosov flux-line lattice

Considerating about the interaction energy for two well separated straight vortices (no core interaction, one vortex feels just the field of the other) at the positions $\boldsymbol{r_1}$ and $\boldsymbol{r_2}$ leads to the result [23]

$$\boldsymbol{f_2} = \boldsymbol{J_1}(\boldsymbol{r_1}) \times \hat{\boldsymbol{e}}\Phi_0 \,, \tag{1.5}$$

where $\boldsymbol{f_2}$ is the *Lorenz force per unit length* felt by the second vortex and $\hat{\boldsymbol{e}}$ is the unit vector in the field direction. This can be generalised to

$$\boldsymbol{f} = \boldsymbol{J} \times \hat{\boldsymbol{e}}\Phi_0 \,, \tag{1.6}$$

where $\boldsymbol{J}$ is the total super-current density at the location at the core of the vortex in question. An implication of this result is, that a flux-line can be in static equilibrium at a given position only if the super-fluid velocity from all sources is zero there. This can be accomplished if the vortex is surrounded by a symmetrical array of other vortices. It turns out, that in a homogeneous superconductor the regular hexagonal lattice configuration has the lowest energy. The *vortex lattice constant* for the hexagonal lattice is

$$a_{\mathrm{hex}} = \left(\frac{4}{3}\right)^{1/4} \left(\frac{\Phi_0}{B}\right)^{1/2} \,. \tag{1.7}$$

In a general expression for the GL interaction energy of an arbitrary arrangement of flux lines one has to sum over the contributions of each vortex. The contribution splits up into two terms, a repulsive magnetic interaction (overlap of magnetic vortex fields) and an attractive condensation-energy term (overlap of the vortex cores). The core interaction is attractive, because one vortex can save condensation energy due to the suppressed order parameter in the second core [5]. The magnetic interaction has the same spatial dependence as the field of an isolated vortex. It decays exponentially $\propto r_{12}^{-1/2} e^{-\boldsymbol{r}_{12}/\lambda}$ for large distances from the core and varies logarithmically at small distances. The magnetic field of arbitrary vortex arrangements for $\kappa \gg 1$ and $H \ll H_{c2}$ is a linear superposition of the isolated vortex fields [4].

1.2.4 Anisotropic GL description

The GL free energy equation for anisotropic superconductors is

$$\begin{aligned} \Delta f(\boldsymbol{A}, \Psi(\boldsymbol{r}), \boldsymbol{r}) &= \alpha(T)\,|\Psi(\boldsymbol{r})|^2 + \frac{\beta(T)}{2}\,|\Psi(\boldsymbol{r})|^4 + \frac{\hbar^2}{4\,m_{\mathrm{ab}}}\left|(i\nabla_{||} + \frac{2e}{\hbar}\,\boldsymbol{A}_{||})\Psi(\boldsymbol{r})\right|^2 \\ &+ \frac{\hbar^2}{4\,m_{\mathrm{c}}}\left|(i\nabla_{\perp} + \frac{2e}{\hbar}\,\boldsymbol{A}_{\perp})\Psi(\boldsymbol{r})\right|^2 + \frac{B^2}{2\,\mu_0}. \end{aligned} \tag{1.8}$$

Here a uni-axial symmetry along the c crystal axis is assumed which represents the most common case of anisotropic superconductors. In equilibrium, the order parameter is $\Psi_0 = \sqrt{|\alpha|/\beta}$ with $\alpha(T) \propto (T - T_{\mathrm{c}})$ [13]. Especially in high-T_{c} superconductors the weak anisotropy between the a and b direction is usually neglected. m_{ab} and m_{c} are the effective electron masses in the ab planes and the c direction, respectively. Assuming the crystal c axis to be aligned with the z coordinate, $\boldsymbol{A}_{||} = (A_{\mathrm{x}}, A_{\mathrm{y}}, 0)$ and $\nabla_{||} = (\nabla_{\mathrm{x}}, \nabla_{\mathrm{y}}, 0)$. The isotropic GL free energy equation is obtained by setting $m = m_{\mathrm{ab}} = m_{\mathrm{c}}$. The anisotropy parameter γ is defined as $\gamma = \sqrt{m_{\mathrm{c}}/m_{\mathrm{ab}}}$. For high temperature superconductors $m_{\mathrm{c}} > m_{\mathrm{ab}}$ and therefore $\gamma > 1$. γ ranges from 5 to 7 in YBCO.

The mass anisotropy causes the coherence length ξ to be different in c and ab direction. The isotropic thermodynamic critical field in (1.2) transfers this anisotropy inversely proportionally to the penetration depth λ. For a uni-axial material ξ_{ab} and ξ_{c} are the coherence lengths in the ab and the c crystal directions, respectively ($\xi_{\mathrm{ab}}(0) \approx 1.6\,\mathrm{nm}$ in YBCO, [24]). λ_{ab} is the penetration depth referring to the shielding currents in the ab planes ($H||c$) and λ_{c} refers to the currents in c direction ($H||ab$). An Abrikosov vortex aligned with the c axis has a circular "cross section" with a core radius of ξ_{ab} and a flux penetration radius of λ_{ab} corresponding to shielding currents in the ab planes. These two length scales correspond to ξ and λ of an isotropic material. When tilting the vortex away from the c axis, m_{c} and the (weaker) shielding currents flowing in c direction come into play decreasing the core dimension in the vortex-c axis plane and increasing the field penetration along the ab planes resulting in an ellipticly "cross section".

The anisotropy γ and the GL parameter κ fulfil the following relations

$$\gamma = \sqrt{\frac{m_{\mathrm{c}}}{m_{\mathrm{ab}}}} = \frac{\xi_{\mathrm{ab}}}{\xi_{\mathrm{c}}} = \frac{\lambda_{\mathrm{c}}}{\lambda_{\mathrm{ab}}} \tag{1.9}$$

$$\kappa^{c} = \frac{\lambda_{ab}}{\xi_{ab}} \quad \kappa^{ab} = \sqrt{\frac{\lambda_{ab}\,\lambda_{c}}{\xi_{ab}\,\xi_{c}}}, \tag{1.10}$$

so that $\kappa^{ab} = \gamma\kappa^{c}$. κ^{c} is about 100 in YBCO.

The rescaling approach suggested in [2] allows to deduce anisotropic properties of the flux lattice from the isotropic results. By rescaling the coordinates, the vector potential and the magnetic field

$$\tilde{\boldsymbol{r}} = (x, y, \gamma z) \quad \tilde{\boldsymbol{A}} = (A_x, A_y, A_z/\gamma) \quad \tilde{\boldsymbol{B}} = (B_x/\gamma, B_y/\gamma, B_z)\,, \tag{1.11}$$

the two gauge invariant derivative terms in (1.8) can be rewritten in a single isotropic term. This transformation transfers the anisotropy γ to the magnetic energy terms. If the flux density is large enough ($B \gg \mu_0 H_{c1}$) the vortices overlap sufficiently and the spatial modulation of the local $\boldsymbol{B}$ can be neglected. The macroscopic magnetic energy can be computed by using the average field which defines the average density of vortices. On the basis of these arguments a scaling rule is obtained [2], [23]

$$Q(\vartheta, H, T, \xi_{ab}, \lambda_{ab}, \gamma, \delta) = s_Q\, \tilde{Q}(\varepsilon_\vartheta H, \gamma T, \xi_{ab}, \lambda_{ab}, \gamma\delta)\,, \tag{1.12}$$

where ϑ is the angle between the field and the *ab* plane and δ is the scalar disorder strength. Q is the desired anisotropic quantity for which the isotropic result $\tilde{Q}$ is already known. $\varepsilon_\vartheta = \sqrt{\gamma^{-2}\cos^2\vartheta + \sin^2\vartheta}$ and the prefactor s_Q depend on the quantity in question. For volume, energy, temperature and action $s_Q = 1/\gamma$, whereas for the magnetic field $s_Q = 1/\varepsilon_\vartheta$. This anisotropic rescaling can only be applied to layered superconductors, when the discreteness of the layered structure is not important (three dimensional behaviour).

1.3 Lawrence Doniach model

A very useful phenomenological model for layered superconductors is the one proposed by Lawrence and Doniach (LD). The layered superconductor is viewed as a stack of two dimensional superconductors (within each of which the GL order parameter $\Psi_n(x, y)$ is a two dimensional function), coupled together by Josephson tunnelling between adjacent layers. As appropriate for the high temperature superconductors, the superconducting layers are associated with the crystallographic *ab* planes (CuO_2 planes) with the *c* axis perpendicular to them. The z coordinate is

taken along c, s is the inter-planar distance and x, y are the coordinates in the planes. The LD free energy is given by

$$\begin{aligned} F(\boldsymbol{A}(\boldsymbol{r}), \Psi_{\mathrm{n}}(\boldsymbol{r}_\perp)) &= s\sum_n \int \mathrm{d}^2 r_\perp \Big[\alpha(T)\,|\Psi_{\mathrm{n}}|^2 + \frac{\beta(T)}{2}\,|\Psi_{\mathrm{n}}|^4 + f_{\mathrm{J}}\,\Big|(i\nabla_{||} + \frac{2e}{\hbar}\,\boldsymbol{A}_{||})\Psi_{\mathrm{n}}\Big|^2 \\ &\quad + \frac{\hbar^2}{4\,m_{\mathrm{c}}\,s^2}\,\Big|\Psi_{\mathrm{n+1}} - \Psi_{\mathrm{n}}\,e^{iI_n}\Big|^2\Big] + \int \frac{B^2}{2\,\mu_0}\mathrm{d}r \qquad (1.13) \\ \text{with} \quad I_{\mathrm{n}}(\boldsymbol{r}_\perp) &= \frac{2e}{\hbar}\int_{ns}^{ns+s} A_{\mathrm{z}}(\boldsymbol{r})\mathrm{d}z \approx \frac{2e}{\hbar} s A_{\mathrm{z}}(\boldsymbol{r}_\perp), ns) \quad \text{if } s \ll \lambda\,, \end{aligned}$$

where $\boldsymbol{r}_\perp = (x, y)$, n is the layer index, $ns = z_n$, α and β are the usual GL coefficients, m_{ab} and m_{c} are the effective masses of Cooper pairs moving in the ab-plane or along c. $\boldsymbol{A}$ is the vector potential where $\boldsymbol{A}_{||} = (A_{\mathrm{x}}, A_{\mathrm{y}}, 0)$, $A_{\mathrm{z}} = \boldsymbol{A}\,\hat{\boldsymbol{z}}$ and $\nabla_{||} = (\frac{\partial}{\partial x}, \frac{\partial}{\partial y}, 0)$.

One has $\xi_{\mathrm{ab}}^2 = \hbar^2/2m_{\mathrm{ab}}\alpha$, $\xi_{\mathrm{c}}^2 = \hbar^2/2m_{\mathrm{c}}\alpha$, $\lambda_{\mathrm{ab}}^2 = m_{\mathrm{ab}}\beta/4\mu_0 e^2\alpha$, $\lambda_{\mathrm{c}}^2 = m_{\mathrm{c}}\beta/4\mu_0 e^2\alpha$, and the anisotropy $\gamma = m_{\mathrm{c}}/m_{\mathrm{ab}} = \sqrt{\lambda_{\mathrm{c}}/\lambda_{\mathrm{ab}}} = \sqrt{\xi_{\mathrm{ab}}/\xi_{\mathrm{c}}} > 1$. The coupling between the superconducting planes is determined by the prefactor of the difference $f_{\mathrm{J}} = \frac{\hbar^2}{4\,m_{\mathrm{ab}}} = \hbar^2/4\,m_{\mathrm{c}}\,s^2$. A new characteristic length scale is introduced, the *Josephson penetration length*

$$\lambda_{\mathrm{J}} = \gamma s\,. \qquad (1.14)$$

For $\xi_{\mathrm{c}} \gg s$ ($\lambda_{\mathrm{J}} \gg \xi_{\mathrm{ab}}$) the difference in (1.14) may be replaced by the gradient $(i\frac{\partial}{\partial z} + \frac{2e}{\hbar}A_{\mathrm{z}})\Psi(\boldsymbol{r})$, and the anisotropic GL theory is recovered. Because $\xi \to \infty$ ($\alpha \propto T - T_{\mathrm{c}}$) for $T \to T_{\mathrm{c}}$ this limit is always realised close to T_{c}. In the opposite limit, $\xi_{\mathrm{c}} \ll s$ ($\lambda_{\mathrm{J}} \ll \xi_{\mathrm{ab}}$) (1.14) describes weakly Josephson coupled superconducting layers. In this regime the vortices are built up of stacks of two dimensional pancake vortices in the superconducting layers connected by Josephson vortex strings.

The crossover between the two dimensional and the three dimensional description occurs at a temperature T_{cr}. This temperature is defined by

$$\xi_{\mathrm{ab}}(T_{cr}) = \frac{\lambda_{\mathrm{J}}}{\sqrt{2}}\,, \qquad (1.15)$$

which is equivalent to $\xi_{\mathrm{c}}(T_{cr}) = s/\sqrt{2}$. The crossover takes place if the parameter

$$\rho = \frac{2\xi_{\mathrm{ab}}^2(0)}{\gamma^2 s^2} = \frac{\xi_{\mathrm{ab}}^2(0)}{\xi_{\mathrm{ab}}^2(T_{cr})} \qquad (1.16)$$

is less than one, $\rho < 1$. With the GL temperature dependence of $\xi_{\mathrm{ab}}(T)$ ($\alpha(T) \propto (T - T_{\mathrm{c}})$) the crossover temperature can be expressed as $T_{cr} = T_{\mathrm{c}}(1 - \rho)$. $\rho \approx 0.1$ for

YBCO, which results in $T_{cr} \approx 80\,\mathrm{K}$ [13].

1.3.1 Pancake vortices

For strongly anisotropic high temperature superconductors, like Bi-2212 or artificial multilayers, the electronic coupling (Josephson coupling) of the layers can be neglected. The shielding super-currents of the vortices are restricted to the superconducting layers resulting in isolated *point vortices* or *pancake vortices* in the layers. A pancake vortex has a dipole like field which extends to a distance of the order of λ_{ab} in z-direction. Due to the symmetry of the field distribution created by each vortex, any configuration of point vortices creates a field parallel to the c-axis. The magnetic flux contribution of one point vortex is $\ll \Phi_0$, only the sum of the flux contributions along a stack of pancake vortices yields Φ_0. Point vortices in the same layer repel each other, and those in different layers attract each other, which favours their stack like arrangement. Pancake vortices in different layers interact exclusively via their magnetic field created in the inter-layer space. The interaction energy of a vortex stack is logarithmic up to arbitrary large distances R, in contrast to point vortices in an isolated thin film, where the interaction varies like $1/R$ for $R > \lambda_{ab}^2/d$ (d is the film thickness) [4], [13].

In the case of a tilted field, the field component parallel to the layers cannot be screened in absence of Josephson currents. Only the normal component of the field, H_z, generates an Abrikosov lattice of 2D vortex stacks perpendicular to the layers. The vortices do not tilt and the superconducting properties only depend on the normal field H_z [18]. Deviations occur close to the layer direction and reflect a weak electronic inter-layer coupling [13].

1.3.2 Josephson vortices

When the applied field is nearly along the *ab*-plane, the vortex core prefers to run between the superconducting layers [4]. When the coupling between the layers is weak, the vortex lines along the *ab*-planes are *Josephson vortices* or *Josephson strings*. They do not have a normal conducting vortex core like Abrikosov vortices because the order parameter is zero between the layers anyway. The dimension of the vortex core is given by the Josephson length, $\lambda_J = \gamma s$, in *ab* direction and by the layer spacing s in the c direction. The aspect ratio of the Josephson core, $\lambda_J/s = \gamma = \xi_{ab}/\xi_c$, is the same as for a 3D anisotropic Abrikosov vortex along the *ab*-planes.

If two pancake vortices in adjacent layers are shifted by more than a distance λ_J, a Josephson vortex will form [7].

1.3.3 Layered superconductors with Josephson coupling

For the formation of tilted vortices in layered superconductors, inter-layer Josephson currents are required. At sufficiently high fields the vortices build up tilted stacks of 2D vortices situated at the superconducting layers and aligned along the direction of the field. The pancakes are connected by Josephson strings between the layers. The vortex core structure is complex and strongly depends on the tilt angle of the field. Relevant length scales of the problem are the normal core size ξ_{ab}, the Josephson length λ_J and the horizontal shift between two adjacent pancake vortices, $s \tan\theta$, where θ is the angle between the field direction and the c axis. In contrast to a three dimensional London model the inter-layer currents are limited by the *Josephson critical current*

$$J_{c,J} = \frac{\Phi_0}{2\pi\mu_0\lambda_c^2 s}. \tag{1.17}$$

At length scales larger $\min(s\tan\theta, \lambda_J)$ away from the normal cores of the 2D vortices, the 3D London inter-layer current is smaller than $J_{c,J}$ and the 3D London model applies. Between this outer border and the normal cores the vortex can be described by a 2D London model with purely electromagnetic interaction between 2D pancakes. Three different angular regimes can be distinguished for the vortex core structure:

- $\tan\theta < \xi_{ab}/s$: The 2D vortex cores strongly overlap and the 3D London model is valid everywhere outside the normal cores.
- $\xi_{ab}/s \leq \tan\theta < \gamma$: The 2D vortex cores are displaced by more than their width, but not enough to leave room to strings of Josephson cores joining them. Two adjacent 2D vortices lie in one single 2D London region.
- $\gamma \leq \tan\theta$: Here $s\tan\theta > \lambda_J$ and Josephson strings develop joining 2D vortices. The cores of the vortex lines take a "staircase" form. When the field is tilted in the xz plane, the dimension of the internal boundary of the 3D London region is λ_J in y direction and $s\tan\theta$ in x direction. The 2D London regions are situated in circles of diameter λ_J around the 2D vortices and between the circles lies a Josephson string.

At low fields well above H_{c1} the vortex lattice follows the 3D London model. Flux lines are nearly aligned with the applied field and form a distorted hexagonal

lattice (without pinning). For $\tan\theta \ll \gamma$, the intra-layer interaction of point vortices is dominant and the pancake vortices in one layer are arranged in a regular triangular lattice, which is shifted from one layer to the next to line up the pancake vortices with the field direction. A cut through a bundle of seven adjacent vortices perpendicular to the field direction gives a hexagon, squeezed in the direction of the tilt plane.

The vortex lattice in layered superconductors exhibits a large variety of different structures because of this complex core structure. When the magnetic field is exactly parallel to the layers, a stretched triangular lattice of Josephson vortices appears. At a field

$$\mu_0 H_0 = \frac{\Phi_0}{2\pi s^2 \gamma} = \frac{\Phi_0}{2\pi s \lambda_J} \tag{1.18}$$

all inter-layer spacings are occupied by Josephson vortex nuclei. For $H \ll H_0$ one obtains a distorted Abrikosov lattice of Josephson vortices situated between the superconducting layers with a core section of γs^2. This refers to the "lock-in" state of the vortex lattice.

The tilted vortex state out of a "locked-in" vortex lattice takes place by forming vortex kinks. These are connections of Josephson vortices across two adjacent layers by Abrikosov vortex pieces. Because this kink-mediated penetration of H_z only takes place, if $\lambda_{ab} > \lambda_J$, one can find a *critical anisotropy* γ_{cr}

$$\gamma_{cr} = 1.95\,\lambda_{ab}/s\,, \tag{1.19}$$

where for $\gamma > \gamma_{cr}$ a "combined lattice" instead of a kinked vortex lattice is expected [6]. In this configuration parallel and perpendicular vortices coexist. [19] also points out that at small kink densities the kinks will align along the z direction in "kink chains", which again form "kink walls" due to their mutual interaction.

In the combined lattice in highly anisotropic materials the weak interaction between pancake stacks and Josephson vortices should result in more complex vortex configurations [20]. As this is not expected to be the case in YBCO, it will not be discussed further.

1.3.4 Flux line pinning

In the presence of vortices with their magnetic induction $\boldsymbol{B} = \mu_0 \boldsymbol{H} = n_v \Phi_0$, a current density J causes a Lorentz force per volume

$$\boldsymbol{F}_{LF} = \boldsymbol{J} \times \boldsymbol{B} \tag{1.20}$$

on the vortex lattice. n_v is the vortex area density B/Φ_0. If there is no pinning force, holding the vortices in place, they will start to move. With a drift velocity v_F of the vortex lines and considering the dissipative power density $\boldsymbol{J} \cdot \boldsymbol{E} = \boldsymbol{F}_{LF} \cdot \boldsymbol{v}_F$ an electric field $\boldsymbol{E}$ is set up

$$\boldsymbol{E} = \boldsymbol{B} \times \boldsymbol{v}_F \,. \tag{1.21}$$

The only opposing force to the Lorentz force in this idealised *free flux flow* without pinning is an assumed viscous force per unit length proportional to v_F. The losses resulting only from moving the vortex lines through the superconductor, are represented by a *flux flow resistivity* ρ_{ff}. It was shown, that a simple relationship between the ρ_{ff} and the normal conducting resistivity ρ_n holds[23],

$$\frac{\rho_{ff}}{\rho_n} \approx \frac{B}{B_{c2}} \,. \tag{1.22}$$

Therefore ρ_{ff} depends linearly on the magnetic field and is constant. The flux flow IV curve, corresponding to $E = \rho_{ff} J$, for the zero pinning case is a straight line through the origin. With pinning the Lorentz force has to overcome the pinning force before flux flow can set in. This shifts the straight flux flow current-voltage (IV) response to larger current densities. The J value, where the straight IV curve cuts the zero voltage axis, is defined as the critical current density J_c. So far no thermal activation of the flux lines has been considered.

IV curves from transport measurements in HTSC do not show such a straight increase of voltage setting in sharply at the critical current density. The voltage sets in more slowly and curved because of thermally activated depinning of vortex lines already below the critical current density. This *flux creep* is described to thermally activated jumps of vortices or bundles of vortices over an energy barrier $U = U(J/Jc, B, T)$. The probability for a jump is $\propto e^{-U/k_B T}$ and the energy barrier vanishes at the critical current density. Without an applied current density the thermally activated vortex jumps do not result in a netto drift of magnetic flux and therefore no electrical field is observed. A Lorentz force favours hops in the direction of the force, i.e. it decreases the energy barrier in the f_{LF} direction and increases it for jumps in the opposite direction. The electrical field is proportional to the difference in the jump rates [23]. At $J \approx J_c$ the jump rate opposite to the Lorentz force can be neglected. Using a phenomenological activation barrier, $U(J) = U_0 \ln(J_c/J)$ [1], the electrical field is given by

$$E \propto \left(\frac{J}{J_c}\right)^n \,. \tag{1.23}$$

There are two mechanisms explaining the effectivity of defects acting as pinning centres. The first assumes, that the order parameter is reduced or suppressed at the defect by the disturbance in the superconducting material. A vortex can avoid its loss of the condensation energy when its core is located at the defect. The second mechanism of pinning is due to the scattering of quasi-particles by the defect [22]. A scattering centre helps a superconductor to sustain deformations of the order parameter up to distances of the order of the zero temperature coherence length $\xi(0)$. Hence, it is energetically advantageous for a region, where the order parameter varies strongly, like in a vortex core, to coincide with a scattering centre.

In YBCO single crystals the pinning is predominantly due to randomly distributed small defects. In thin films the pinning is stronger and dominated by correlated defects like twin-plains, anti-phase boundaries, dislocations and surface features.

1.4 Low angle grain boundaries

The behaviour of grain boundaries in HTSC strongly depends on the misorientation angle between adjoining superconducting grains. High angle grain boundaries ($> 10^{\circ}$ misorientation) (HAGB) generally show a low critical current and a current voltage characteristic exhibiting Josephson-coupled behaviour. Low angle grain boundaries ($< 10^{\circ}$ misorientation) (LAGB) provide a strong coupling of adjacent grains, although the observed intergrain critical current density is usually lower than the intragrain J_c.

To investigate the basic properties of the grain boundary interfaces, the bi-crystal technology was invented. It allows single, well defined grain boundaries to be fabricated and analysed in thin films samples. The measurements presented in this work were performed on a 5° $[001]$-tilt grain boundary grown on $SrTiO_3$. This means, that the misorientation angle is 5° and the $[001]$ crystal direction, is shared by both grains. "Tilt" is used to refer to a rotation around an axis in the plane of the grain boundary and "twist" to a rotation of the crystal grains around the axis perpendicular to the grain boundary plane. In the grain boundary used in this work, both grains are *c* axis oriented thin films, where the *ab* planes are misaligned (symmetrically) by 5°.

On an atomic level the LAGB is formed by adding atomic layers in the grain boundary plane resulting in edge dislocations. The length of the *Burgers vector* $\boldsymbol{b}$, measured in a transmission electron microscope (TEM) on a 10° $[001] - tilt$ LAGB,

was found to be 0.38 nm [10]. It is connected, by Frank's formula $D = |\boldsymbol{b}|/2\sin(\theta/2)$, with the *dislocation distance* D and the misorientation angle θ [17]. It was concluded from TEM investigations of grain boundaries in HTSCs that the observed reduced current densities do not result from the coarse defects in the grain boundaries, such as voids or impurity layers. High- and low angle grain boundaries showed a clean and well defined structure, where the grains appear unaltered right up to the boundary. At larger θ, the distance between the dislocations decreases and the separate dislocations found in LAGB merge in a continuous interface layer typical for HAGB weak links.

Around the dislocation cores the superconducting order parameter is suppressed. The non-superconducting core regions can result from local compositional and hole concentration variations, additional electron scattering and significant strains near the dislocation cores [15]. At least for LAGB the decrease of the critical current across the grain boundary can be explained by the reduction of the superconducting cross section.

The non superconducting dislocation cores have an effective radius of the order of $\approx 1\,\text{nm}$. This is comparable to the zero temperature coherence length in YBCO and therefore the dislocation cores can act as pinning centres [8].

The current voltage response of a LAGB is determined by the flow of vortices along the grain boundary [17], [9]. The IV curves measured across a LAGB show a linear rise of the voltage. For an applied magnetic field perpendicular to the plane of the thin film ($H||c$) and parallel to the grain boundary plane Abrikosov vortices are pinned by the dislocation cores. If J ($\boldsymbol{J} \perp H$) is in excess of the critical current density, a narrow line of vortices in the LAGB moves in response to the Lorentz force along the grain boundary (*flux channelling*). The voltage is generated over a short distance of the order of the vortex lattice spacing around the boundary resulting in very high electric fields. In [9] it was assumed that only a single row of vortices moves. The relation (1.22) could be confirmed and the derived upper critical fields were in good agreement with the expected values.

From the electric field derived in [9] it was concluded, that only a single row of vortices move along the grain boundary. In a strongly coupled LAGB the vortex lattice in the grains is not much disturbed by the grain boundary and dislocation cores should be effective pinning centres for Abrikosov vortices. Therefore it is not clear, why Abrikosov vortices should slip in a single row along the grain boundary. In [14] it was pointed out, that due to defects in the material a decrease of the depairing current density to values still above than the intragrain J_c will have an effect on

the vortex cores. So even if the LAGB does not directly limit the intergrain J_c by decoupling the grains, the core structure of vortices located in the grain boundary will be changed. Considering a planar defect with a reduced current density in the direction perpendicular to the plane it was shown, that the length of the vortex core along the defect becomes much larger than the unchanged core size, ξ, in the transversal direction. Therefore the effectivity of pinning centres will be reduced for the direction parallel to the defect plane. These modified vortices are called *Abrikosov-Josephson vortices*.

Chapter 2

"Grain boundary" films

2.1 Sample

The sample was a 200 nm thick $YBa_2Cu_3O_{7-\delta}$ thin film grown by pulsed laser deposition on a 5° [001]-tilt grain boundary bi-crystal $SrTiO_3$ substrate. The dimensions of the substrate and, therefore, of the the sample are approximately 5×10 mm. The film was patterned by photo-lithography and Ar ion milling. A layer of Ag followed by a layer of Au were sputtered onto the film surface to form the contacts [11].

Fig. 2.1 shows on the left a photograph of the middle part of the sample. The photograph was taken with an optical microscope at a magnification of 50:1. The grain boundary is vertical and marked by a dashed line. The dark stripes are $YBa_2Cu_3O_{7-\delta}$. The pattern provides 10 μm wide tracks which connect the thick horizontal bars ending at the contact pads. There are three vertical tracks parallel to the grain boundary which could be used to obtain the intragrain J_c and four tracks traversing the grain boundary. The tracks can be seen more clearly in the sketch provided on the right. The tracks are numbered from 1 to 7. For the measurements presented in this work only the grain boundary tracks 1 to 4 and one track not crossing the grain boundary, track 5, were used. The tracks numbered from 1 to 4 form an angle of 90°, 60°, 45° and 30°, respectively, with respect to the grain boundary. This angle is the *grain*

Reference	a	b	c	d	e	f	g
d in mm	0.175	0.200	0.251	0.350	0.238	0.109	0.230

Table 2.1: *Distance of the voltage contacts d. The letters refer to the dimensions in the track outline in Figure 2.1.*

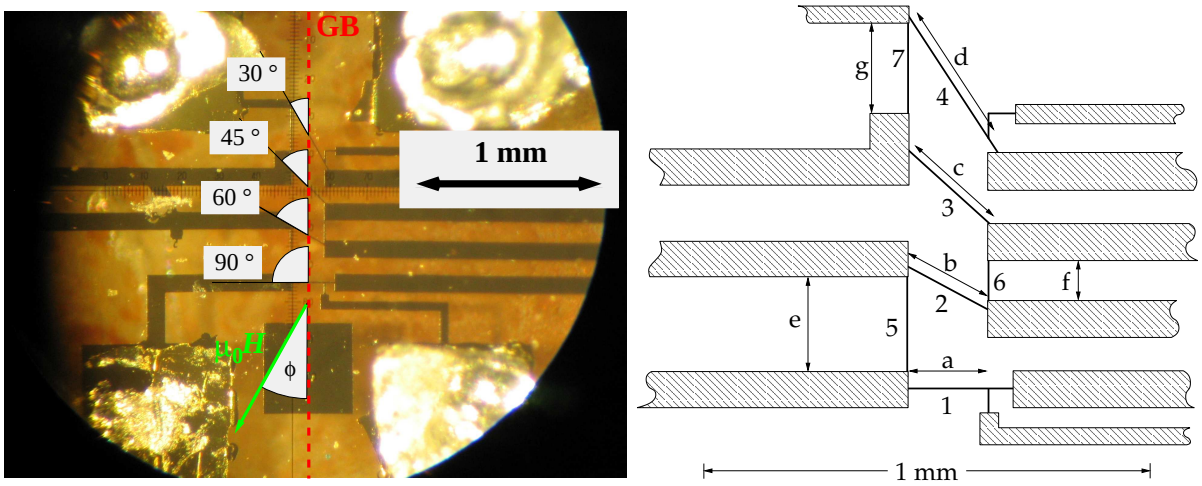

Figure 2.1: *Photograph of the middle section of the pattered thin film. It was made with a magnification of 50:1. The dashed red line marks the grain boundary. The dark parts are $YBa_2Cu_3O_{7-\delta}$. The actual tracks are the thin stripes traversing the grain boundary at the given angles representing Φ_{gb}. The green arrow symbolises the magnetic field applied in the film plane and rotated by φ. In the corners the nearly quadratic gold covered contact pads with pieces of Indium on the top are visible. On the right the outline of the tracks are shown. The numbers from 1 to 7 mark the tracks usable for transport measurements. The data presented here was taken on tracks 1 to 5. The arrows mark the distance of the voltage contacts for each track. The corresponding lengths are listed in Table 2.1.*

boundary angle Φ_{gb} and will be used to identify the corresponding track in the text. Track 5 will be referred to as "no GB".

The arrows mark the distance of the voltage contacts for each track. The lengths were determined from the photograph with a drawing program and are given in Table 2.1. Each length was read off five times to get a rough error estimate which resulted in an expected accuracy of ± 0.001 mm. The lengths vary by maximal 1.5 % from the theoretical length calculated by $d(\Phi_{gb} = 90\,^{o})/\sin\Phi_{gb}$. In cases where two 10 μm tracks meet, the distance was taken at the middle of the track.

2.2 Transport measurements

2.2.1 Handling thin film samples

YBCO is sensitive to moisture. The samples were usually kept in a dry-box. The exposure to moisture in normal air already leads to a steady degradation of the sample so that the handling of the sample should be kept as short as possible. If the sample is removed from the cryostat, it has to be heated above room temperature already in the cryostat to avoid condensation of water on the thin film. Although,

because of their very smooth and crack free surface, thin films are relatively resistant to moisture, they are also quite thin. The chemical reaction of YBCO with water is irreversible and leads to insulating reaction products. A thin layer of this reaction products is built up shortly after the first exposition to air and passivates the rest of the material to a certain degree. Because of the reduced cross-section of the conducting YBCO, film degradation manifests itself in an increasing normal conducting resistance and an unchanged superconducting transition temperature. During our experiments, no essential degradation effects of the film were observed.

2.2.2 Mounting the sample

Before mounting the sample on the sample stage the probe wiring has to be checked for proper condition. Also the current angular range settings of the stepper motors have to be checked. The spring loaded contacts are put into the correct position in the sample holder and the contact pins get connected to the probe. For the measurements always four pins were used, two for the sample voltage and two for the sample current. The sample is held in place only by the spring force of the contact pins. There was no indication, that four pins are not enough to keep the sample reliably at its position.

Especially the first time a sample gets mounted it has to be checked under the optical microscope for unwanted connections. Because of imperfections in the patterning process unetched YBCO often remains at the border of the substrate, which can lead to unintended current flow between the contact pads. The remaining areas of the thin film can be scratched with a sharp knife or a diamond tip to break these connections.

The indium pads are slices cut from an indium wire with a razor blade. They are put onto the contact pads of the thin film with one tip of a pair of tweezers. To avoid the indium pads from sticking too well to the tweezers' tip, the tip can be wrapped with Teflon tape. After placing all the indium slices they are pressed onto the film with the Teflon tape covered flat back of the tweezers. If some indium pieces on adjacent contacts get too close, they can be cut with a razor blade on the film.

It is not advised to measure the resistance of grain boundary tracks with an ohmmeter to check for the connection between the measurement setup and the film. The output voltage or current of the ohmmeter is usually too high and may break the sample. When putting the sample holder on the sample, it was not possible to see if the spring loaded contacts press properly onto the indium pads. To have some feed-

Track	90 °	60 °	45 °	30 °	no GB
T_{c0} in K	89.2	89.2	89.1	89.1	89.0

Table 2.2: *Evaluated values of* T_{c0}.

back about the connection with the sample, the two voltmeters in the measurement setup in the auto-range mode were used. If good contact is achieved, the voltmeters stop drifting and show a usually small, but constant offset value in the smallest voltage range.

If the mounting procedure was successful the probe is put into the cryostat and the sample cooled down. Usually the measurement of the transition temperature is done at this first cool down. Next the self field critical current at 77 K was measured. If the IV curves meet the expectations, the rotational measurements with applied field were started.

In the present measurements the temperature control was performed with two Oxford Instruments temperature controllers, an ITC503 for the *variable temperature insert* (VTI) heater and an ITC4 for the sample heater in the sample stage. The He gas temperature in the VTI was usually set about 10 K below the desired sample temperature to limit the current of the probe heater. This was done to protect the probe heater and to reduce electromagnetic interference of the heater current with the measurement. The sample temperature was measured with the ITC4 using a linear table in the ITC4. The temperature was calculated employing the calibration data of the Cernox resistor (CX-1050-AA) in the measurement program. At the VTI heat exchanger a Carbon Glass resistor (CGR-1-500) is used.

2.2.3 Transition temperature

The measurements of the superconducting transition temperature T_c are shown in Fig. 2.2. The electrical field in the right hand plot was calculated from the distances between the voltage contacts given in Tab. 2.1. Except for the 30 ° grain boundary the different measurements collapse approximately to one curve. No influence of the grain boundary can be seen. T_{c0} was evaluated by taking the intersection of the tangent through the inflection point of the transition with the x axis. The results are summarised in Table 2.2.

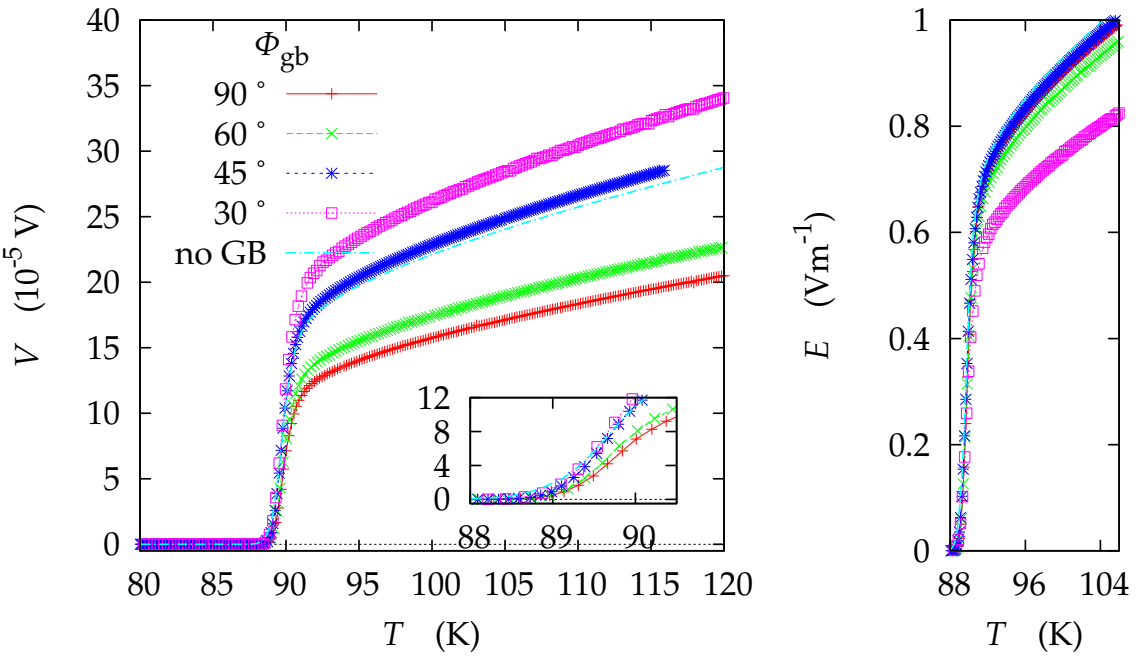

Figure 2.2: *Measurements of the superconducting transition temperature T_c. The left graph shows the original sample voltage and the right plot shows the electrical field, both versus the sample temperature. The electrical field was calculated by dividing the voltage by the lengths given in Table 2.1.*

2.2.4 Self field critical current

The self field critical current density on tracks traversing the grain boundary depends on Φ_{gb}. It is assumed, that this cannot be attributed to the difference of the distance between the voltage contacts. The (arbitrary) voltage criterion of 0.5 μV for all critical current evaluations presented here was chosen to cross the IV curve at a point, where the voltage rise is already quite steep. This should avoid a strong dependence of the evaluated J_c on the chosen voltage criterion. Secondly, the measured voltage in a IV curve of a grain boundary track should result from a potential difference appearing directly across the grain boundary. This is expected because of the reduced current carrying capability of the grain boundary. The rest of the thin film ("the grains"), including the area where the sample voltage is sensed, should not contribute an additional potential difference.

Low angle grain boundaries (LAGB) are built from a row of dislocations to accommodate for the misalignment of the adjacent grains. In a simple dislocation model the influence of the dislocation on the electrical properties is localised in a cylindrical volume enclosing the dislocation reaching from the surface to the film/substrate interface of the thin film. This cylinder is not superconducting and the rest of the

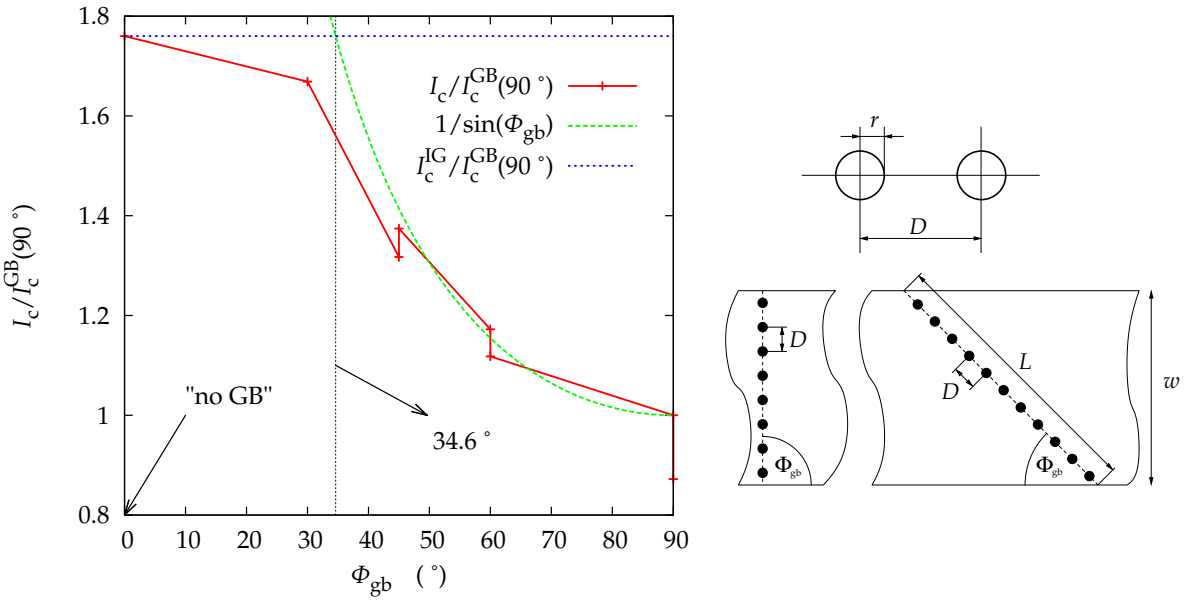

Figure 2.3: *Normalised self field critical current in dependence of the grain boundary angle Φ_{gb}. I_c is the self field critical current, I_c^{GB} and I_c^{IG} are inter- and intragrain critical currents, respectively. For comparison with the intergrain critical currents, $I_c^{IG}/I_c^{GB}(90\,^\circ)$ is plotted at $\Phi_{gb} = 0\,^\circ$. The sketch on the right shows the dimensions used in the text.*

material behaves as an undisturbed superconductor. The dependence of the self field critical current on the grain boundary angle, therefore, reduces to a geometrical relationship of the effective cross sections.

The geometry is also explained in the sketch in Fig. 2.3. D is the distance of adjacent dislocations, r is the radius of the dislocation cylinder, $d = D - 2r$, w_{track} is the width of the track, t_{film} is the thickness of the thin film and $n_{disloc}(\Phi_{gb}) = w_{track}/(D \sin \Phi_{gb})$ is the number of dislocations in the grain boundary. For a $4\,^\circ$ grain boundary $D = 5.6\,nm$ [8]. With our assumptions the current density should not depend on the grain boundary angle, only the cross-section does. The effective cross-section, $A_{track,eff}(\Phi_{gb}) = n_{disloc}(\Phi_{gb}) \cdot d$, and it follows

$$\frac{I_c^{GB}(\Phi_{gb})}{I_c^{GB}(90\,^\circ)} = \frac{1}{\sin \Phi_{gb}}\,. \tag{2.1}$$

This equation is plotted in Fig. 2.3. At $\Phi_{gb} = 0\,^\circ$ the value of $I_c^{IG}/I_c^{GB}(90\,^\circ)$ is added for comparison. Every self-field intergrain I_c^{GB} is smaller than the intragrain critical current. The angle of $34.6\,^\circ$ marked in Fig. 2.3 is the limiting angle, where the effective cross-section of the grain boundary is equal to the track cross-section,

$A_{\mathrm{track,eff}}(\Phi_{\mathrm{gb}}^{\mathrm{limit}}) = w_{\mathrm{track}}\, t_{\mathrm{film}}$. Rearranging this relation yields

$$\sin \Phi_{\mathrm{gb}}^{\mathrm{limit}} = 1 - \frac{2r}{D} = \frac{I_{\mathrm{c}}(90\,^{\mathrm{o}})}{I_{\mathrm{c}}^{\mathrm{IG}}}\,, \tag{2.2}$$

where the assumption was used, that the inter- and intragrain current densities are equal and the observed difference in the measured current densities again only depends on the different cross-sections. The equality of the inter- and intragrain critical current density solved for the dislocation radius leads to

$$r = \frac{D}{2}\left(1 - \frac{I_{\mathrm{c}}(90\,^{\mathrm{o}})}{I_{\mathrm{c}}^{\mathrm{IG}}}\right)\,. \tag{2.3}$$

The evaluation of (2.3) for the measured self-field data results in $r = 1.2\,\mathrm{nm}$. Even though this dislocation picture is very crude, it seems to give at least an rough explanation of the measured self-field critical currents.

2.2.5 Rotational measurements

For all rotational measurements a configuration was chosen where the magnetic field is rotated parallel to the *ab*-planes. On tracks without a grain boundary the critical current is determined by intrinsic pinning and the angular dependence is attributed to the variation of the Lorentz force. The usual explanation assumes that the depinning of the vortices is caused only by the Lorentz force acting on them. When the current density is parallel to the magnetic field the Lorentz force vanishes and the critical current should be maximal (*force free configuration*). If the field is perpendicular to the current direction, the Lorentz force is maximal and the critical current at its minimum (*maximum Lorentz force configuration*). This behaviour was found on the track measured without grain boundary and on most of the grain boundary tracks. As shown earlier [12], the effect of the grain boundary is a pronounced drop of J_{c} when the field is aligned with the grain boundary. The minimum of the critical current is found at an angle, where the field is exactly aligned with the grain boundary and the critical current rises symmetrically around this angle. If the critical current determined by the intrinsic pinning is low enough, the expected angular behaviour due to intrinsic behaviour is overlaid by the symmetric drop around the grain boundary. In some cases of the present measurements the angular dependence of the critical current is ruled only by the grain boundary over the whole angular range.

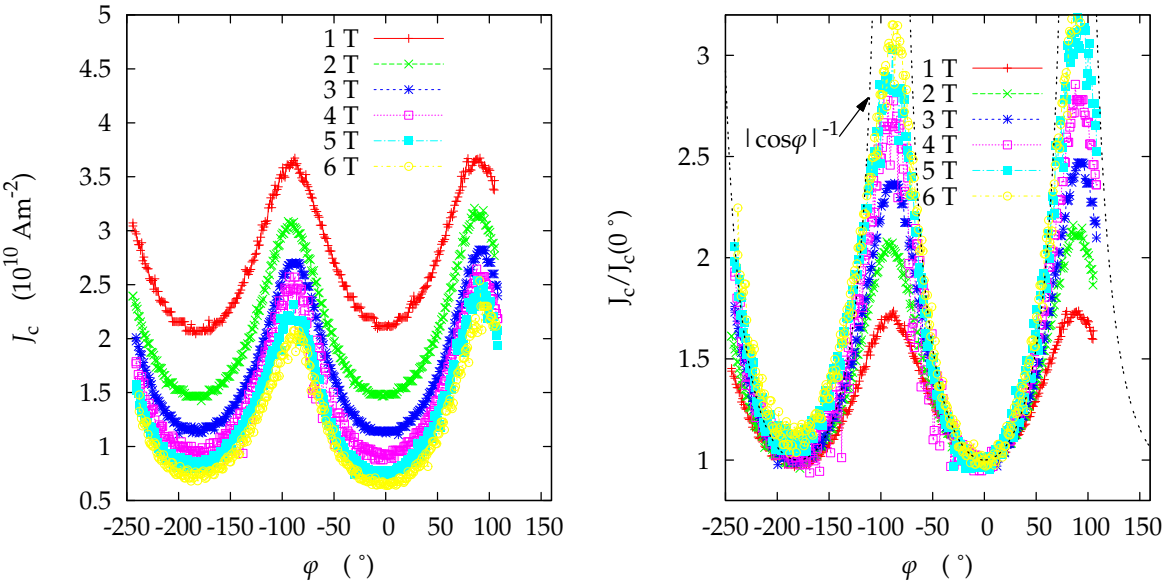

Figure 2.4: *Angular dependence of the critical current density on a thin film track without a grain boundary. The data were obtained at* 60 K *from* 1 *to* 6 T. *On the right panel each curve is divided by* $J_c(0°)$ *for comparison with the angular dependence of a straight vortex description,* $|\cos\varphi|^{-1}$.

2.2.6 Grain boundary free track

With an applied magnetic field a strong dependence of the observed critical current density on the field direction evolves. On a track without a grain boundary the most fundamental explanation is based on the Lorentz force acting on straight vortices in a type II superconductor. The vortices are assumed to be aligned with the applied magnetic field and pinned by a homogeneous and isotropic pinning force density f_p. The self field of the superconducting current and distortions of the vortices due to the superconducting volume are ignored. Only the force balance between the Lorentz force density and the pinning force density

$$J\Phi_0 \sin\alpha = f_p \tag{2.4}$$

is considered. The current density J is assumed to be parallel to the track and the angle between J and the field direction is α. f_p increases with the current density in an IV measurement until it reaches a material specific maximum value, f^*_{pm}. Beyond this point the pinning force does not suffice to hold the vortices in place and a voltage appears along the track. The critical current density J_c is defined as the value of J, where a certain voltage criterion ($5 \cdot 10^{-7}$ V in the J_c evaluations presented here) is reached. The critical current density therefore defines in this simple picture the

maximum pinning force density

$$J_c \Phi_0 \cos\varphi = f^*_{pm} \,. \tag{2.5}$$

In (2.5) the origin of φ was shifted so that $\varphi = 0\,^o$ corresponds to the maximum Lorentz force configuration and $\varphi = 90\,^o$ to the force free configuration. The expected dependence of J_c on φ in this picture is $\propto |\cos\varphi|^{-1}$. At the minimum of this curve f^*_{pm} can be determined as $J_c(0\,^o)/\Phi_0$. This straight vortex picture fails to describe the force free case because it produces a divergence at $\varphi = 90\,^o$.

Figure 2.4 shows on the left rotational measurements of J_c obtained at 60 K in magnetic fields from 1 to 6 T. In the plot on the right the same curves are divided each by $J_c(0\,^o)$ for comparison with the expected angular dependence following from the straight vortex picture. One observes, that the higher the applied magnetic field the wider the applicable angular range of the model. The approximate angular range around $0\,^o$, where the normalised J_c curves coincide with the theoretical curve, amounts to about $\pm 20\,^o$ for a magnetic field of 1 T, $\pm 30\,^o$ for 2 and 3 T, $\pm 50\,^o$ for 4 T and extends to about $\pm 60\,^o$ above 5 T.

2.2.7 Grain boundary tracks

Figure 2.5 shows an overview of the angular dependence of J_c measured on grain boundary thin film tracks. In the left plot measurements at 40 K from 1 to 6 T on a $90\,^o$ grain boundary track are presented. Each curve is shifted by a certain angle $\Delta\varphi$ to emphasise the magnetic field dependence. The force free maxima do not systematically decrease with increasing magnetic field in contrast to the decrease of the minima, where the magnetic field is parallel to the grain boundary. It is assumed, that the whole angular range of the J_c curves in the left plot is determined by the flux-breaking/rejoining process of the vortices in the grain boundary, because they were measured on a $90\,^o$ grain boundary track. The intragrain critical current curve would have its minima and maxima at the same angular positions as the actually measured J_c curves. But an intragrain critical current force free maximum should, especially at higher magnetic fields, be narrower and one would expect a stronger field dependence of the force free critical current density (see Fig. 2.4). In the right panel of Fig. 2.5 angular dependencies of J_c measured on a $60\,^o$ thin film track at 60 K and magnetic fields of 1, 3 and 5 T are shown. They are compared to the angular dependence at the same temperature and fields taken from the thin film track without

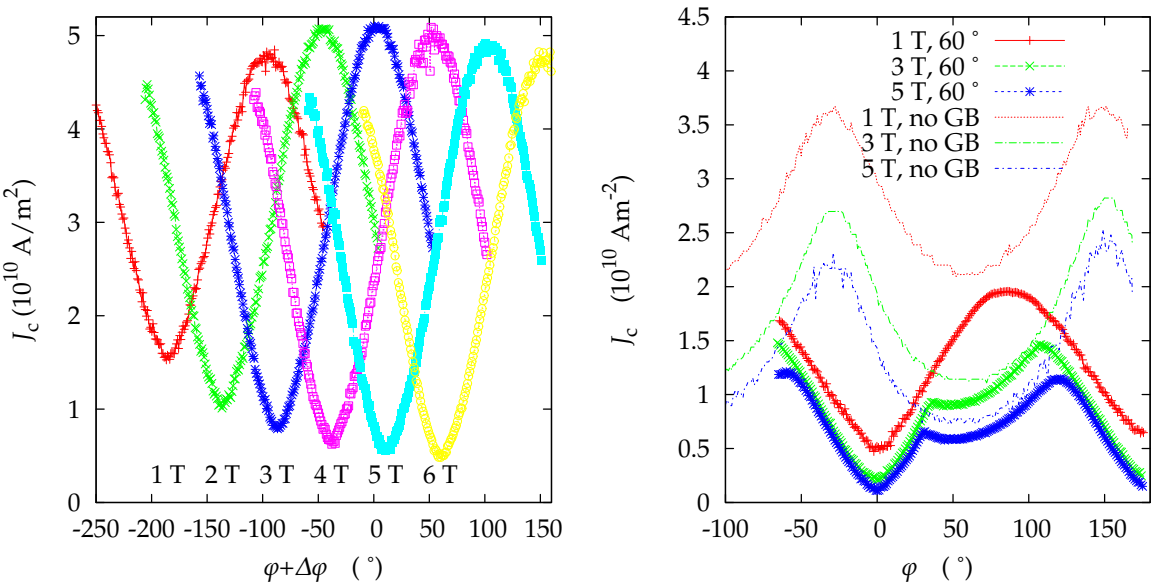

Figure 2.5: *Angular dependence of the critical current density on grain boundary thin film tracks. In the left plot measurements at* 40 K *from* 1 *to* 6 T *on a* 90 ° *are presented. Each curve is shifted by a certain angle* $\Delta\varphi$ *for better comparison. The right plot contains* J_c *measurements at* 60 K *and magnetic fields of* 1, 3 *and* 5 T. *The curves measured on a thin film track without grain boundary (without symbols) are compared to measurements on a* 60 ° *grain boundary track (with symbols). No scaling is applied.*

grain boundary and shifted by Φ_{gb} (no symbols). All grain boundary curves show the symmetric channelling minimum at 0 ° but, except for the 1 T case, the maximum is clearly "cut off" by the minimum of the intragrain critical current. The 1 T curve shows the same behaviour as the plots in the left graph of Fig. 2.5. The comparison with the corresponding curve from the grain boundary free track suggests, that the intragrain critical current density was larger than the channelling dominated one over the whole angular range. On tracks with a grain boundary angle other than 90 ° the intragrain J_c minimum is shifted closer to the angular position of the force free maximum of the intergrain J_c. For these cases the two different critical current regimes can usually be clearly identified.

Grain boundary angle scaling

In 2.2.4 the dependence of the self field critical current on the grain boundary angle Φ_{gb} was discussed. If the given interpretation of a reduction of the cross section due to non superconducting dislocation cores is correct, this effect should not vanish when a magnetic field is applied. In Figure 2.6 the rotational measurements at 50 K

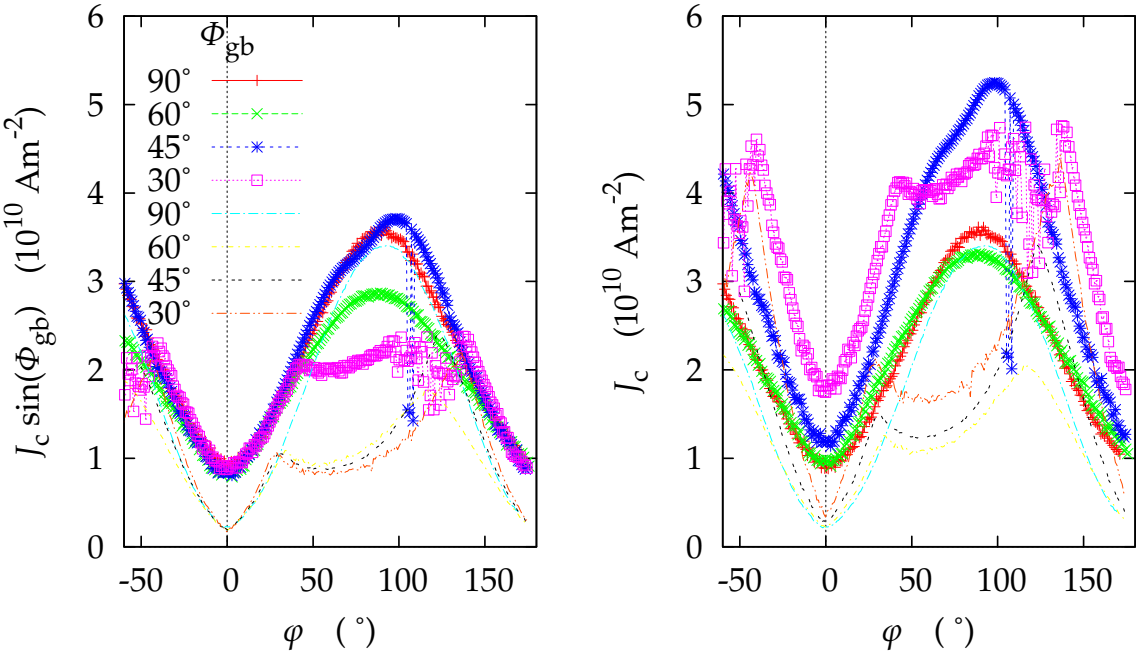

Figure 2.6: *Angular dependence of the critical current density on grain boundary thin film tracks measured at* 50 K *and two magnetic fields,* 1 *and* 6 T. *In the left plot the* J_c *values are multiplied by* $\sin\Phi_{gb}$. *For the calculation of* J_c *the thin film track cross-section of* $2 \cdot 10^{-12}$ m^2 *was used.*

and two magnetic fields, 1 and 6 T, for all four grain boundary tracks are shown. For the calculation of J_c the thin film track cross-section of $2 \cdot 10^{-12}$ m^2 was employed. In the left plot the J_c values are in addition multiplied by $\sin\Phi_{gb}$, which is the necessary correction for the grain boundary angle dependent cross-section. The scaled J_c curves measured on different grain boundary tracks collapse at least close to $\varphi = 0\,^{o}$, which justifies this scaling approach.

For the rest of this chapter the scaling of the critical current density by $\sin\Phi_{gb}$ in combination with the track cross-section was used to eliminate effects on J_c only resulting from the length difference of the grain boundary crossing the thin film track. It should also make results obtained for different Φ_{gb} values more comparable. The difference between the track cross-section and the effective cross-section on a grain boundary track for $\Phi_{gb} = 90\,^{o}$ was ignored. The evaluation of the effective cross-section (dislocation radius) as described in 2.2.4 requires the additional assumption, that the inter- and intragrain critical current densities are equal. It was preferred to avoid this assumption.

It should be noted, that the current flow across the grain boundary is assumed to be perpendicular to the grain boundary plane. If this were not the case, the variation

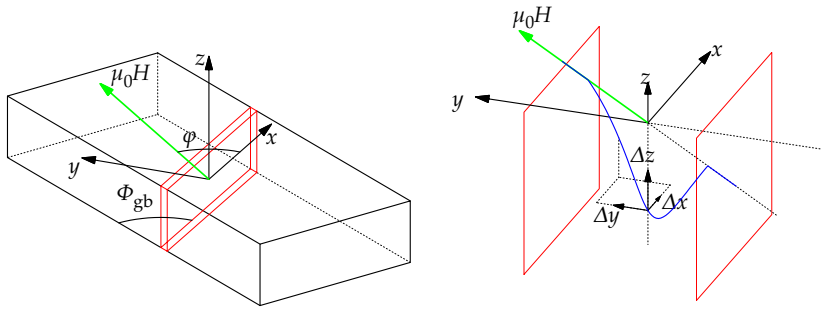

Figure 2.7: *The left illustration shows the coordinate system and angles used for plots and in the evaluation of the J_c transport data. The black box should represent a cutout of the track with a grain boundary (red). The y axis is always perpendicular to the grain boundary plane. On the right the grain boundary volume is drawn in more detail. The xyz coordinate system is the same as in the left plot and also the one utilised in the computer program. The $\Delta x \Delta y \Delta z$ coordinate system is used in the analytical description. The Δx and Δy coordinates coincide with the x and y coordinates. The Δz coordinate differs from the z coordinate by the maximal displacement of the vortex.*

of the Lorentz force with the grain boundary angle would also lead to the described scaling behaviour, but the dependence of the self field J_c in Φ_{gb} would not be covered by such an alternative explanation. In addition one would expect an unsymmetrical channelling minimum, which is not observed.

Elastic single vortex model

To describe the angular dependence of the critical current on a thin film grain boundary track, a single vortex model was proposed in [12]. It is assumed that the vortex is a string with constant line energy ϵ_l (force or energy per length) situated in a continuous isotropic superconducting volume. The superconductor is characterised only by a maximum pinning force density (force per length) derived from a measured critical current density. Without a current the vortices are assumed to align with the applied magnetic field and distortions of the field due to the geometry of the superconducting volume are ignored. When a current flows through the sample, the Lorentz force bends the vortex string elastically away from the straight field direction. On a vortex line segment the Lorentz force density is counteracted by the sum of the elastic force density and the pinning force density. The magnitude of the pinning force density is limited by its maximum value. The maximum pinning force density inside the grains, f^*_{pm}, is assumed to be much larger than the maximum pinning force density

f_{pm} in the grain boundary region. The bulk superconductor is therefore also referred to as *high pinning region* (HPR) and the grain boundary is called the *low pinning region* (LPR).

The grain boundary has a thickness d_{gb} and the length of a straight vortex crossing the grain boundary at an angle φ is $D = d_{\mathrm{gb}} \sin \varphi$. The coordinate systems and angles used in the following discussion are described in Fig. 2.7. The xyz coordinate system is utilised in the computer programmed iteration. The $\Delta x \Delta y \Delta z$ coordinate system is used in the analytical description in Section 2.2.7. Its origin is positioned at the middle point of the vortex path with the most negative z coordinate. As should become clear from the illustration in Fig. 2.7, the Δx and Δy coordinates coincide with the x and y coordinates. The Δz and z axis point in the same direction and $z - \Delta z$ is the vortex displacement.

The basic idea of the model is, that a vortex traversing the grain boundary will be pinned strongly in the grains and far less in the grain boundary. With an applied current the *Lorentz force density* f_{LF} will act along the whole vortex equally. When f_{LF} is sufficient to de-pin the vortex in the grain boundary but not in the grains, the part of the vortex traversing the boundary will bend and eventually break. The breaking of a vortex means, that the line tension of the vortex cannot counteract the forces acting on it. The vortex will extend in a larger and larger growing loop until it comes close enough to a neighbouring vortex, where it will cut and cross-join with it. The resultant effect of this cutting and cross-joining process is a vortex movement along the grain boundary (also referred to as vortex channelling). With respect to the transport measurements the voltage rises linearly with the current as it would be in the flux flow regime. Of course this elastic single vortex model cannot give any information about the channelling mechanism itself. The expectation is to find a boundary for the maximum possible current, where channelling sets in. This should be close to the measured critical current.

In [12] the vortices in the grain boundary are assumed to be straight and the effect of the line energy is taken into account by a *vortex breaking force* F_{break}. This is assumed to be the force necessary to break a vortex in the absence of pinning in the grain boundary volume. It acts on a vortex line of length D so the breaking force density is F_{break}/D. For a current density J the absolute value of the Lorentz force density on a single, straight vortex traversing the grain boundary at an angle φ is given by

$$f_{\mathrm{LF}} = \Phi_0 J \cos \varphi \,. \tag{2.6}$$

The vortex breaking sets in when f_{LF} is sufficient to counteract F_{break}/D and f_{pm}, therefore at $J = J_{\mathrm{c}}$ the Lorentz force density is equal to $F_{\mathrm{break}}/D + f_{\mathrm{pm}}$ leading to

$$J_{\mathrm{c}}(\varphi) = \frac{F_{\mathrm{break}}}{\Phi_0 \, d_{\mathrm{gb}}} \tan\varphi + \frac{f_{\mathrm{pm}}}{\Phi_0 \cos\varphi} \,. \tag{2.7}$$

This result was confirmed in [21] for a vortex bent to a half circle as a limiting case for small φ. Therein it was also shown, that in this case F_{break} is equal to $2\epsilon_{\mathrm{l}}$.

Numerical approach

In [21] the simplification of straight vortices in the grain boundary was dropped. The analytical result (2.7) for infinite HPR pinning was achieved for the limit of $\varphi \to 0$ by applying the analytical form of the elastic force density

$$\boldsymbol{f}_{\mathrm{e}}(t) = \frac{\epsilon_{\mathrm{l}}}{|\partial_t \boldsymbol{r}|^4} \partial_t \boldsymbol{r} \times \partial_t \boldsymbol{r} \times (\partial_t^2 \boldsymbol{r} \times \partial_t \boldsymbol{r}) \,, \tag{2.8}$$

the Lorentz force density

$$\boldsymbol{f}_{\mathrm{LF}} = \Phi_0 \boldsymbol{J} \times \frac{\partial_t \boldsymbol{r}}{|\partial_t \boldsymbol{r}|} \,, \tag{2.9}$$

and solving the force density equation

$$\boldsymbol{f}_{\mathrm{LF}} + \boldsymbol{f}_{\mathrm{e}} + \boldsymbol{f}_{\mathrm{pm}} = 0 \tag{2.10}$$

to achieve the result (2.7). $\boldsymbol{r}(t)$ is the parametrisation of the vortex line path C (smooth curve) with $\int_C |\partial_t \boldsymbol{r}| \, \mathrm{d}t$ over the vortex path being the length of the vortex.

To extend the applicable angular range a numerical approach was utilised again assuming an infinite f^*_{pm}. The vortex was built up of nodes connected by straight vortex segments. The vector sum (2.10) was solved iteratively for every node and the contribution of ϵ_{l} and f_{pm} was analysed. The numerically calculated angular dependence of the current density could be described well by a fit curve containing these two parameters [21]:

$$J_{\mathrm{c}}(\varphi) = \frac{2\epsilon_{\mathrm{l}}}{d_{\mathrm{gb}} \Phi_0} (\tan|0.78\varphi| + 0.22 \sin|\varphi|) + \frac{f_{\mathrm{pm}}}{\Phi_0 \sqrt{|\cos\varphi|}} \,. \tag{2.11}$$

It should be noted, that this is not the complete result given in [21], but results from the numerical calculation. (2.11) confirms the result (2.7) for small φ. It should be

applicable for almost the angular range from $0\,^{o}$ to $90\,^{o}$. Unfortunately, a comparison with the data obtained in this work left some questions open. Of course the divergence at $\varphi = 90\,^{o}$ is unphysical and the authors of [21] were perfectly aware of this fact. They proposed an upper estimate for the force free critical current density assuming a helical vortex configuration. Some of the J_c curves in this work seem to never leave the channelling regime and the force free maxima round off rather flatly, almost sinusoidal. The steep rise of the tangent at larger angles is not found and the additional divergence of the $(\cos\varphi)^{-1/2}$ term does not improve this. It could have been expected, that the very general numerical approach should have covered the force free direction better because, as shown in [21], it produces helical vortices for angles close to $90\,^{o}$. The second problem arises at φ close to zero because the corner like rise was found only in a few of the measured curves. Most of the critical current density minima round off and are broader. It does not help to correct the maximum pinning force density below the measured channelling minimum of J_c (in (2.7) and (2.11) $J_c = f_{pm}/\Phi_0$ for $\varphi \to 0$) as was done in [21], where the model was fitted to a rotational measurement on a grain boundary. This leads to the awkward situation of having two LPR pinning force densities: one, that stems from the picture of straight vortices not pinned by the grains at $\varphi = 0\,^{o}$ and which is therefore determined by $J_c(0\,^{o})$, and another, that is introduced to make the fit look better. Between these two limiting cases of φ the model seems to reproduce the measured curves reasonably well.

Alternative solution for the numerical approach

During the process of re-implementing the numerical iteration proposed in [21], I become aware of the fact that the whole problem is highly symmetrical and that it should be possible to simplify the calculation. It turned out that this is indeed possible for the case of zero pinning force density. The resulting equation reproduces the results of the numerical iteration algorithm in the whole angular range and is also in agreement with the analytic spiral vortex solution given in [21]. The effect of a nonzero LPR pinning force density could be at least approximately included in this equation. The advantage of this analytical result compared to (2.11) is, that it allows an inspection of the origins of the non-physical properties and might point out possible corrections.

Like in the numerical calculation the vortex is split up into a number of nodes connected by straight segments. Unlike the previously described computer model,

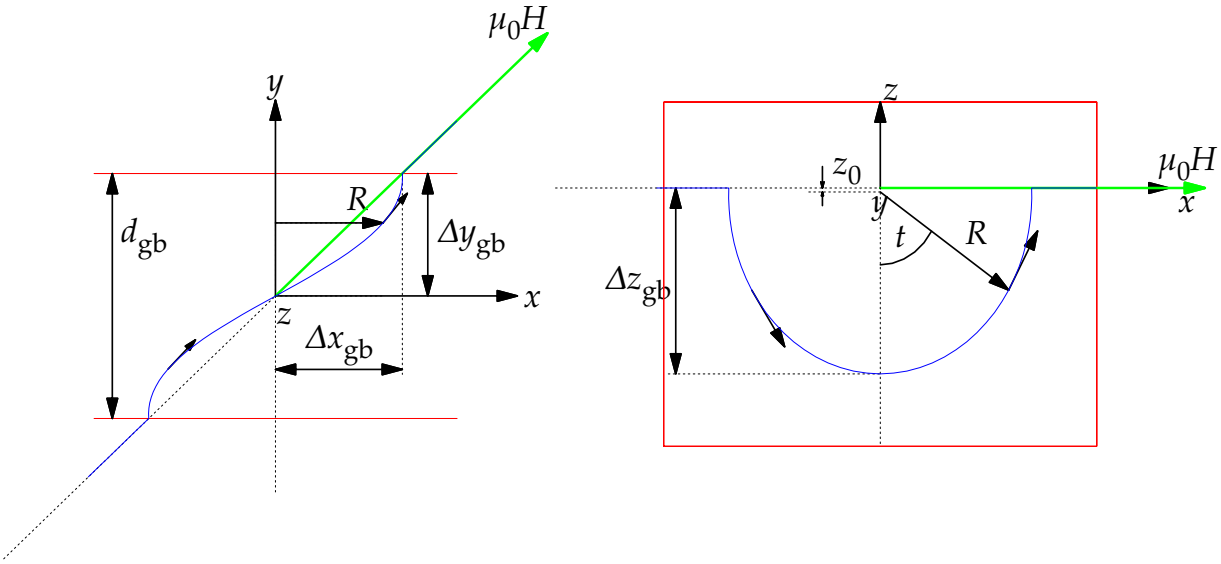

Figure 2.8: *Projection of a numerically calculated vortex spiral (φ=50°) on the xy plane (left) and on the xz plane (right). R is the vortex radius, t is the curve parameter used in the parametrisation of the vortex line and z_0 is the z coordinate of the middle axis of the circular vortex spiral.*

the length of the straight segments, l, is held constant, not the number of nodes. The discrete form of $\boldsymbol{f}_{\mathrm{LF}}$ acting on the i-th node between the segment $i-1$ and i is

$$\boldsymbol{f}^i_{\mathrm{LF}} = \frac{\Phi_0}{l}\boldsymbol{J} \times l \frac{\hat{\boldsymbol{e}}^{i-1}_{\mathrm{l}} + \hat{\boldsymbol{e}}^{i}_{\mathrm{l}}}{|\hat{\boldsymbol{e}}^{i-1}_{\mathrm{l}} + \hat{\boldsymbol{e}}^{i}_{\mathrm{l}}|}\,, \tag{2.12}$$

and the discrete form of $\boldsymbol{f}_{\mathrm{e}}$ is

$$\boldsymbol{f}^i_{\mathrm{e}} = \frac{\epsilon_{\mathrm{l}}}{l}(\hat{\boldsymbol{e}}^{i}_{\mathrm{l}} - \hat{\boldsymbol{e}}^{i-1}_{\mathrm{l}})\,. \tag{2.13}$$

$\hat{\boldsymbol{e}}^i_{\mathrm{l}}$ is a unit vector in the direction of i-th segment (between the nodes with indices i and $i+1$). Looking at a usual vortex line produced by the numerical model at intermediate angles certain features become obvious (see Fig. 2.8). Because there are only two vectors in the calculation, the current vector and the field vector, the result has to be point symmetric. Plotting the vortex curve projection onto the xy plane shows that every x and y component of the tangent turns up two times along the vortex. The projection will always go through the point $x = 0$, $y = 0$. Looking at the curve in the yz plane reveals that the z component of the tangent is zero in the

middle at $y = 0$ and is of equal magnitude and opposite sign for two opposite y positions of the same magnitude. With this symmetry the sum of force densities over all points can be calculated. We are searching for the force equilibrium (2.10). If it is fulfilled for every single node, also the sum over all nodes will fulfil this equation. Especially (2.13) gives a very simple form, when the summation is elaborated over several nodes, not even depending on any symmetry:

$$\sum_{\text{nodes}} \boldsymbol{f}_{\text{e}}^{i} = \frac{\epsilon_{\text{l}}}{l}(\hat{\boldsymbol{e}}_{\text{l}}^{\text{end}} - \hat{\boldsymbol{e}}_{\text{l}}^{\text{start}})\,. \tag{2.14}$$

For brevity let us rename the intermediate tangent unit vector in (2.12) by $\hat{\boldsymbol{e}}_{\text{l}}^{i'} = (\hat{\boldsymbol{e}}_{\text{l}}^{i-1} + \hat{\boldsymbol{e}}_{\text{l}}^{i})/|\hat{\boldsymbol{e}}_{\text{l}}^{i-1} + \hat{\boldsymbol{e}}_{\text{l}}^{i}|$. Note, that the i'-th segment (in the direction $\hat{\boldsymbol{e}}_{\text{l}}^{i'}$) is the tangent *at* the i-th node needed for calculating the Lorentz force acting on the i-th node. $\boldsymbol{J}$ points in the y direction, so the cross product for the i'-th segment is

$$\boldsymbol{f}_{\text{LF}}^{i} = \frac{\Phi_0}{l}\begin{pmatrix} Jl\,\hat{e}_{\text{l,z}}^{i'} \\ 0 \\ Jl\,\hat{e}_{\text{l,x}}^{i'} \end{pmatrix}, \tag{2.15}$$

and summing the z and x components of the vortex segments starting at $(\Delta x, \Delta y, \Delta z) = (0,0,0)$ and ending at $(\Delta x, \Delta y, \Delta z)$ results in $\sum_{i'} l\hat{e}_{\text{l,z}}^{i'} = \Delta z$ and $\sum_{i'} l\hat{e}_{\text{l,x}}^{i'} = \Delta x$. Therefore we have

$$\sum_{\text{nodes}} \boldsymbol{f}_{\text{LF}}^{i} = \frac{J\Phi_0}{l}\begin{pmatrix} \Delta z \\ 0 \\ -\Delta x \end{pmatrix}. \tag{2.16}$$

To keep it simple, let us at first ignore the pinning force density and write down $\sum_i \boldsymbol{f}_{\text{LF}}^{i} + \boldsymbol{f}_{\text{e}}^{i} = 0$ explicitly for a vortex piece starting at the $\Delta x \Delta y \Delta z$ origin (middle of the vortex path inside the LPR) and an arbitrary point $(\Delta x, \Delta y, \Delta z)$ in the positive Δy half space

$$\begin{aligned} (\Phi_0 J/l)\,\Delta z + (\epsilon_{\text{l}}/l)\,(\hat{e}_{\text{l,x}} - \hat{e}_{\text{l,x}}^{\text{c}}) &= 0 \\ 0 + (\epsilon_{\text{l}}/l)\,(\hat{e}_{\text{l,y}} - \hat{e}_{\text{l,y}}^{\text{c}}) &= 0 \\ -(\Phi_0 J/l)\,\Delta x + (\epsilon_{\text{l}}/l)\,(\hat{e}_{\text{l,z}} - \hat{e}_{\text{l,z}}^{\text{c}}) &= 0\,. \end{aligned} \tag{2.17}$$

$\hat{e}_{\text{l,x}}^{\text{c}}$, $\hat{e}_{\text{l,y}}^{\text{c}}$ and $\hat{e}_{\text{l,z}}^{\text{c}}$ are the components of the tangent unit vector at the middle of the vortex. After eliminating l and using $a' = J\Phi_0/\epsilon_{\text{l}}$ and $\hat{e}_{\text{l,z}}^{\text{c}} = 0$, one arrives at three

equations:

$$\hat{e}_{l,x} = \hat{e}^c_{l,x} - a'\Delta z \quad \hat{e}_{l,y} = \hat{e}^c_{l,y} \quad \hat{e}_{l,z} = a'\Delta x\,. \tag{2.18}$$

Putting these components of the tangent unit vector into the normalisation equation $1 = \hat{\boldsymbol{e}}_l^2$ leads to a quadratic equation for the Δz coordinate with the result

$$\Delta z = \frac{\hat{e}^c_{l,x}}{a'} \pm \sqrt{\left(\frac{\hat{e}^c_{l,x}}{a'}\right)^2 - \Delta x^2}\,. \tag{2.19}$$

The solution calculated by this approach is a circular spiral with a radius of

$$R = \frac{\hat{e}^c_{l,x}}{a'} = \frac{\sqrt{1-\hat{e}^2_{l,y}}}{a'} \tag{2.20}$$

and a constant slope in the current direction determined by $\hat{e}_{l,y}$. Because $\hat{e}_{l,y}$ is constant, it is directly related to the overall vortex length L:

$$\hat{e}_{l,y} = \frac{2\Delta y}{L}\,. \tag{2.21}$$

$(\Delta x_{gb}, \Delta y_{gb}, \Delta z_{gb})$ refers to the point where the vortex path leaves the LPR region in the positive y half space. Δz_{gb} therefore represents by definition the vortex displacement in the negative z direction.

Parametrisation

For the further discussion it is helpful to introduce a parametric curve representation of (2.18):

$$\boldsymbol{r}(t) = \begin{pmatrix} R\sin t \\ k\,t \\ R(1-\cos t) \end{pmatrix}\,. \tag{2.22}$$

The path of the vortex line described by $\boldsymbol{r}$ is chosen to be bent in the $-z$ direction. The components are again in the $\Delta x\Delta y\Delta z$ coordinate system. t is half the opening angle of the circular projection with the radius R of the vortex line on the xz plane, where the point with $t = 0$ lies on the z axis at the origin of the $\Delta x\Delta y\Delta z$ system. The central axis of the spiral is at $z = z_0$, see also Fig. 2.8. This should be appropriate for a field and current vector pointing into the positive y half space. Because the force densities only depend on derivatives of $\boldsymbol{r}$, constants can be added to every component without changing the force density equilibrium equation. Only shifts in the z component are

interesting in our context. Using the definitions (2.8) and (2.9) one finds

$$\boldsymbol{f}_{\mathrm{e}} = -\frac{\epsilon_1 R}{\sqrt{R^2+k^2}} \begin{pmatrix} \sin t \\ 0 \\ -\cos t \end{pmatrix} = -\frac{\epsilon_1}{R}(1-\hat{e}_{\mathrm{l,y}}^2) \begin{pmatrix} \sin t \\ 0 \\ -\cos t \end{pmatrix} \text{ and} \tag{2.23}$$

$$\boldsymbol{f}_{\mathrm{LF}} = \frac{JR\Phi_0}{\sqrt{R^2+k^2}} \begin{pmatrix} \sin t \\ 0 \\ -\cos t \end{pmatrix} = J\Phi_0\sqrt{1-\hat{e}_{\mathrm{l,y}}^2} \begin{pmatrix} \sin t \\ 0 \\ -\cos t \end{pmatrix} \tag{2.24}$$

where $\hat{e}_{\mathrm{l,y}} = k/\sqrt{R^2+k^2}$ has been employed. The resulting equilibrium equation (2.10), $f_{\mathrm{pm}} = 0$, is

$$J = \frac{\epsilon_1}{\Phi_0\sqrt{R^2+k^2}}\,. \tag{2.25}$$

The same result can be achieved from the first or the third equation in (2.18) using $\hat{e}_{\mathrm{l,x}} = (R\cos t)/\sqrt{R^2+k^2}$ and $\hat{e}_{\mathrm{l,z}} = (R\sin t)/\sqrt{R^2+k^2}$.

The dependence on the field direction φ comes into play by fixing the vortex line boundary conditions:

$$\boldsymbol{r}(t_1) = \begin{pmatrix} R\sin t_1 \\ k\,t_1 \\ R(1-\cos t_1) \end{pmatrix} = \begin{pmatrix} \Delta x_{\mathrm{gb}} \\ \Delta y_{\mathrm{gb}} \\ \Delta z_{\mathrm{gb}} \end{pmatrix} = \begin{pmatrix} (d_{\mathrm{gb}}\cos\varphi)/(2\sin\varphi) \\ d_{\mathrm{gb}}/2 \\ R - z_0 \end{pmatrix}. \tag{2.26}$$

The vortex path starts at $t = -t_1$ and reaches the other end of the grain boundary at $t = t_1$. The z coordinate of the midpoint of the circular projection on the xz plane of the vortex spiral, z_0, is constant:

$$z_0 = \sqrt{R^2 - \Delta x_{\mathrm{gb}}^2} \text{ and } R = z_0 + \Delta z_{\mathrm{gb}}\,. \tag{2.27}$$

Vortex spirals will be referred to as "helical", if $t_1 > \pi/2$ or, equivalently, if the sign of z_0 is negative. Δx_{gb}, Δy_{gb} and Δz_{gb} are considered as distances and are always taken as positive values.

After (2.26) t_1 can be expressed in terms of k:

$$t_1 = \frac{d_{\mathrm{gb}}}{2k}\,. \tag{2.28}$$

The vortex length inside the grain boundary is

$$L = 2t_1\sqrt{R^2+k^2} = d_{\mathrm{gb}}\sqrt{(R/k)^2+1}\,. \tag{2.29}$$

This shows, that the vortex length is constant if R is proportional to k. Constant vortex length solutions have a completely different angular dependence of the critical current from that observed in the measurements.

By straight forward geometrical considerations, expressions for R and k in terms of Δx_{gb} and Δz_{gb} can be derived, which will be of use later.

$$R = \frac{\Delta x_{\mathrm{gb}}^2 + \Delta z_{\mathrm{gb}}^2}{2\,\Delta z_{\mathrm{gb}}} \quad k = \frac{d_{\mathrm{gb}}}{2\arccos\frac{\Delta x_{\mathrm{gb}}^2 - \Delta z_{\mathrm{gb}}^2}{\Delta x_{\mathrm{gb}}^2 + \Delta z_{\mathrm{gb}}^2}}\,. \tag{2.30}$$

Inclusion of the pinning force density

Because one cannot pull longitudinally on a vortex all forces have to act perpendicularly on it. Obviously the Lorentz force always points radially away from the current direction. As long as only two force densities, $\boldsymbol{f}_{\mathrm{LF}}$ and $\boldsymbol{f}_{\mathrm{e}}$, are considered, the elastic force density has to oppose the Lorentz force density and, because $\hat{e}_{\mathrm{l,y}}$ is constant, all forces are radial and have a constant size. If $f_{\mathrm{pm}} = 0$, the vector sum (2.10) reduces to a single equation containing only the length of the vectors of the force densities.

A third force density complicates the situation, because now the vector character of the involved quantities cannot be ignored any more. The force densities for every point of the vortex line form a two dimensional vector sum parallelogram in the plane perpendicular to the vortex line. In general a nonzero y component of the elastic and the pinning force density can exist. This component in the current density direction will result in a non-constant $\hat{e}_{\mathrm{l,y}}$ component, because it adds an non-zero term to the second equation of (2.18). Therefore, the modulus of the Lorentz force density will not be constant along the vortex line.

The model assumes a homogeneous, isotropic pinning force density with an upper limit. Therefore, additional assumptions are necessary to determine the components of $\boldsymbol{f}_{\mathrm{pm}}$. Because the pinning force density is isotropic, the influence on the overall geometry will not be too strong. If, like in the zero pinning case, the geometry is again a circular spiral with constant slope, then the three force densities should all be radial and their sum should again reduce to a scalar equation. The comparison with numerical iteration results suggests, that this is a reasonable approximation.

For the circular spiral geometry, including f_{pm} into the force equilibrium is straight forward. $\boldsymbol{f}_{\mathrm{pm}}$ should point in the same direction as $\boldsymbol{f}_{\mathrm{e}}$ and, therefore, the force density equilibrium equation in parametrised form reads

$$\frac{JR\Phi_0}{\sqrt{R^2+k^2}} - \frac{\epsilon_1 R}{R^2+k^2} - f_{\mathrm{pm}} = 0\,. \tag{2.31}$$

Alternatively f_{pm} can also be incorporated in the summation procedure. $\boldsymbol{f}_{\mathrm{pm}}$ can be written for the i-th node as

$$\boldsymbol{f}^i_{\mathrm{pm}} = -f_{\mathrm{pm}} \frac{\boldsymbol{f}^i_{\mathrm{LF}}}{|\boldsymbol{f}^i_{\mathrm{LF}}|}\,. \tag{2.32}$$

$\boldsymbol{f}^i_{\mathrm{LF}} + \boldsymbol{f}^i_{\mathrm{pm}}$ can be formulated as

$$\boldsymbol{f}^i_{\mathrm{LF}} + \boldsymbol{f}^i_{\mathrm{pm}} = \boldsymbol{f}^i_{\mathrm{LF}} \left(1 - \frac{f_{\mathrm{pm}}}{f_{\mathrm{LF}}}\right)\,, \tag{2.33}$$

where the expression in parentheses does not influence the summation over the nodes, because $|\boldsymbol{f}_{\mathrm{LF}}|$ was assumed to be constant. This means, that a' in (2.18) can be replaced by

$$a = \frac{J\Phi_0}{\epsilon_1}\left(1 - \frac{f_{\mathrm{pm}}}{f_{\mathrm{LF}}}\right) \tag{2.34}$$

to account for the pinning force density without changing the rest. The result from the third equation in (2.18) solved for J reads

$$J = \frac{2\,\epsilon_1}{\Phi_0\, d_{\mathrm{gb}}}\, \hat{\boldsymbol{e}}^{\mathrm{end}}_{\mathrm{l,z}}\, \tan\varphi + \frac{f_{\mathrm{pm}}}{\Phi_0\sqrt{1-\hat{e}^2_{\mathrm{l,y}}}}\,. \tag{2.35}$$

This is exactly the same as (2.31), but in this form the similarity to the published results (2.7) and (2.11) [21] becomes more obvious. The z component of the tangent unit vector at the vortex end (where the vortex path leaves the LPR region) shows up in the "elastic term" containing ϵ_1, and the "pinning term" containing f_{pm} is now divided by $\sqrt{1-\hat{e}^2_{\mathrm{l,y}}}$ instead of $\cos\varphi$ or $\sqrt{\cos\varphi}$. If we assume, that in the limit of $\varphi \to 0$ the vortex line is approximately a half circle with a large radius (strictly $R \to \infty$ because $\Delta x \to \infty$ for $\varphi \to 0$), $\hat{\boldsymbol{e}}^{\mathrm{end}}_{\mathrm{l,z}} \to 1$, $\hat{e}_{\mathrm{l,y}} \to 0$, because the vortex length $L \to \infty$ and $\cos\varphi \to 1$ and the three results coincide.

The Lorentz force density sets with $f_{\mathrm{pm}} \le f_{\mathrm{LF}}$ a lower limit for the vortex length. For an unbent vortex $\hat{e}_{\mathrm{l,y}} = \sin\varphi$ (the same value as in the bulk) and the inequality reduces to $f_{\mathrm{pm}} \le \Phi_0 J \cos\varphi$. This is clearly fulfilled, when bending of the vortex takes

d_{gb} (nm)	ϵ_l (N)	f_{pm} (Nm^{-1})	f^*_{pm} (Nm^{-1})
10	$2.89 \cdot 10^{-13}$	$1.5 \cdot 10^{10}\,\Phi_0$	$4 \cdot 10^{11}$

Table 2.3: *Parameter values used in the example calculation for comparisons between the numerical iteration and the analytical result. The value for f^*_{pm} is large representing "infinite" HPR pinning.*

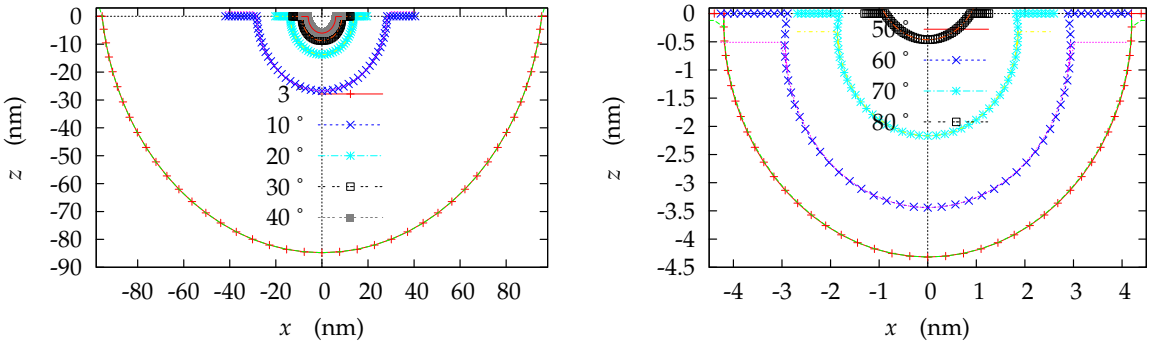

Figure 2.9: *Projection of vortex spirals calculated with the numerical iteration program on the xz plane for different magnetic field directions φ. For the parameters, see Table 2.3. Over the iteration results plotted with symbols half circles without symbols are drawn.*

place at all. The lower limit for the vortex length is the length of a straight vortex line as expected.

Comparison with the numerical iteration

The parameters applied in the example calculation for the comparison between the numerical iteration and the analytical result are summarised in Table 2.3. For f^*_{pm} an arbitrary, but large value was chosen that corresponds to "infinite" HPR pinning. The iteration was started with a straight vortex line.

Figure 2.9 illustrates the projections of the vortex spirals calculated with the numerical iteration on the xz plane for different values of φ. To compensate for the shape distortion of the plots, half circles are drawn over the vortex spirals without symbols. This demonstrates, that also the numerical iteration results are circular spirals to a good approximation.

The geometry of the vortex paths determined by the numerical iteration deviated in two respects from the circular spiral vortex with constant slope assumed in the analytical result. First, the vortex displacment Δz_{gb} differed up to about 20 %. The observed difference stays below about 6 % for intermediate angular values of φ from 30 ° to 60 ° and is maximal at the lowest ($\varphi = 3$ °) and highest φ values ($\varphi = 80$ ° for

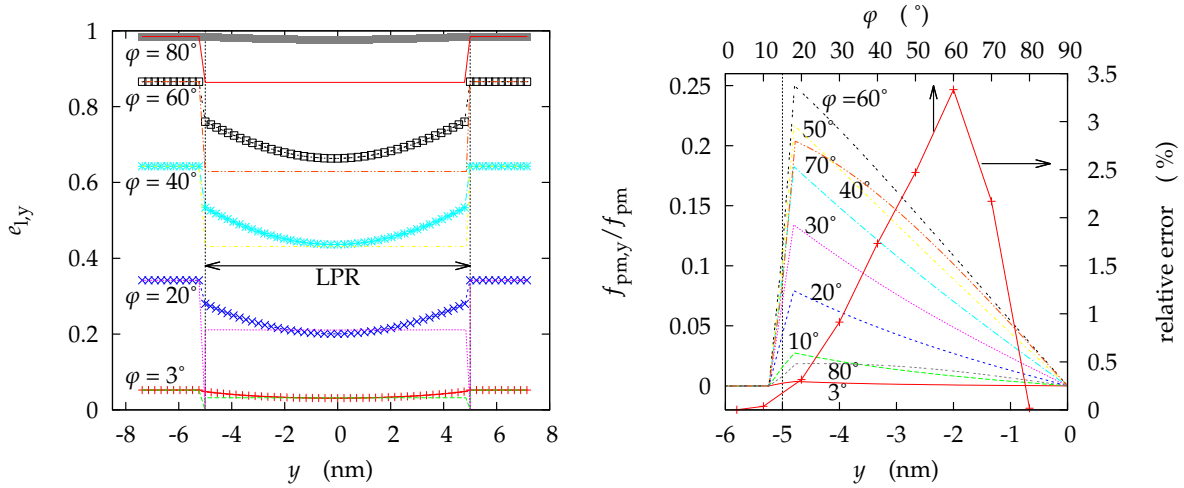

Figure 2.10: *Non-constant vortex spiral slope in the numerical iteration results. The left plot shows the y component of the tangent unit vector for several values of φ. The curves with symbols are evaluated from vortex spirals obtained with* $f_{pm} = 1.5 \cdot 10^{10}\,\Phi_0\,\mathrm{Nm}^{-1}$ *and the ones without symbols correspond to the zero LPR pinning case. The right graph contains the normalised y component of the pinning force density* $f_{p,y}/f_{pm}$ *in the negative y half space for all calculated rotational angles (without symbols).* $f_{p,y}(-y) = -f_{p,y}(y)$*. The curve with symbols is the angular dependence of the maximal relative error of* f_{pm} *calculated by (2.36) that results from setting* $f_{p,y}$ *to zero.*

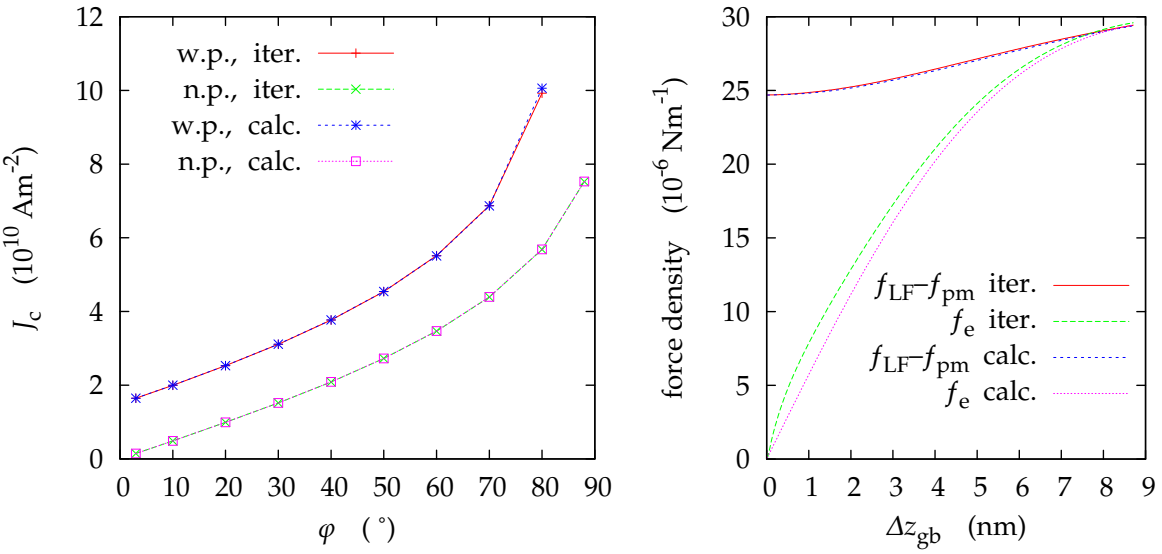

Figure 2.11: *The left plot shows a comparison of the calculated angular dependence of the critical current density. The graph compares data resulting from the numerical iteration ("iter.") and data calculated by the analytical solution ("calc."). "w.p." stands for "with pinning" and "n.p." corresponds to* $f_{pm} = 0\,\mathrm{Nm}^{-1}$*. The right graph compares the force densities logged during the numerical iteration with the calculated values from (2.23) and (2.24). The field direction for this example was* 30 °*. The force densities from the iteration are averaged over* 37 *points in the LPR.*

$f_{pm} = 1.5 \cdot 10^{10}\,\Phi_0\,\mathrm{Nm}^{-1}$ and $\varphi = 88\,^{\circ}$ for $f_{pm} = 0\,\mathrm{Nm}^{-1}$). The observed differences in Δz_{gb} are similar for the case of zero- and non-zero LPR pinning.

The second geometrical deviation is the non-constant vortex spiral slope in the numerical iteration results. It is only observed for non-zero f_{pm} values as shown in the left plot of Figure 2.10. The right graph of Fig. 2.10 contains the normalised y component of the pinning force density $f_{p,y}/f_{pm}$ in the negative y half space for all calculated rotational angles (without symbols). $f_{p,y}$ has an odd functional dependence on y, $f_{p,y}(-y) = f_{p,y}(y)$. The y component of the pinning force density calculated by the numerical iteration is largest at $\varphi = 60\,^{\circ}$, where it reaches about 25 % of f_{pm}, which seems a bit too large to be neglected, as is done in the analytical result. On the other hand the relative error between the full f_{pm} of the numerical result and the pinning force density calculated with $f_{p,y} = 0$,

$$\sqrt{\frac{f_{p,x}^2 + f_{p,y}^2 + f_{p,z}^2}{f_{p,x}^2 + f_{p,z}^2}} - 1 \approx \frac{1}{2}\frac{f_{p,y}^2}{f_{pm}^2 - f_{p,y}^2}\,, \tag{2.36}$$

usually amounts only to a few percent. It is plotted in the right graph of Fig. 2.10 with symbols. For the given example at $\varphi = 60\,^{\circ}$ this relative error is 3.3 %. From (2.36) follows, that even if $f_{p,y} = 0.4\,f_{pm}$ the relative error of the approximation $f_{p,y} = 0$ stays below 10 %. Furthermore the relative error estimate of 3.3 % was calculated for the maximum value of $f_{p,y}$ reached only at the boundary of the LPR region. For the most part of the calculated vortex line it will be smaller.

The second force directly affected by a nonzero $f_{p,y}$ is the elastic force density. $f_{e,y} = -f_{p,y}$, and because the modulus of f_e will (for relevant current densities) always be larger than f_{pm}, the relative error will be smaller than in the case of the pinning force density.

As can be seen in the left panel of Figure 2.10, $\hat{e}_{l,y}$ changes at certain angles up to an absolute value of about 0.1 along the vortex line if the iteration is started with a straight vortex. Also when $\hat{e}_{l,y}$ is not constant any more, it is still at least approximately connected to the vortex length.

The described differences between the numerical iteration results and the analytical description for infinite HPR pinning do not have a strong impact on the derived critical current densties. Figure 2.11 shows in the left panel a comparision between the angular dependence of J_c calculated in two different ways for the zero pinning case ("n.p." for "no pinning") and for an applied pinning force density of $f_{pm} = 1.5 \cdot 10^{10}\,\Phi_0\,\mathrm{Nm}^{-1}$. The curves resulting from the numerical iteration are

named "iter." and data calculated by the analytical solution (2.31) are named "calc.". The details of the evaluation of the analytical solution are given in the next section. The agreement between the numerical iteration J_c and the analytical result is very good. Except for single points, the difference stays below 0.2 %. The reason is explained by the right hand graph of Fig. 2.11. This graph compares the force densities f_e and f_{LF} logged during the numerical iteration for a single critical current density point at $\varphi = 30^\circ$ with f_e and f_{LF} evaluated with (2.23) and (2.24). In the calculation of f_{LF} with (2.24) the current density, $J = 3.11 \cdot 10^{10}\,\mathrm{Am}^2$ from the numerical iteration was used. The horizontal axis is the vortex displacement Δz_{gb}, which increases during the iteration. The pinning force density employed for plotting $f_{LF} - f_{pm}$ is in both cases the constant f_{pm} value from Table 2.3. The pinning force density was not logged during the iteration. The f_e and f_{LF} values for the numerical iteration are the arithmetic averages of the force density norms from 37 vortex nodes inside the LPR. The iteration was stopped, when the vectorial sum of all force densities of the same 37 vortex fell below a certain limit. At the end of the iteration the averaged force densities from the numerical iteration and the analytical force densities meet at one point. This means, that (2.24) and (2.23) resemble in good approximation the averaged force densities appearing along the vortex line during the numerical iteration. This behaviour was found only for numerical iterations performed with "infinite" HPR pinning. If a value of f_{pm}^* was considered, that was low enough to allow movement of vortices outside the LPR, the agreement was not satisfying.

It should be noted, that the sign of f_{pm} is connected to the magnetic hysteresis arising due to pinning. There are two vortex spiral configurations related to the same current density depending on how the current density was reached. Subtracting f_{pm} in (2.31) is appropriate for an increasing current density, which also corresponds to the experimental situation. By decreasing the current density from a larger value, the solution with the opposite sign of f_{pm} has to be realised. This interpretation was confirmed by the numerical program by starting the iteration once with a straight vortex line and a second time with a sufficiently large vortex spiral shrinking to the hysteretic solution.

Vortex breaking limit

The analytical result (2.31) for the current density is not of much use in the given general form. Even though the shape of the vortex line is fixed to be a circular spiral with constant slope, all combinations of R and k that fulfil (2.31) for a given

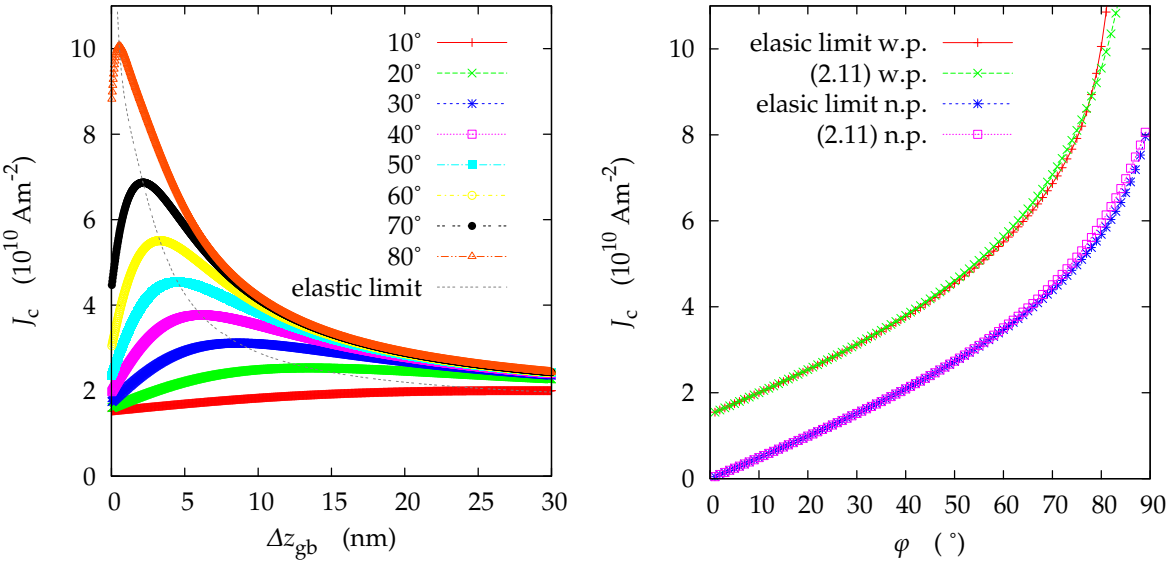

Figure 2.12: *The left plot shows critical current densities calculated with (2.31) and (2.30) for different field directions in dependence of the vortex elongation Δz_{gb}. The parameters listed in Table 2.3 with non-zero f_{pm} were used. The curve without symbols goes through the maxima of each J_c dependency and corresponds to the elastic limit critical current density. The right graph compares the elastic limit J_c evaluated for the pinning ("w.p." for "with pinning") and the zero pinning ("n.p." for "no pinning") case with (2.11).*

J are valid vortex geometries for this current density. This is quite obvious for the analytical result, but is also true for the numerical iteration algorithm.

This claim was tested by starting the iteration with a specific vortex spiral. For a given ϵ_l the starting configuration fixes $\hat{e}_{l,y}$ and f_e. The choice of a current density J determines f_{LF} and the development of the vortex line during the iteration. The vortex spiral will expand without limits, if the initial f_{LF} is larger than $f_e + f_{pm}$ derived for the starting configuration. The vortex line stays nearly unmodified, if the starting f_{LF} lies in between $f_e - f_{pm}$ and $f_e + f_{pm}$, and it shrinks, if f_{LF} is chosen to be smaller than $f_e - f_{pm}$. As long as there is a nonzero pinning force density, the vortex cannot shrink to a straight line. Therefore, also for the numerical iteration, one can easily construct more than one vortex spiral that are stable (or unstable) for one current density.

By starting the iteration with a straight vortex, the solutions that can be achieved are already restricted. Under this condition there is a single limiting value of the current density that is taken as J_c. Below and at J_c the vortex spiral is stable and for current densities above J_c the force equilibrium equation cannot be fulfilled any more. Jc is evaluated according to this criterion in the numerical iteration used in this

work and also in [21]. The critical current density defined in this way will be referred to as the *elastic limit* J_c or the *vortex breaking limit* J_c. The elastic limit critical current density does not necessarily correspond to the measured J_c, because it assumes an undisturbed expansion of the vortex spiral.

Taking only the analytical result, it is not clear, why an elastic limit should exist at all. For example, the force equilibrium (2.31) is a quadratic equation in $\sqrt{1-\hat{\epsilon}_{l,y}^2}$. The solution of this quadratic equation contains J and R and, as long as it exists at all, it defines a wide range of current densities and vortex radii, which fulfil the force equilibrium equation by construction. Like in the numerical case, without additional geometric restrictions, there are no reasons for a elastic limit and a vortex would be able to handle nearly every current density.

A quite successful and simple example of a geometrical assumption about the vortex line is, that it breaks after having developed about a half turn spiral. For this *half turn spiral solution* t_1 is equal to $\pi/2$ and constant. From the boundary conditions follows $R = \Delta x_{gb}$, $z_0 = 0$ and $k = d_{gb}/\pi$. Putting this into (2.25) results in

$$J_c = \frac{\epsilon_l}{\Phi_0 d_{gb}} \frac{\sin\varphi}{\sqrt{(\cos\varphi/2)^2 + (\sin\varphi/\pi)^2}} + \frac{2 f_{pm}}{\Phi_0} \frac{\sqrt{(\cos\varphi/2)^2 + (\sin\varphi/\pi)^2}}{\cos\varphi}. \quad (2.37)$$

This angular dependence of the critical current agrees very well with the fit to the numerical data given in [21]. Up to an angle φ of 80 ° it deviates by less than 4 % from (2.11). It also suffers from the same problems as (2.11). It diverges at $\varphi = 90$ ° and rises too steeply at $\varphi = 0$ °. The half turn solution already gives the correct hints about the behaviour of the calculated J_c angular dependence.

A second, more general assumption about the vortex geometry only requires that $0 \leq t_1 \leq \pi$ and employs (2.30). It produces about the same vortex configurations as the numerical iteration, but is more general, because it also includes a full turn spiral vortex at $\varphi = 90$ °. Δz_{gb} and Δx_{gb} define for a given ϵ_l and f_{pm} the actual shape of the vortex spiral, where Δx_{gb} is fixed by the field direction. This leaves Δz_{gb} as a free variable. Interestingly, the critical current density plotted versus Δz_{gb} by applying (2.31) with R and k from (2.30) has a single maximum as shown in the left panel of Figure 2.12. Again the parameters listed in Table 2.3 are used. With the geometrical restrictions for the vortex it is therefore plausible to define the elastic vortex breaking limit as the vortex configuration at the maximal critical current density. The elastic limit J_c, evaluated in this way with the analytical result, agrees well with the one derived with the numerical iteration (see left graph in Fig. 2.11) and also with (2.11)

as illustrated in the right panel of Fig. 2.12.

As can be seen in left panel of Fig. 2.12, $\Delta z_{gb} \rightarrow \infty$ for $\varphi \rightarrow 0\,^{o}$ for the elastic limit. For this limit $R \rightarrow \infty$ and $t_1 \rightarrow 90\,^{o}$. This is the same behaviour of the half turn solution (2.37), it is produced by the numerical iteration and it was also derived analytically for small values of φ in [21]. Although this is not a very realistic vortex spiral geometry, it seems to be typical for the elastic limit case. It is the reason for the corner like shape of the channeling minimum in the calculated J_c angular dependencies. According to (2.23), the elastic force denstiy goes to zero for $R \rightarrow \infty$, which suggests a straight vortex. For $\varphi \rightarrow 90\,^{o}$ it was found that $\Delta z_{gb} \rightarrow 0$, $R \rightarrow 0$ and $t_1 \rightarrow 180\,^{o}$. This corresponds to a straight vortex and is the reason for the divergence in this force free configuration. Again the elastic force density goes to zero. This behaviour seems to be typical for the elastic limit J_c, because it is also produced by the half turn solution and the numerical iteration.

It should be noted, that the vortex displacement Δz_{gb} at the J_c maximum coincides with the Δz_{gb} position of the minimum of the force density sum in (2.31). The force density sum was used in the evaluation of the Δz_{gb} values, in order to get solutions, where the force density sum goes to zero. The force density sum only is zero in the elastic limit case at its minimum, but, as long as the minium lies below zero, Δz_{gb} values can also be evaluated for smaller J_c values. One can also fix the value of Δz_{gb} and search for the possible current densities. This would correspond to an interpretation, where the vortex spiral cannot elongate in an undisturbed way. If the vortex line comes close to another vortex in the process of an elastic expansion, flux cutting and cross joining is likely to occur [3]. The elastic limit critcal current would never be realised in this case.

Because the geometrical restriction (2.30) is quite general and gives also good agreement with the numerical iteration, it is used for the interpretation of the data.

Evaluation of ϵ_l

In [21] it was suggested, that ϵ_l should be (in combination with f_{pm}) evaluated by a least square fit of (2.11) to the critical current density angular dependence. This does not work very well with the data presented in this work. First of all, as mentioned already, I refuse to consider f_{pm} a fit parameter. Despite the fact, that it does not make much sense to introduce a second pinning force density, there is also the problem, that the current density minima at $\varphi = 0\,^{o}$ are quite broad in some cases. With the relatively steep and corner like rise of (2.11) one ends up with very small values of

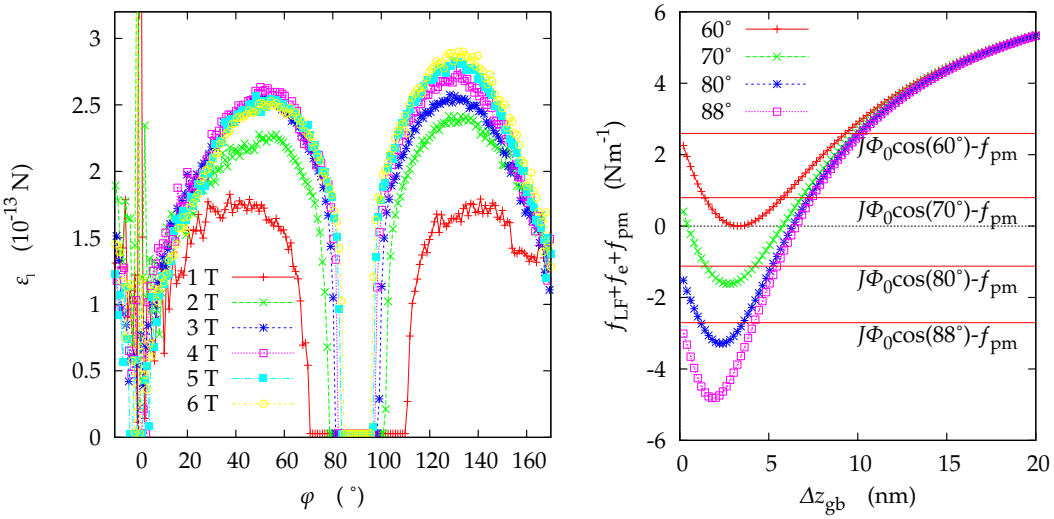

Figure 2.13: *The left plot shows angular dependence of ϵ_l calculated from a measured critical current density of a 90° track at 40 K. ϵ_l was evaluated at the elastic limit using (2.24) in combination with (2.30). The pinning force density was taken directly form the measured data at $\varphi = 0°$. The right plot explains why the ϵ_l values around $\varphi = 90°$ are missing. The force sums are calculated with the parameters of Table 2.3 and the current density $J = 5.51 \cdot 10^{10}\,\mathrm{Am}^{-2}$. The curve of the force sum starts at $\Delta z_{gb} = 0\,\mathrm{nm}$ with the value $J\Phi_0\cos(\varphi) - f_{pm}$ and decreases first because of the elastic contribution. If $J\Phi_0\cos(\varphi) < f_{pm}$, it is impossible to get for any positive value of ϵ_l a minimum at $f_{LF} + f_e + f_{pm} = 0$ as required for the elastic limit J_c.*

f_{pm}. A second problem with a curve derived from the elastic limit is, that it is not very likely to properly describe the angular dependence around $\varphi = 0°$ properly. Of course, the half turn solution cannot be correct for arbitrarily large vortex radii, because the vortex would not fit into the grain boundary any more. Note that for a half turn vortex spiral $R = \Delta x_{gb}$ and at φ =1.43°, 2.86° and 5.71° $\Delta x_{gb} = t_{film}$, $t_{film}/2$, $t_{film}/4$, where $t_{film} = 200\,\mathrm{nm}$ is the film thickness. At a magnetic induction B of 1 T the approximate vortex distance $\sqrt{\Phi_0/B} \approx 45\,\mathrm{nm}$, so there is room for four layers of vortices in the thin film. Therefore a half turn vortex spiral is unlikely to be realized below $\approx 5°$.

Another problem with a least square fit of the elastic limit curve (2.11) for ϵ_l is, that there are often some critical current density data points, situated above the calculated curve. This gets even worse, if one chooses to take f_{pm} below the J_c minimum at $\varphi = 0°$. The elastic limit curve should represent already the maximal possible critical current density resulting from pinning and from the elasticity of the vortices. Therefore there should be no J_c values above the elastic limit curve.

To account for these problems and to not restrict the result, the evaluation of ϵ_l was split up in serveral steps. First the force equilibrium equation (2.31) with R and

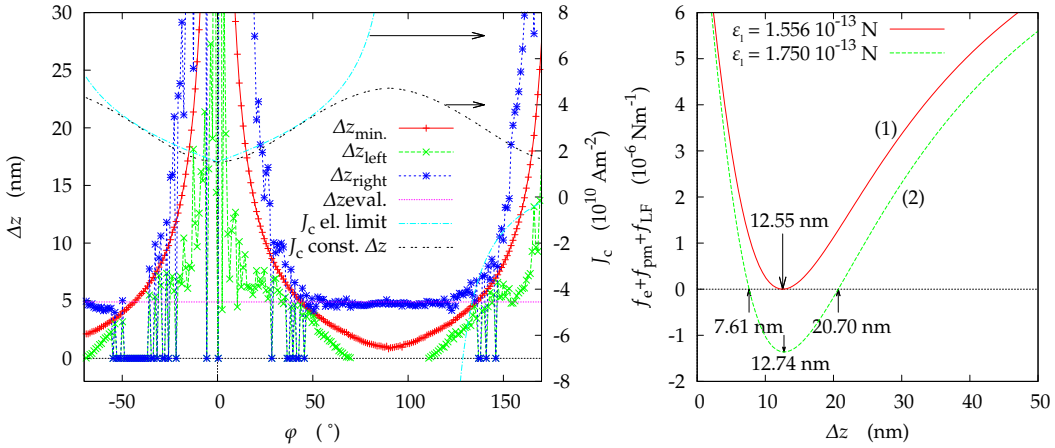

Figure 2.14: *The left graph shows an example of the evaluated* Δz_{gb} *values of the* J_c *measurement at* 1 T *and* 40 K *on a* 90° *track.* ϵ_l *was set to the maximum value of* $1.75 \cdot 10^{-13}$ N. *Plotted are the two solutions of the force density equilibrium equation,* Δz_{gb}^{left} *and* Δz_{gb}^{right} *both referring to the same current density. The middle curve is the* $\Delta z_{gb}^{min.}$ *value of the minimum of the force density sum.* Δz_{gb}^{right} *continues approximately* Δz_{gb}^{left} *and one can define a single* Δz_{gb} *value for the whole angular range. Also shown is the calculated critical current density predicted by the elastic limit (2.11) in comparison to the current density calculated with (2.31) and (2.30) by using the evaluated* Δz_{gb}. *On the right the force density equilibrium equation for a single point in the critical current angular dependence measured at* 1 T *and* 40 K *on a* 90° *track is plotted.* $f_{pm} = 3.156 \cdot 10^{-5}\,\mathrm{Nm}^{-1}$, $J = 2.117 \cdot 10^{10}\,\mathrm{Am}^{-2}$, $\varphi = 20.47°$ *and* $\epsilon_l = 1.56 \cdot 10^{-13}$ N *for curve "(1)" and* $\epsilon_l = 1.75 \cdot 10^{-13}$ N *for curve "(2)". Curve "(1)" represents an evaluation for the elastic limit where* ϵ_l *and* Δz_{gb} *was calculated for an extremal solution (first evaluation step). The maximum* ϵ_l *value was taken to plot curve "(2)" and evaluate the two* Δz_{gb} *values right and left of the minimum.*

k given by (2.30) is solved at the elastic limit for every J_c value of the experimental data. f_{pm} can be read directly off the current density angular dependence and is fixed for every measured curve leaving only ϵ_l as a variable. This results in an angular dependence of ϵ_l as an intermediate result, as shown for a measurement on an 90 ° track at 1–6 T and 40 K in the left graph of Figure 2.13. The value of the line energy derived in this way varies with φ and it is not constant as demanded by the model. Around $\varphi = 0$ ° the data is noisy, because the value of Δx_{gb} gets very large at low angles and it is not defined for $\varphi = 0$ °. In a certain angular range around $\varphi = 90$ ° the force equilibrium equation does not have a solution at the elastic limit and a meaningless small constant value is plotted in Fig. 2.13. This behavior is explained in the right illustration of Fig. 2.13. It is similar to the numerical iteration started with a straight vortex, where at sufficiently large angles the Lorentz force density acting on the straight vortex line falls below the pinning force density. Note that for $\Delta z_{gb} = 0$ the elastic force density is zero and (2.31) resembles the equation for a straight vortex with infinite vortex radius. Therefore, the force density sum starts at $\Delta z_{gb} = 0$ nm with the value of $J\Phi_0 \cos(\varphi) - f_{pm}$. If $J\Phi_0 \cos(\varphi) < f_{pm}$, it is impossible to get a minimum at $f_{LF} + f_e + f_{pm} = 0$ for any positive value of ϵ_l which would be required for the elastic limit J_c. The elastic term in (2.31) is negative, so the force density sum gets even more negative for small Δz_{gb}.

In a second step, the maximum of the calculated ϵ_l values is taken (ignoring the noisy part around $\varphi = 0$ °) as the constant ϵ_l for the whole angular range. The force density equilibrium plotted for a single point of the critical current density has now two solutions at two different values of Δz_{gb} (see right graph in Fig. 2.14). These two solutions are plotted for a critical current measurement at 1 T and 40 K on a 90 ° track in the left plot of Fig. 2.14. The lower value of Δz_{gb} is approximately continued by its larger value. This makes it possible to define a single Δz_{gb} for the whole angular range. The lower value of Δz_{gb} is zero at around 90 °, which would correspond to a straight vortex solution. By switching to the second solution of the force density equilibrium, one avoids the divergence of the current density at 90 °. Also shown is the current density for the elastic limit predicted by (2.11) in comparison to that calculated from (2.31) in combination with (2.30) using the constant Δz_{gb}. As expected, also the critical current of the elastic limit touches the curve for the constant Δz_{gb} current density where the three Δz_{gb} values meet.

Results and discussion

The measured critical current density can be fitted very well by the constant Δz_{gb} solution. In some cases the calculated current density deviates partly from the measured data, mainly because the measured curves are not symmetric around $\varphi = 0^{\circ}$. Still the rounding off at zero rotation angle and the critical current at the force free direction (where available) is predicted reasonably well. It became already clear from Figure 2.13, that for most of the curves two possible choices of the maximum ϵ_l exist: one in the angular range from 0° to 90° and a little bit larger one between 90° and 180°. Whichever maximum ϵ_l one picks, the corresponding slopes will be fitted best by the final constant Δz_{gb} curve. It is presumed, that the periodic asymmetry between -90° and 90° results from a slight misalignment of the sample in a way, that the magnetic field is not rotated perfectly parallel to the *ab* planes of the thin film. A second source of error in this evaluation comes from data, where only a relativly small part of the angular dependence can be attributed to the channeling minimum. The intermediate results for finding the maximum ϵ_l and Δz_{gb} are always noisy around $\varphi = 0^{\circ}$ leaving only a small part of the curves for determining the evaluation parameters. In this case some repetitive attempts by slightly varying the original parameters and checking on the final critical current density curves (which are never noisy) can still give satisfactory results.

The present evaluation suggests, that the measured angular dependence of the critical current density is not determined by the elastic limit of the vortices. A speculative scenario would be, that the expanding vortex gets close to another vortex pinned by a defect in the grain boundary, thus initiating a cutting/crossjoining process. In this case, the vortex elongation should show a dependence on the defect denstiy. Neutron irradiation allows the introduction of additional point defects in the material, where the defect density depends on the neutron fluence applied. One would expect, that the change of the average distance of the point defects is reflected by a decrease in the vortex elongation Δz_{gb}.

The evaluated line energy ϵ_l suffers from the same problem as the results published in [21], [12]. With the line energy estimate given in [21],

$$\epsilon_l \approx 0.38 \frac{\Phi_0^2}{4\pi\mu_0\lambda_{ab}^2} \tag{2.38}$$

and a temperature dependence $\lambda_{ab}(T) = \lambda_{ab}(0\,\mathrm{K})(1 - T/T_c)^{-1/2}$ one can fit the evaluated ϵ_l values at constant a magnetic field. $\lambda_{ab}(0\,\mathrm{K})$ was used as a fit parameter.

The largest values of $\lambda_{ab}(0\,\mathrm{K})$ are obtained by fits on the data of the 60° track and the lowest on data of the 30°. The fit results range from 3.3 up to 4.2 times the theoretical $\lambda_{ab}(0\,\mathrm{K})$ of 140 nm. As already ponted out in [21] most likely a more refined treatment of the vortex elasticity would be needed to resolve this descrepancy.

Tables and figures of the evaluation results

B (T)	T (K)	Φ_{gb} (°)	f_{pm} (10^{-6} Nm^{-1})	ϵ_l (10^{-13} N)	Δz_{gb} (nm)	Remark
1	40	90	31.56	1.75	4.89	Fig. 2.15
2	40	90	20.86	2.23	4.67	Fig. 2.15
3	40	90	16.41	2.54	4.80	Fig. 2.15
4	40	90	13.44	2.60	4.80	Fig. 2.15
5	40	90	11.70	2.53	4.80	Fig. 2.15
6	40	90	9.991	2.50	4.80	Fig. 2.15
1	50	90	18.41	1.45	4.74	Fig. 2.15
2	50	90	11.21	1.81	4.62	Fig. 2.15
3	50	90	7.942	1.94	4.62	Fig. 2.15
4	50	90	6.268	1.99	4.62	Fig. 2.15
5	50	90	5.103	1.98	4.65	Fig. 2.15
6	50	90	4.518	1.91	4.65	Fig. 2.15
1	60	90	9.859	0.958	4.60	Fig. 2.16
2	60	90	4.860	1.25	4.64	Fig. 2.16
3	60	90	3.678	1.25	4.64	Fig. 2.16
4	60	90	2.844	1.22	4.64	Fig. 2.16
5	60	90	2.114	1.18	4.82	Fig. 2.16
6	60	90	1.958	1.17	4.75	Fig. 2.16
1	70	90	3.700	0.524	4.73	Fig. 2.16
2	70	90	1.779	0.595	4.08	Fig. 2.16
3	70	90	1.279	0.571	4.19	Fig. 2.16
4	70	90	1.134	0.523	3.90	Fig. 2.16
5	70	90	0.8062	0.49	4.39	Fig. 2.16
6	70	90	0.6341	0.455	4.58	Fig. 2.16
1	80	90	0.8696	0.11	4.34	Fig. 2.17
2	80	90	0.3485	0.108	4.28	Fig. 2.17
3	80	90	0.2769	0.0836	4.42	Fig. 2.17
4	80	90	0.2455	0.0667	4.03	Fig. 2.17
5	80	90	0.2341	0.0462	3.29	Fig. 2.17
6	80	90	0.2455	0.0318	3.31	Fig. 2.17

Table 2.4

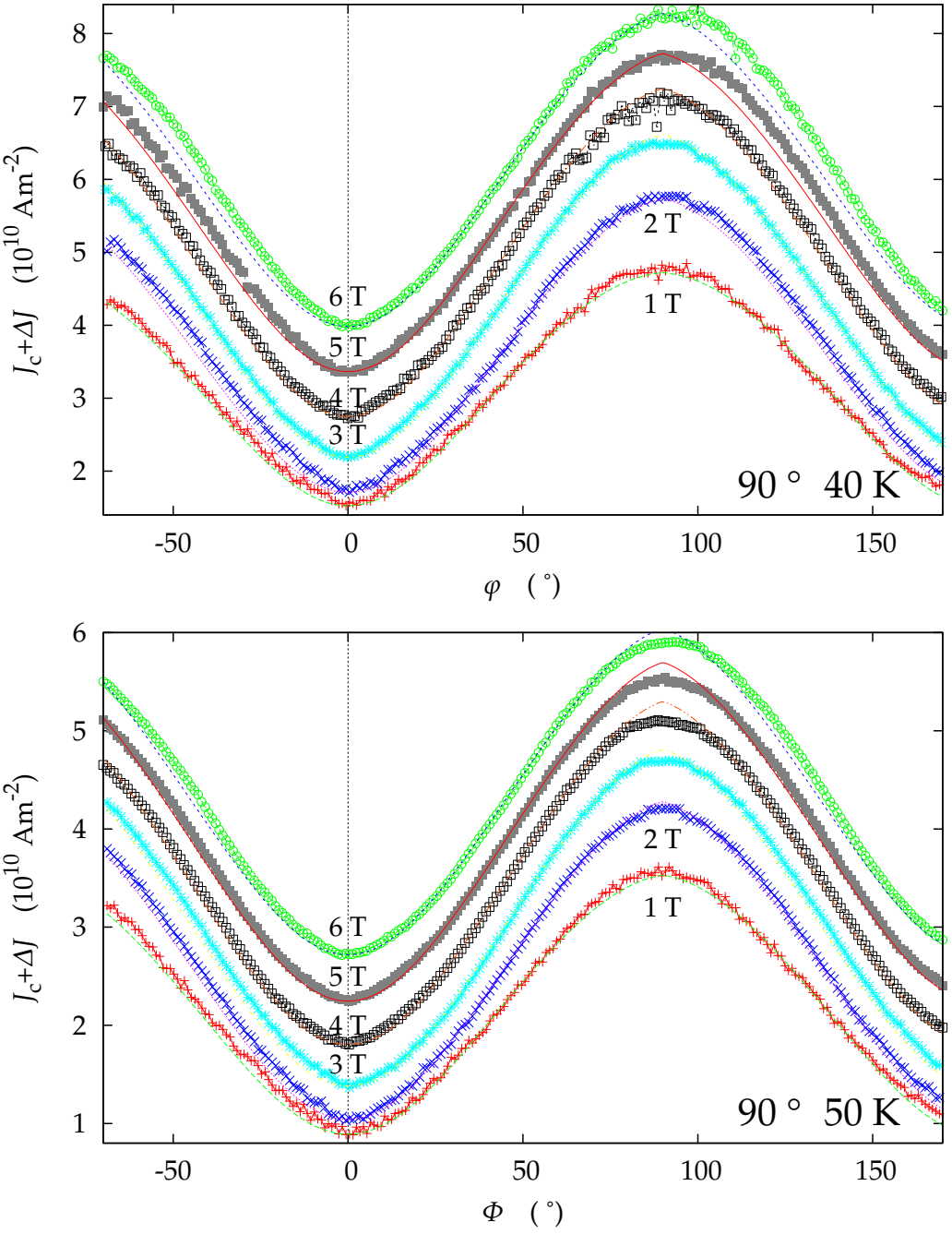

Figure 2.15: *Measured critical current density on a* 90° *track at* 40 *and* 50 K *each from* 1–6 T *(symbols) and the calculated current density following from the evaluation (without symbols). The curves are shifted in y direction for better comparison.*

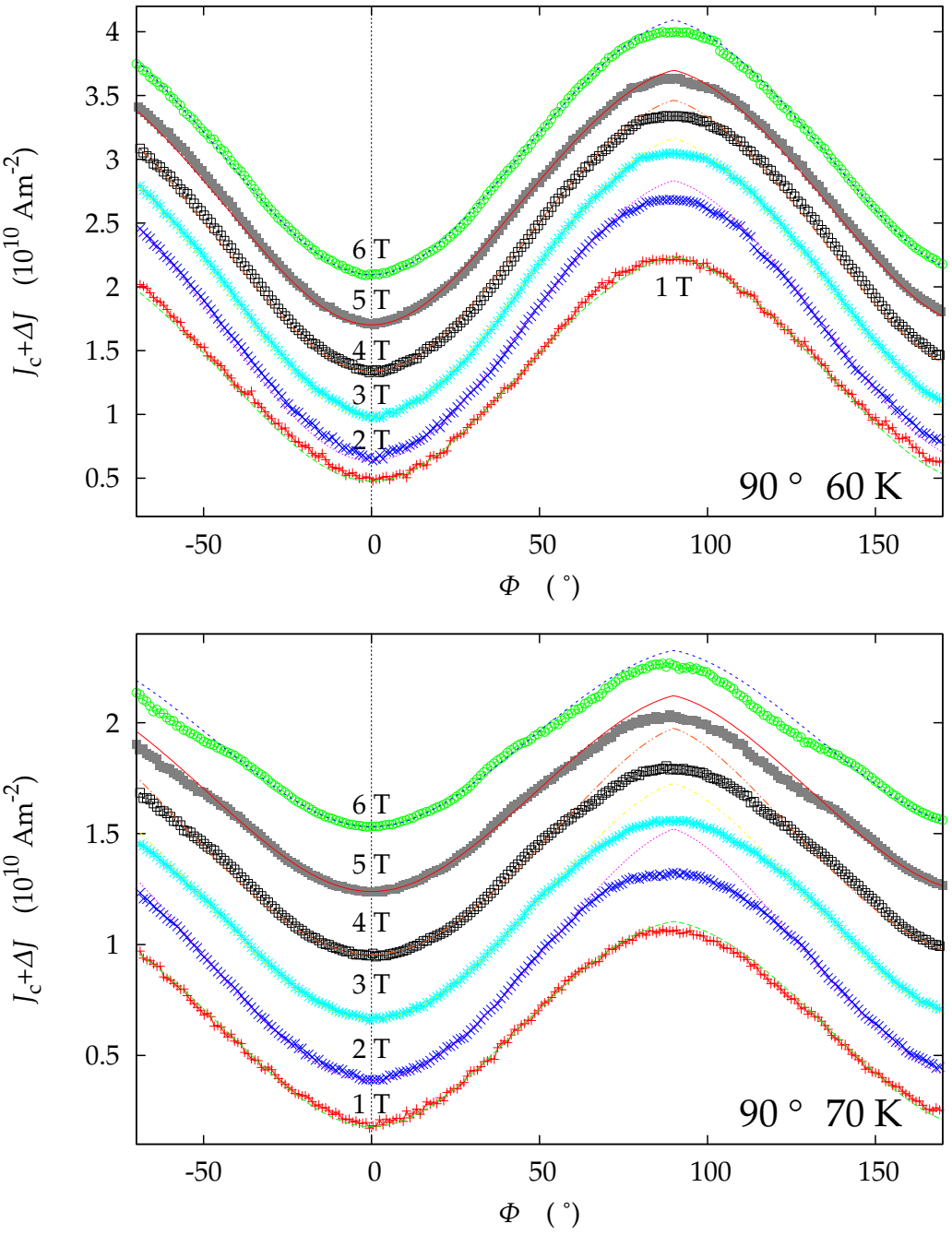

Figure 2.16: *Measured critical current density on a 90° track at 60 and 70 K each from 1–6 T (symbols) and the calculated current density following from the evaluation (without symbols). The curves are shifted in y direction for better comparison.*

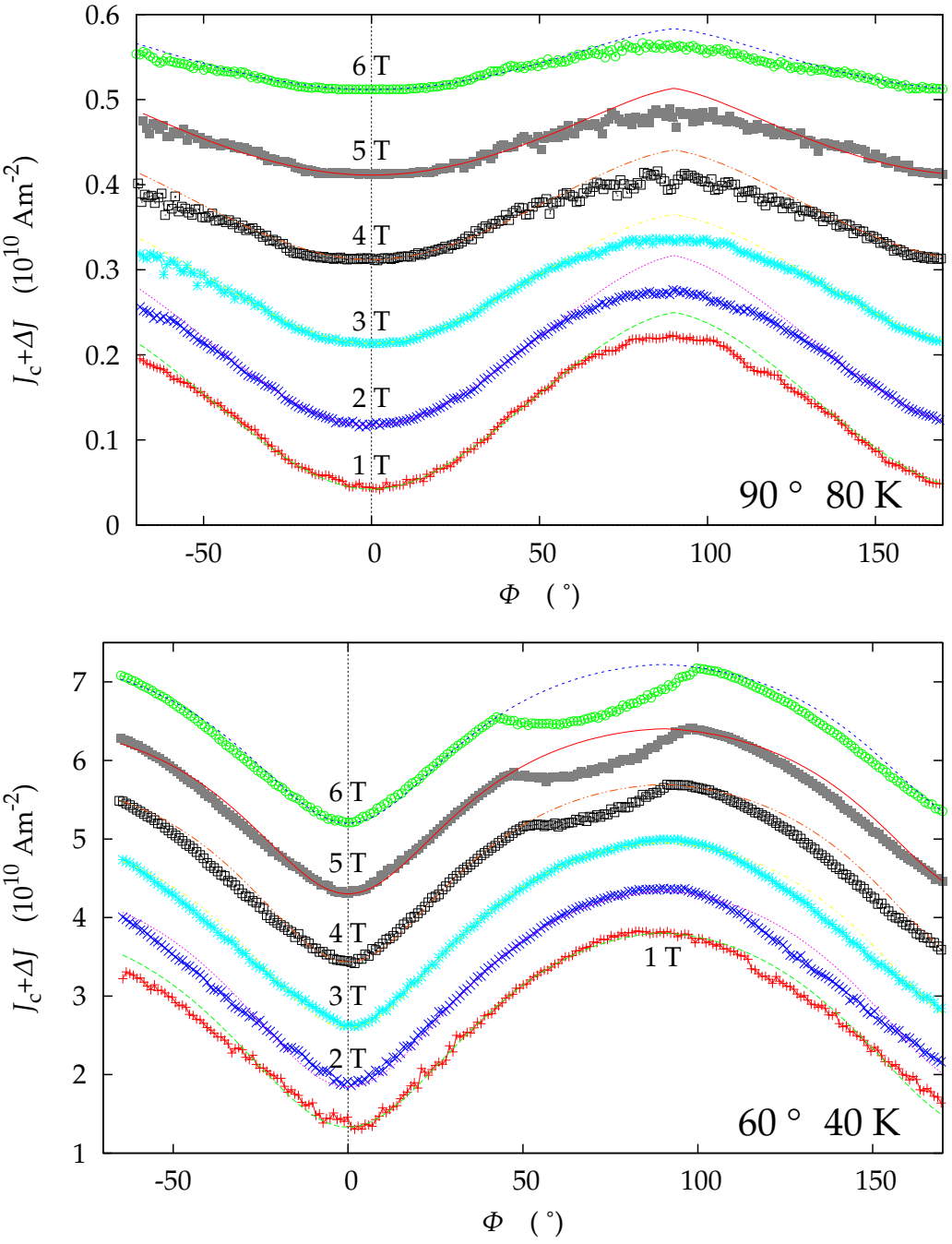

Figure 2.17: *Measured critical current density on a* 90° *track at* 80 K *and a* 60° *track at* 40 K *each from* 1–6 T *(symbols) and the calculated current density following from the evaluation (without symbols). The curves are shifted in y direction for better comparison.*

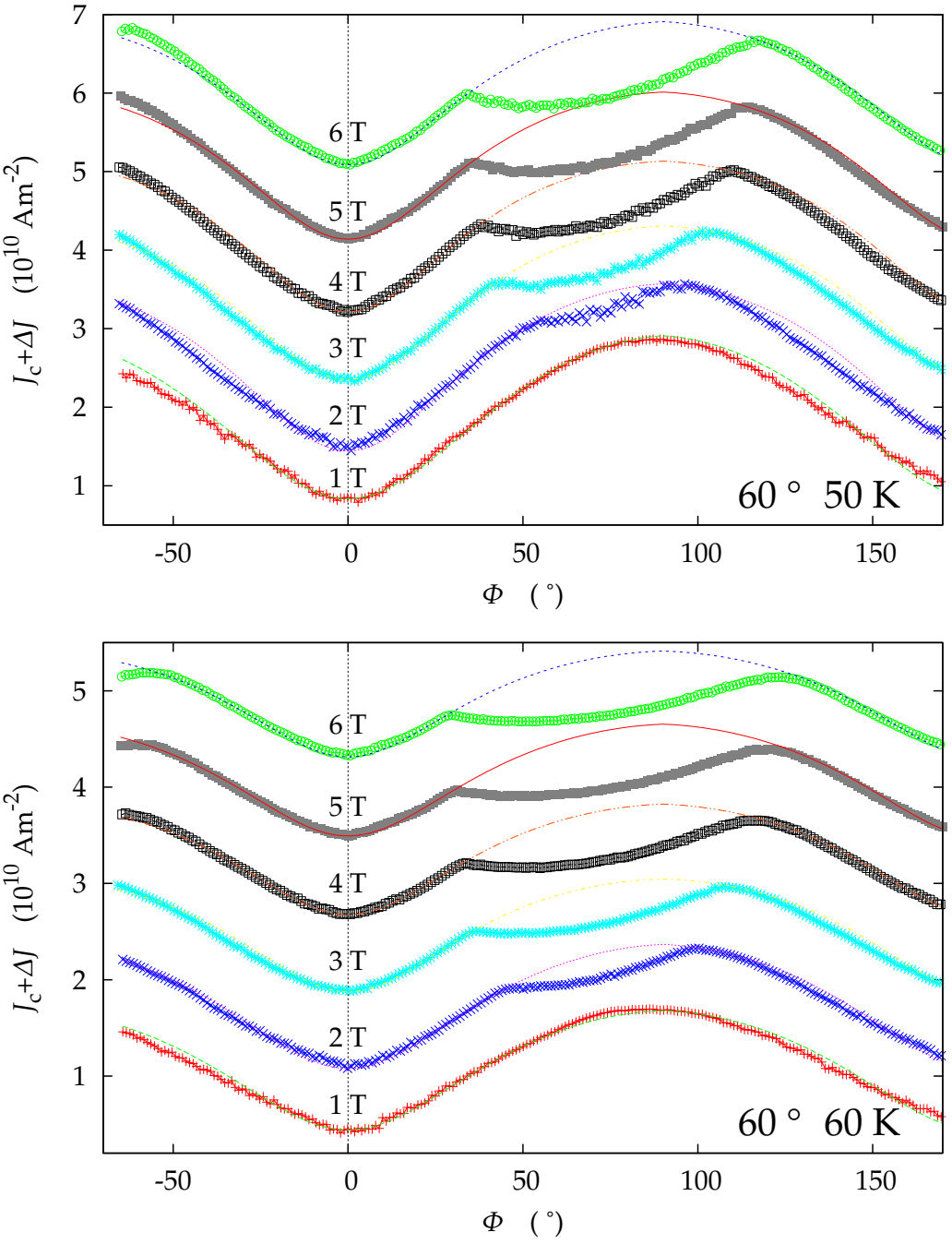

Figure 2.18: *Measured critical current density on a* 60° *track at* 50 *and* 60 K *each from* 1–6 T *(symbols) and the calculated current density following from the evaluation (without symbols). The curves are shifted in y direction for better comparison.*

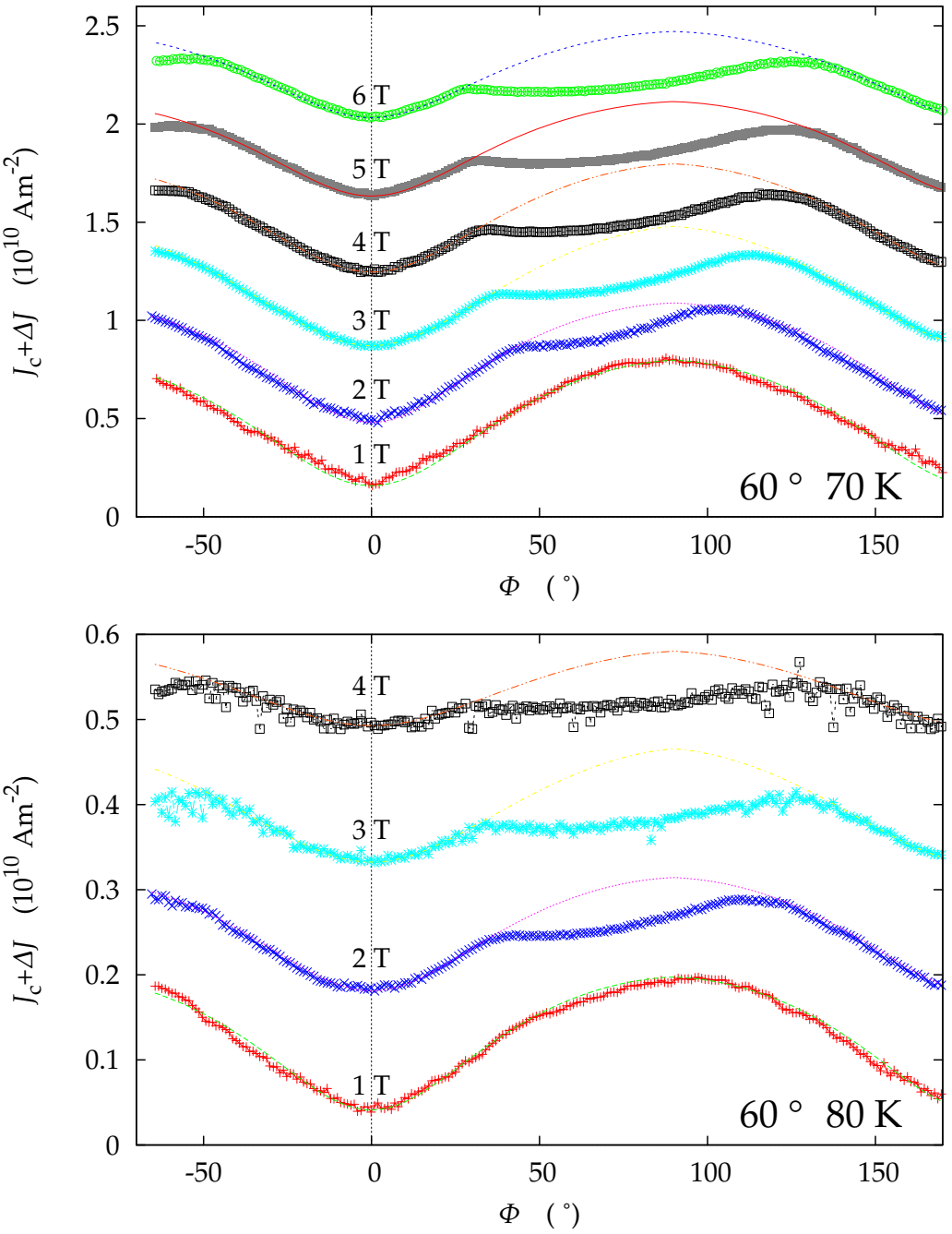

Figure 2.19: *Measured critical current density on a 60° track at 70 and 80 K each from 1–6 T (symbols) and the calculated current density following from the evaluation (without symbols). The curves are shifted in y direction for better comparison.*

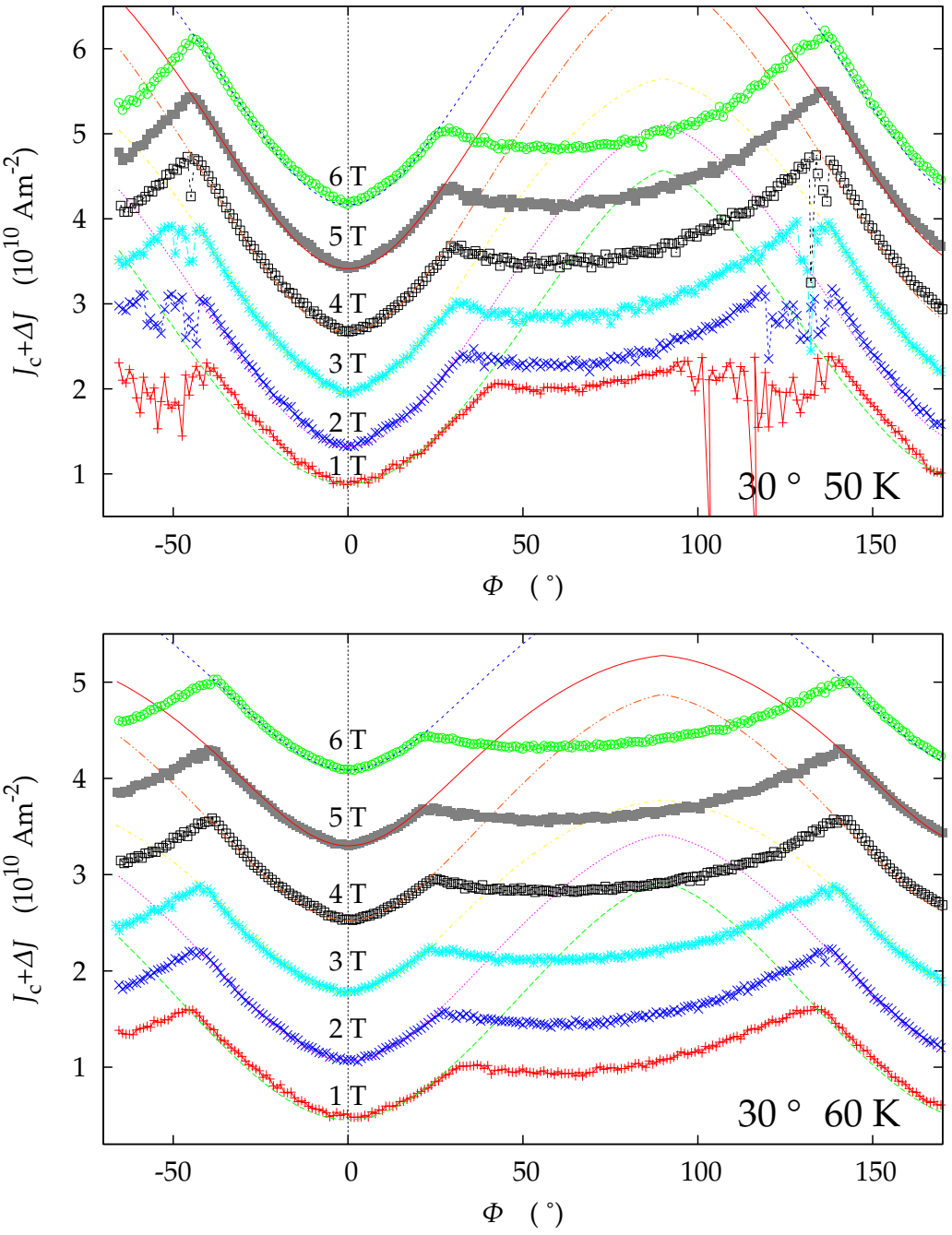

Figure 2.20: *Measured critical current density on a* 30° *track at* 50 *and* 60 K *each from* 1–6 T *(symbols) and the calculated current density following from the evaluation (without symbols). The curves are shifted in y direction for better comparison.*

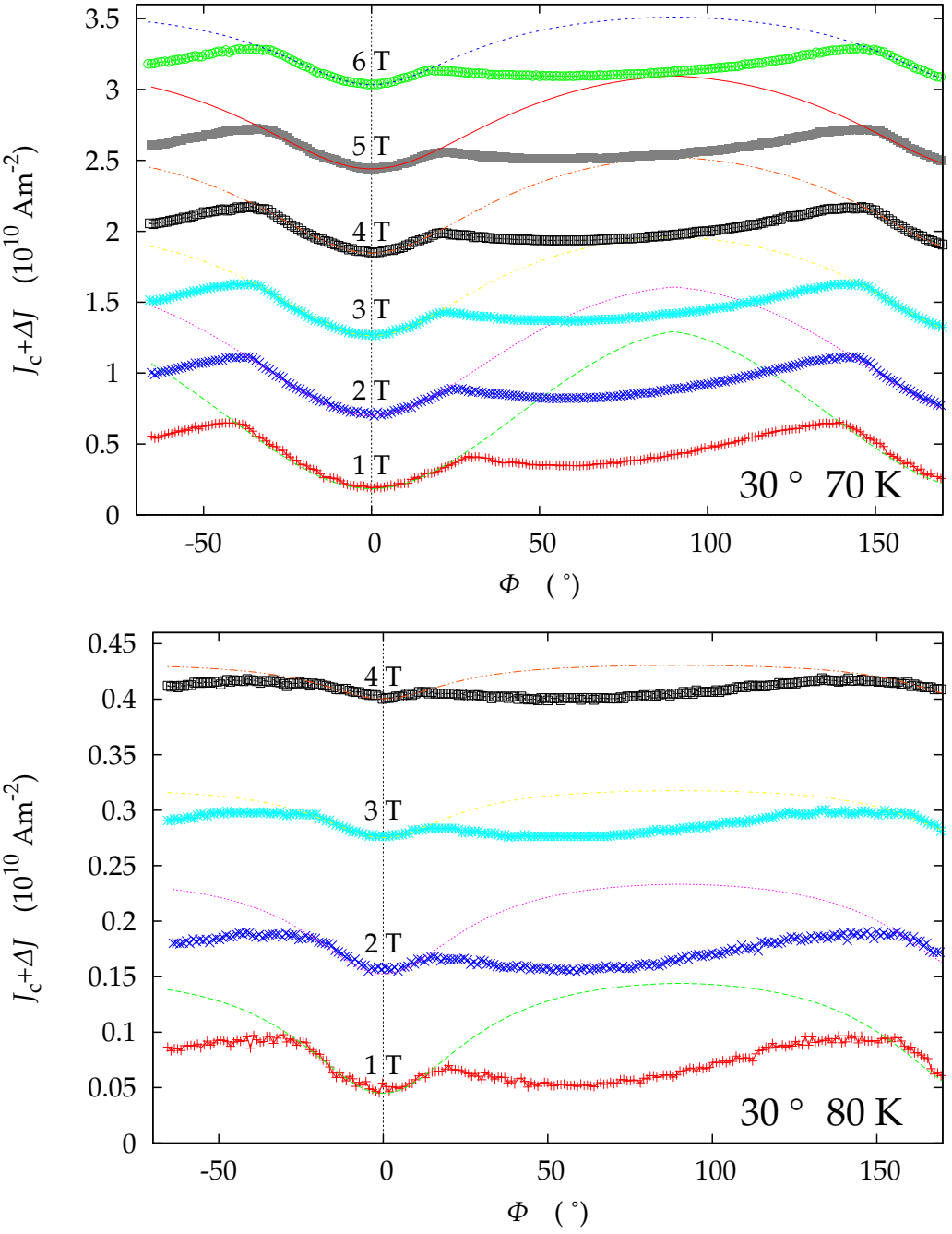

Figure 2.21: *Measured critical current density on a 30° track at 70 and 80 K each from 1–6 T (symbols) and the calculated current density following from the evaluation (without symbols). The curves are shifted in y direction for better comparison.*

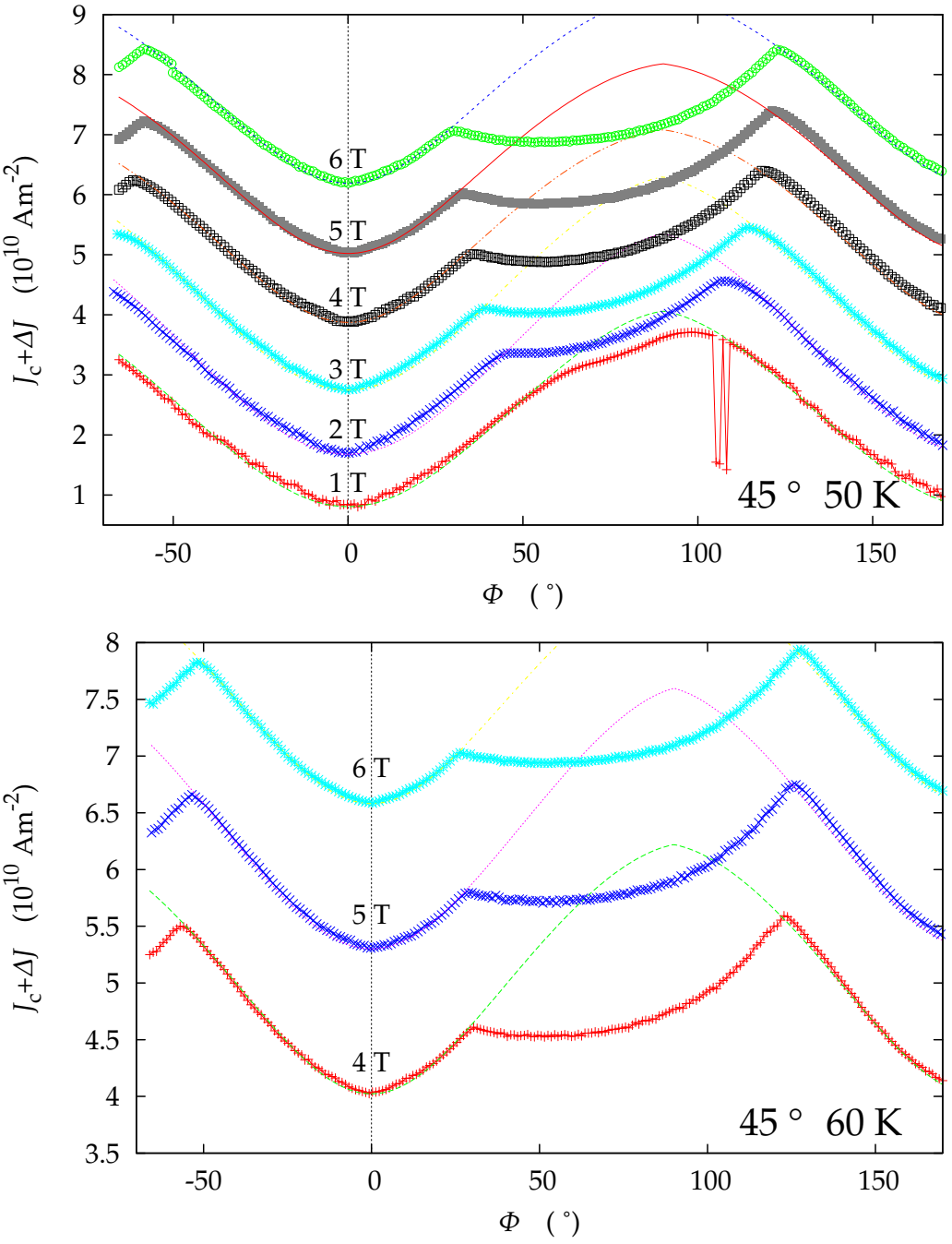

Figure 2.22: *Measured critical current density on a* 45 ° *track at* 50 K *from* 1–6 T *and* 60 K *each from* 4–6 T *(symbols) and the calculated current density following from the evaluation (without symbols). The curves are shifted in y direction for better comparison.*

B (T)	T (K)	Φ_{gb} (°)	f_{pm} (10^{-6} Nm^{-1})	ϵ_l (10^{-13} N)	Δz_{gb} (nm)	Remark
1	40	60	27.53	1.78	6.68	Fig. 2.17
2	40	60	18.47	1.95	7.16	Fig. 2.17
3	40	60	14.47	1.94	7.54	Fig. 2.17
4	40	60	12.13	1.93	7.82	Fig. 2.17
5	40	60	10.39	1.81	7.87	Fig. 2.17
6	40	60	9.321	1.72	7.75	Fig. 2.17
1	50	60	17.28	1.35	5.86	Fig. 2.18
2	50	60	9.581	1.66	7.02	Fig. 2.18
3	50	60	8.118	1.57	7.24	Fig. 2.18
4	50	60	5.648	1.61	7.57	Fig. 2.18
5	50	60	4.569	1.53	7.33	Fig. 2.18
6	50	60	3.876	1.47	7.21	Fig. 2.18
1	60	60	9.119	0.868	6.32	Fig. 2.18
2	60	60	4.725	0.972	6.72	Fig. 2.18
3	60	60	3.620	0.967	7.43	Fig. 2.18
4	60	60	2.586	0.923	7.18	Fig. 2.18
5	60	60	1.940	0.915	7.00	Fig. 2.18
6	60	60	1.337	0.909	7.39	Fig. 2.18
1	70	60	3.279	0.459	6.41	Fig. 2.19
2	70	60	1.666	0.482	7.08	Fig. 2.19
3	70	60	1.478	0.416	5.93	Fig. 2.19
4	70	60	0.9626	0.407	6.48	Fig. 2.19
5	70	60	0.6947	0.375	6.90	Fig. 2.19
6	70	60	0.6719	0.339	6.82	Fig. 2.19
1	80	60	0.8510	0.118	6.80	Fig. 2.19
2	80	60	0.4355	0.0982	6.52	Fig. 2.19
3	80	60	0.2563	0.0868	5.55	Fig. 2.19
4	80	60	0.2658	0.0565	5.55	Fig. 2.19

Table 2.5

B (T)	T (K)	Φ_{gb} (^{o})	f_{pm} (10^{-6} Nm^{-1})	ϵ_l (10^{-13} N)	Δz_{gb} (nm)	Remark
1	50	30	18.25	1.78	3.88	Fig. 2.20
2	50	30	10.63	2.21	4.83	Fig. 2.20
3	50	30	7.133	2.44	5.62	Fig. 2.20
4	50	30	5.588	2.51	4.95	Fig. 2.20
5	50	30	4.423	2.46	5.33	Fig. 2.20
6	50	30	3.410	2.44	5.56	Fig. 2.20
1	60	30	9.402	1.30	4.28	Fig. 2.20
2	60	30	5.473	1.45	5.18	Fig. 2.20
3	60	30	3.486	1.44	6.25	Fig. 2.20
4	60	30	2.608	1.48	5.27	Fig. 2.20
5	60	30	2.074	1.41	6.17	Fig. 2.20
6	60	30	1.760	1.38	5.71	Fig. 2.20
1	70	30	3.820	0.631	4.73	Fig. 2.21
2	70	30	2.088	0.624	5.97	Fig. 2.21
3	70	30	1.313	0.587	7.57	Fig. 2.21
4	70	30	0.9737	0.547	7.23	Fig. 2.21
5	70	30	0.8368	0.507	6.83	Fig. 2.21
6	70	30	0.6924	0.453	8.66	Fig. 2.21
1	80	30	0.9273	0.101	9.59	Fig. 2.21
2	80	30	0.4648	0.0897	10.4	Fig. 2.21
3	80	30	0.3131	0.0534	11.9	Fig. 2.21
4	80	30	0.2153	0.0388	12.2	Fig. 2.21

Table 2.6

B (T)	T (K)	Φ_{gb} (^{o})	f_{pm} (10^{-6} Nm^{-1})	ϵ_l (10^{-13} N)	Δz_{gb} (nm)	Remark
1	50	45	16.67	1.71	4.36	Fig. 2.22
2	50	45	9.893	2.01	4.43	Fig. 2.22
3	50	45	7.197	2.05	4.73	Fig. 2.22
4	50	45	5.644	2.05	5.40	Fig. 2.22
5	50	45	4.569	2.03	5.42	Fig. 2.22
6	50	45	3.966	1.92	5.43	Fig. 2.22
4	60	45	2.551	1.36	5.14	Fig. 2.22
5	60	45	2.084	1.34	4.72	Fig. 2.22
6	60	45	1.678	1.29	5.14	Fig. 2.22

Table 2.7

Chapter 3

Two axis probe

3.1 Introduction

The transport measurements are all performed with a standard four probe configuration, where the current leads are separated from the voltage wires.

The setup in use was originally designed to characterise the transport anisotropy of superconducting tapes. To measure the angular dependence of the critical current the available maximum magnetic field of 6 T is sufficient. The magnetic field orientation of the split coil magnet is horizontal. Rotational measurements at a maximum Lorentz force configuration (magnetic field perpendicular to the transport current) can be performed relatively easily by rotating the whole probe in the variable temperature insert (VTI). In this case the sample is mounted vertically and the inner diameter of the sample space (30 mm) does not limit the sample length.

The main part of this thesis was to design and build a two axis probe allowing to orient a sample in arbitrary orientation relative to the magnetic field.

3.2 Initial design considerations

The basic design criteria can be summarised as follows

- Two axes for the orientation of the sample.
- Fully automated measurement process because of the extended parameter space (temperature, magnetic field, two angles).

- Incorporation in the current measurement setup. Especially the existing probe for tape samples should still be fully operatonal and exchanging the probes should be easy.
- Variable probe length to make it adaptable to different VTIs.

The technically equivalent goniometer presented in [16] was designed with similar objectives as the one built in this thesis. The goniometer head in [16] is built up of a fixed frame hosting the whole rotation mechanics. With the horizontal axis the second rotational axis perpendicular to the sample surface is tilted. This mechanically complex configuration was chosen because the probe is operated in a cryostat with a vertical field orientation (solenoid) and the sample space diameter is about 50 mm. In our case the much smaller sample space diameter of the VTI dictated simpler mechanics of the head. Due to the horizontal magnetic field it was possible to realise one rotational axis by rotating the whole probe. So only the movement of the horizontal axis had to be built into the goniometer head. It was decided to make the sample stage normal perpendicular to the horizontal axis. This simplified the construction of the horizontal axis and was expected to make the mounting and contacting of a sample easier. When contacting a sample the probe usually lies horizontally on a table and the sample stage can also be rotated to be horizontal. In addition with this design it would still be possible to screw a small metal block onto the sample stage to tilt the sample normal towards the horizontal rotational axis. Originally it was planned to manufacture the hole goniometer head from brass to avoid any mechanical problems due to different temperature expansion coefficients of the materials. During the manufacturing process it was decided to make the frame from stainless steel and only the horizontal axis from brass. The stainless steel frame was chosen to improve the mechanical stability and robustness of the goniometer head. The relatively complicated horizontal axis was built from brass to simplify the machining of its parts. The mixture of brass and stainless steel proved to work without mechanical problems.

The sample stage itself was to a certain degree inspired by [16]. The temperature sensor (in our case a Cernox sensor with a copper case) is located directly below the sample inside the sample stage. Like in [16] it is possible to heat the sample stage by a resistive heater. The sample stage is in direct contact with the sample and should determine the sample temperature. It should have a high thermal conductivity to ease the heat exchange between the sample and the sensor. This was another argument to build the horizontal axis from brass: The low thermal conductivity of

stainless steel rules out to use it as a material for the sample stage. A combination of a stainless steel frame with a copper sample stage for the horizontal axis seemed to be too complicated and using only copper for the horizontal axis would have increased the difference of the thermal expansion coefficients between the head frame and the axis even further (linear thermal expansion coefficient of brass $\approx$19 μm/K, of stainless steel $\approx$19 μm/K). In addition copper is relatively ductile and not easy to machine. Brass was considered to be a reasonable compromise. In the very first version each axis was also equipped with a Hall probe. The Hall-probe for the horizontal axis was placed in the same housing as the heater with the active area perpendicular to the sample surface.

The wiring of the probe is first of all determined by the devices in the probe. In the original design it was planned to incorporate two Hall probes (at least two current wires and four voltage wires), a Cernox temperature sensor (two current and two voltage wires) and a sample heater (two current wires). For the sample one current and two voltages lines (two current wires and four voltage wires) were foreseen. The default sample voltage would be connected to the nanovoltmeter and the second one could be used to gain extra information like the contact resistance of one contact. This sums up to eight current lines and ten voltage lines. The electrical connections to the probe have to be plug-able and are realised by vacuum tight 10-way low temperature PEEK (polyetheretherketone) connectors. Two of them are necessary. The default sample voltage lines should go from the sample to the nanovoltmeter directly avoiding plugs and soldering connections as much as possible. In this way it was expected to improve the voltage signal quality. These two voltage cables are supported by an extra vacuum tight feed through. From previous experience on other transport probes in use at our lab, all voltage lines were realized with ultra miniature coaxial cables from Lakeshore. Two highly flexible types with stranded conductors of these cables are available, one with copper strands for low conductor resistance and one with stainless steel strands for lower thermal losses. These cables are designed for use at low temperatures. The low resistance copper cables are used for the sample voltages to keep the Nyquist noise as small as possible. The Hall probes and the temperature sensor are measured with a digital multimeter with a minimal voltage resolution in the order of microvolts, so stainless steel cables can be used (the resistance of the stainless steel cables at room temperature over the length of the probe is of the order of 100 Ω). The shielding of all coaxial cables was connected together at the top of the probe and accessible at a pin of the 10-way PEEK connector. In the first approach, the current wiring was done with pairwise

twisted varnish coated copper wires. To protect the wiring and also to make it simpler to bring the wires into the probe the whole wiring was distributed into several PTFE (polytetrafluoroethene, Teflon) hoses. At the bottom of the probe the wires are soldered to terminal tags screwed to a plastic plate.

The wiring for the sample, the temperature sensor, the heater and a Hall probe is situated inside the horizontal axis and will move relative to the rest of the sample head during operation. Therefore also the electrical connections to the devices will be permanently moved at low temperatures, making them less durable. The first approach was to connect the temperature sensor and Hall probe wires directly to the terminal board and to put them together with the sample wiring into a shrink hose for protection. There are basically two solutions for the wiring between the moving devices and the terminal plate on the probe, an open and a closed wiring. In the open wiring long wires enter the sample space directly from the top, where as in a closed wiring the wires are led through a closed channel to the height of the horizontal axis and enter axially the sample space. The simpler open wiring approach was not chosen, because it was considered to be too error-prone with the arrangement of the bevel gears given in the present design. It was expected, that long wires not restricting the movable angular range, will also easily get caught by the gear wheels and might break. In the probe design the wires are led through a hole in a side part of the goniometer head down to the horizontal axis. They enter the sample space at the height of the rotation axis. With small modifications it would still be possible to combine this closed wiring with an open one, at least for the sample connections. This could for example be desirable when high sample currents (several amperes) are required. Some simple kind of guidance to keep the wires away from the gears could prevent them from being caught by the bevel gears.

Two stepper motors with a reduction gear box are used to drive the two axis of the probe. Stepper motors can easily be controlled by a computer, the gear box provides a high angular resolution and high torque of the drives and stepper motors can hold their axis at a certain position. The limited rotational speed of stepper motors is not important for the present application because it does not require a fast positioning of the sample. For the mechanical transfer of the rotation down to the horizontal axis one finds different approaches in the literature, like worm gears [16], strings and bevel gears. A worm gear would save space, because it can be situated beside the sample space and it would fix the position of the gear wheel by its design. One disadvantage is the off centered axis, which would have required some extra guidance because of the length of the probe. Another difficulty might be to get a

worm gear with proper dimensions (the probe described in [16] utilizes custom worm gears designed and built for this probe). Using a string reel combination also saves space but the not predictable length variation of the string due to the combination of varying string tension and temperature in the given application would make a angular position feedback of the horizontal axis unavoidable. A high resolution angular position feedback with a resolution below 0.1^{o} was considered to be too complicated in the low temperature environment and therefore ruled out. In the current design a centered vertical axis transfers the rotation down to the sample space and the vertical rotation is turned to a horizontal one by two bevel gears. The vertical axis is protected and guided by an extra stainless steel pipe inside the shaft and the bevel gears are slightly modified standard gears used in technical model-making. This design was considered to be simpler than a worm gear solution and in addition the bevel gears were low cost and instantly available.

3.3 Current design

In this section the current design of the probe is described and discussed.

3.3.1 Top mount

The top mount connects the probe mechanically with the VTI and axially stabilises and rotates the probe shaft. It is manufactured from aluminium and consists of round, about 10 mm thick plate, carrying one stepper motor with a tooth belt drive, a belt spanner and the limit switches. The metal plate has a hole for the transfer-tube, which has to be aligned with the helium input port of the cryostat, when the probe is mounted in the VTI. A conical aluminum part is screwed on to the bottom of the plate. It ends in a KF40 small flange for mounting the probe to the VTI. Its axially centred bore hole contains two well separated ball bearings to ensure the axial stability of the probe shaft. Directly accessible below the lower ball bearing sits a vacuum tight shaft seal. The length of the probe reaching into the VTI can be adjusted by shifting it up or down in the ball bearings. The vertical position is fixed with a metal clamp above the top ball bearing. Attached to this metal clamp resides the toothed wheel for the tooth belt transferring the rotation from the stepper motor to the shaft. Two grub screws at the circumference of the metal clamp at different height are arranged to operate the limit switches.

3.3.2 Probe shaft

The body of the probe shaft is made from stainless steel to reduce thermal losses and to ensure its mechanical stability. It is built up of two stainless steel tubes, a short top piece, that tightly fits into the ball bearings with its diameter, and a longer thinner tube at the bottom. Inside this body, there are two other stainless steel tubes with smaller diameter extending over the whole length of the probe. The innermost tube is the vertical axis transferring the rotation of the second stepper motor down to the two axis head. He gas can flow through the vertical axis to improve the cooling of the shaft when the probe is operated. It is surrounded by another stainless steel tube to protect the axis rotation. PTFE tubes containing the wiring of the probe are situated between the outer two stainless steel tubes. The middle steel tube makes sure, that the wiring does not press onto the vertical axis and also allows that the vertical axis can be removed easily for maintenance. In the bottom end of the probe's body sticks a nearly half open stainless steel turned part carrying the plastic terminal plate with screwed on soldering eyelets. The bottom ends of the wires in the probe are soldered to the eyelets on the terminal plate. At the bottom of the turned part the two axis head of the probe can be mounted centered with four screws on the outer circumference. Also at the bottom is the feed through with a PTFE bearing for the small bevel gear wheel.

In the top of the shaft body sticks an aluminum block, which carries the second stepper motor for the horizontal axis movement. Its centred bore hole is equipped with a ball bearing and a vacuum seal for the vertical axis. The stepper motor with planetary gear box is attached to an aluminium frame that can be removed easily by opening four screws. When the motor is removed the vertical axle can be rotated by hand to check for mechanical problems. The gear box axle is mechanically connected to the vertical axle by an oldham coupling. The piece of the oldham coupling clamping the vertical axle is slightly modified to increase the clamping force on the axle to avoid slipping. The vertical axis ends in a brass piece protruding about 10 mm when the axle is mounted.

3.3.3 Goniometer head

The frame of the goniometer head is built up of four stainless steel parts, a top and bottom plate and two side parts with holes and bearings for the horizontal axle. The top plate has a large centred drill hole fitting precisely onto the lower end piece of

the probe shaft. It is fixed to the probe shaft by four grub screws directed to the probe's axis. Four countersunk bolts, two for each side, connect the two side parts with the top. The same arrangement of screws through the bottom part stabilize the side pieces and make the frame rigid. An additional drill hole in the top plate is continued in one side part to take up the wiring for the probe stage. The heads of the countersunk screws would protrude the outer diameter of the goniometer head and have to be filed down to the head circumference. Therefore one has to take care not to mix up the eight screws when taking the goniometer head apart, because each screw can just be used in its original position. It should be noted, that, because the countersunk hole is cut off at the circumference of the head, there is a force perpendicular to the screw axis when the countersunk screw is tightened. This leads to a bending of the screw head, which reduces the precision of the centering of the screw and can influence the positioning of the side parts. The alignment of the side parts determines the alignment of the bearings and is therefore crucial for the movement of the horizontal axis. Worn-out screws should be replaced. It also has to be noted, that the flat inner surface of the side parts is not machined to perfectly planar, so the alignment of the side parts cannot be checked easily on the assembled frame by measuring the inner bore of the frame. Holes in the bottom plate ensure an unimpeded He gas flow to the sample stage. It is possible to mount a Hall probe in a slit at the centre of the bottom piece for probing the angular position.

The horizontal axle is made from four brass parts, the sample stage, the heater, the large bevel gear wheel and the end piece of the axle. The stage has a central drilling along the rotation axis containing the temperature sensor. Samples up to an area of $1\,\mathrm{cm}^2$ can be mounted on it. In direct neighborhood to the area reserved for the sample are two threaded holes to fix a sample holder. Four countersunk drill holes at the corners of the sample stage take up the screws to mount the heater on the side of the stage opposite the sample. The composition of heater and sample stage form the middle part of the horizontal axle. The two end pieces screwed to the two faces perpendicular to the axial direction of the sample stage fit into the bearings of the side parts of the goniometer frame. The larger end piece is a modified bevel gear with a lathed bearing shaft at its back and a centre hole for the incoming wires. The smaller end piece is a cylinder with a rim. The heater can be removed from the sample stage without unscrewing the end pieces to allow simplified maintenance. The top surface of the sample stage is lowered relative to the rotational axis to account for the typical thickness of a thin film sample substrate. A mounted thin film should lie directly in the rotational axis.

The first version of the horizontal axle was built up from three parts. The sample stage and the smaller end piece were originally machined from a single lathe piece. The arrangement of the bevel gear and the heater was basically the same. Because the machining introduces additional tension in the material, it can cause an increased bending of the sample stage with varying temperatures. The end pieces rotating in the bearings are connected to the sample stage and therefore their alignment is influenced directly by this bending. The alignment of the end pieces is crucial for a flawless movement of the horizontal axle and should depend as little as possible on the temperature during operation. To improve this situation, the second version of the sample stage was made from a cuboid brass piece that was slightly rounded at the edges. Still the surfaces had to be machined but to a far lesser extent and all working steps where done in exactly the same manner on every opposing pair of surfaces of the cuboid to preserve its symmetry. In this way the temperature induced bending of the stage could be reduced in comparison to the original design, but did not vanish completely.

Experience has shown that the horizontal axis has to move without appreciable resistance when mounted in the frame. This should also not change when the probe is cooled down. To achieve this, the horizontal axis needs a small play in the axial direction to compensate for unavoidable mechanical imperfections. After assembling the goniometer head, it is advisable to check the easy movement of the horizontal axle by hand with the probe mounted in the VTI. The very high momentum of the stepper motor with gear box would of course overcome a resistance in the movement of the axis. On the other hand such a brute force approach would probably damage parts of the probe in case of a technical failure. In the current design the momentum of the motor drive is limited by the clamping strength of the top half of the oldham coupling. It simply slips when the horizontal axis blocks mechanically. Also great care has to be taken in assembling the frame of the goniometer head. All countersunk screws should be fixed partly, one after the other in several rounds.

3.3.4 Sample holder and spring loaded contacts

For the electrical contacts of the thin film samples spring loaded contacts are used. Besides contacting the sample the spring force of the contacts holds the thin film in place. The sample holder therefore is a fixture for the spring loaded contacts, which defines the position and the spring force of the contacts. It is built up of three plastic pieces glued together by superglue forming a small bridge over the sample.

A plastic plate with drill holes for the spring contacts resides on two small plastic bars. The position of the drill holes has to fit to the contact pads of the patterned film so a sample holder can only be used fro one contact pattern. To minimize the contact resistance the height of the bars is dimensioned to achieve the maximum spring force of the spring loaded contacts. Two 2 mm diameter bore holes on each end are necessary to attach the sample holder to the sample stage.

Spring loaded contacts come in a lot of different shapes and sizes depending on the field of application like PCB (printed circuit board) test pins, battery contacts and HF test pins for IC sockets. There are two determining dimensions for choosing the spring loaded contacts, the pitch distance (distance between two adjacent contacts) and the length of the contact pin. Because of the limited room above the sample the maximum length of the contacts is $\approx$ 11 mm. The pitch distance on the thin films measured so far is 1.7 mm. This requirement rules out most of the commercially available spring contacts. Fortunately a battery contact with an outer barrel diameter of 0.86 mm and an overall uncompressed length of 9.47 mm was found. It comes with a spherical plunger tip, which is appropriate for our purpose. The barrel of the pins is thickened near the plunger end to hold the pin at a fixed height, when its back end sticks in a mounting hole and a force is applied to the plunger. The bore holes for mounting the pins were simply drilled with a 0.9 mm spiral drill in a fiberglass plastic plate. The thickness of the plastic plate should not be less than about 2 mm to avoid a sidewards tilt of the barrel.

The contact pins were stuck into the drill holes of the sample holder from the film side and the contact wires were soldered to the barrel on the film side. Solder on the barrel cannot be removed residue-free and thickens the pin shaft, so it does not fit through the sample holder bore holes. Soldering the wires on the film side made it possible to mount and remove the contact pins easily from the sample holder and reuse them on a different position. The sample is only held in place by the spring force of the contact pins.

With the sample holder mounted on the sample stage, it is not possible to rotate the horizontal axle over the full 360 °, because the mounting screws hit the small bevel gear. Therefore, just a angular range of $\approx$190 ° of the half circle opposite to the top bevel gear is usable.

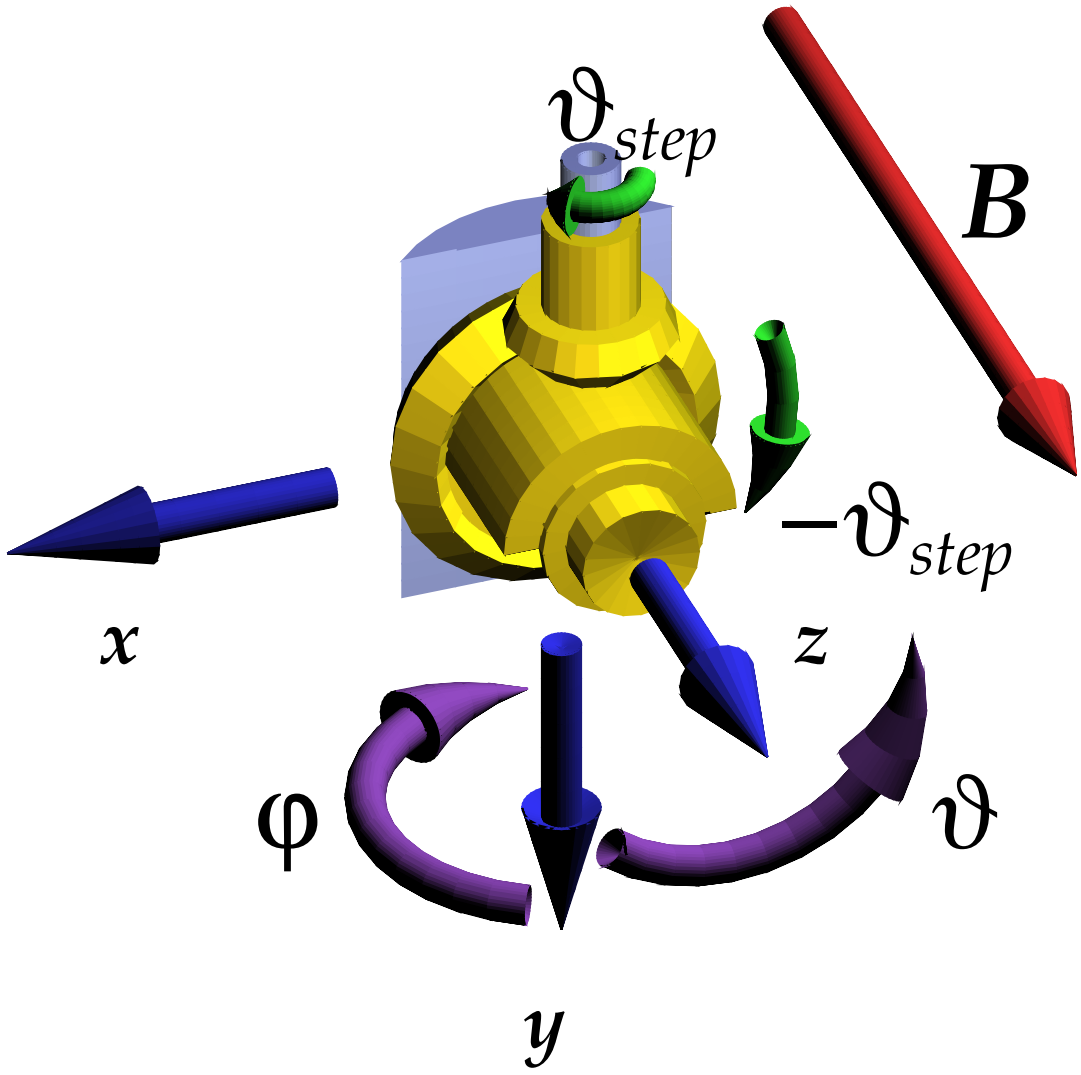

Figure 3.1: *Description of the goniometer geometry and the coordinate axes used in the text. The coordinate system xyz is attached to the the horizontal axle. The xz-plane is aligned with the sample stage.* ***B*** *points in the direction of the magnetic field.* φ *and* ϑ *show the positive rotation directions for the two goniometer axes.* φ *refers to the rotation of the whole probe and* ϑ *represents the rotation around the horizontal axis.* ϑ_{step}*, the small arrow at the top, describes the sense of rotation for an increasing stepper motor angle. This positive sense is transferred by the bevel gears to a negative one with respect to the horizontal axis as shown by -*ϑ_{step}*. The small bevel gear should symbolise the localisation of the probe's shaft. The position of the horizontal axes with the* $\hat{z}$ *axis aligned with the magnetic field corresponds to the "zero" position* $\vartheta_{\text{step}} = \vartheta_0$ *and* $\varphi_{\text{step}} = \varphi_0$*.*

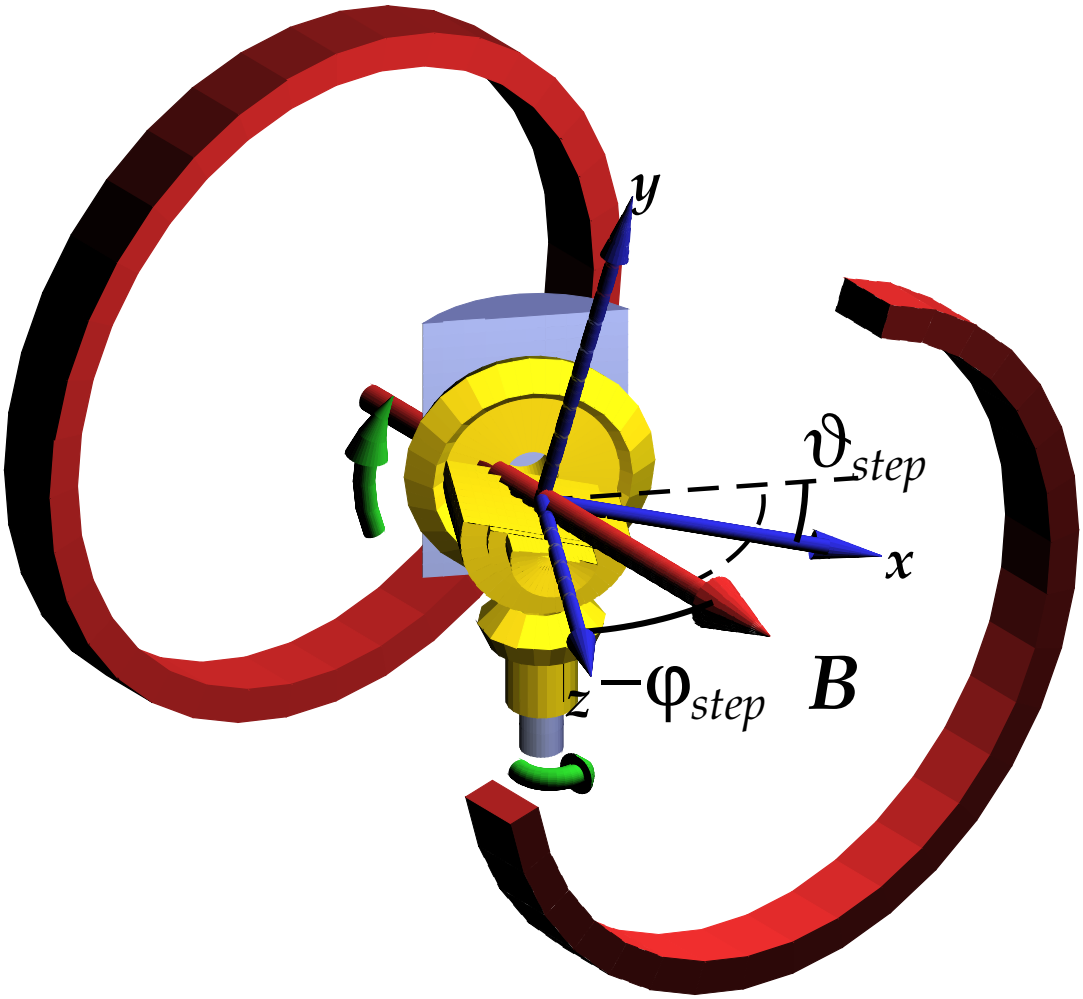

Figure 3.2: *Diagram of the angles describing the direction of the magnetic field in the coordinate system xyz attached to the horizontal axle.* ***B*** *points in the direction of the magnetic field and the two big rings should symbolise the static split coil magnet. The probe's shaft is directed to the bottom of the graph to make the sample stage visible. A positive rotation of the stepper motor for the horizontal axle leads to a positive rotation by* ϑ_{step} *of the magnetic field in the stage coordinate system. A positive rotation of the probes head appears as a negative angle* $-\varphi_{\text{step}}$ *between the z axis and the magnetic field.* φ_0 *and* ϑ_0 *are assumed to be zero here for simplicity.*

3.3.5 Goniometer geometry

The basic goniometer geometry is show in Fig. 3.1. The coordinate system is chosen in a way that the horizontal axis is aligned with the z-axis pointing away from the bevel gear and the y-axis has the same direction as the sample stage normal. The xz-plane is parallel to the sample stage surface and the y axis is directed to the bottom end of the probe. Per convention the absolute stepper motor angle of the horizontal and the vertical axle are named ϑ_{step} and φ_{step}, respectively. It should be noted, that an increasing stepper motor angle refers to a clockwise rotation of the stepper motor axle when one looks at the back of the motor. This is the positive sense of rotation regarding to the right hand rule if the motor would be enclosed by the fingers and the axle points in the direction of the thumb. In the following a positive sign of an angle always refers to a positive sense of rotation regarding the right hand rule. It follows that an increasing φ_{step} corresponds to a *negative* rotation of the magnetic field vector in the given coordinate system (see Fig. 3.2). $-\varphi_{\text{step}}$ appears as the positive angle between the magnetic field and the z-axis. The positive rotation of the ϑ_{step} axis is reversed at the bevel gear and finally results in a positive rotation of the field vector around the z axis. ϑ_{step} is the angle spanned by the x-axis and the projection of the magnetic field onto the xy-plane.

The magnetic field direction, $\hat{\boldsymbol{B}}$, at certain stepper motor angles can be written as

$$\hat{\boldsymbol{B}} = U_z(\vartheta_{\text{step}} - \vartheta_0)U_y(-\varphi_{\text{step}} + \varphi_0)\,\hat{\boldsymbol{z}}\,, \tag{3.1}$$

where U_y and U_z are orthogonal matrices describing the rotation around the y and the z axis, $\hat{\boldsymbol{z}}$ is the unit vector in z direction. ϑ_0 and φ_0 are the stepper motor angles where the magnetic field is aligned with $\hat{\boldsymbol{z}}$ and the probe's axis is aligned with $\hat{\boldsymbol{x}}$. Their values are usually not known and have to be determined by alignment measurements. For convenience, angles $\phi_{\text{stage}} = -\varphi_{\text{step}} + \varphi_0$ and $\theta_{\text{stage}} = \vartheta_{\text{step}} - \vartheta_0$ are introduced, which include the angle offsets of stepper motors. (3.1) describes a vector in sperical coordinates, where, contrary to the usual convention, ϕ_{stage} is the angle between the z axis and the vector and θ_{stage} is the angle between the x axis and the projection of the vector onto the xy plane.

The second relevant vector for transport measurements is the orientation of the track or the current direction. With the chosen coordinates this would be a vector in the xz-plane.

3.3.6 Sample alignment and goniometer inconsistencies

In general the procedure for the sample alignment depends on the sample properties and the requirements of the measurements to be performed. The method given in this section was used to check for geometrical inconsistencies of the goniometer.

It was seen already on measurements with the Hall probes incorporated in the first design that it is not possible to align the horizontal axle with the magnetic field. For no φ_{step} value the Hall voltage become independent of ϑ_{step}. This observation can be explained either by a tilt of the magnetic field relative to the VTI sample space, a tilt of the whole probe inside the VTI or a tilt between the goniometer head and the probe's shaft. The result of this tilt is, that during a rotation around the vertical axis the magnetic field vector describes a cone instead of a circular disk. As a consequence the expected $180^{\,\text{o}}$ symmetry of a sample tilted arbitrarily with respect to the sample stage is broken. A broad class of high temperature superconductors show an intrinsic pinning effect, when the magnetic field is aligned with the *ab*-plane of the mono-crystalline sample. The critical current varies usually strongly in the neighbourhood of the intrinsic pinning direction. In this geometry, already small angular deviations introduced by the goniometer or a tilt of the sample can result in observable distortions in the measured angular dependence of the critical current.

To model the expected geometrical distortions, (3.1) has to be extended to account for the additional tilt, α_{ft} of the magnetic field with respect to the sample stage:

$$\hat{\boldsymbol{B}} = U_{\text{z}}(\theta_{\text{stage}})U_{\text{y}}(\phi_{\text{stage}})U_{\text{x}}(\alpha_{\text{ft}})\,\hat{\boldsymbol{z}}\,. \tag{3.2}$$

At $\phi_{\text{stage}} = 0$ or $\varphi_{\text{step}} = \varphi_0$ the horizontal axis encloses now an angle of α_{ft} with the magnetic field direction. To keep matters simple it is still assumed, that the horizontal axis is perpendicular to the vertical axis or equivalently there is no misalignment of the goniometer head with the probe's shaft and the bearings of the horizontal axis are at the same height. For the sample position one can start with a coordinate frame, where the y axis is aligned with the sample surface normal and the x and z axes are roughly oriented like in the sample stage coordinate system. A vector valued function $\hat{\boldsymbol{B}}_{\text{samp}}(\phi_{\text{samp}},\theta_{\text{samp}})$ should describe the field direction in the sample frame of reference. The sample coordinate system is transformed into the sample stage coordinate system by two tilt angles β_{t1} and β_{t2}:

$$\hat{\boldsymbol{B}} = U_{\text{z}}(\beta_{\text{t2}})U_{\text{x}}(\beta_{\text{t1}})\,\hat{\boldsymbol{B}}_{\text{samp}}(\phi_{\text{samp}},\theta_{\text{samp}})\,. \tag{3.3}$$

Conflating (3.3) and (3.2) delivers equations for $\varphi_{\text{step}}(\phi_{\text{samp}}, \theta_{\text{samp}})$ and $\vartheta_{\text{step}}(\phi_{\text{samp}}, \theta_{\text{samp}})$ which can be used to determine the stepper motor movements for an angular measurement defined in the sample coordinate system:

$$U_z(\vartheta_{\text{step}} - \vartheta_0)U_y(-\varphi_{\text{step}} + \varphi_0)U_x(\alpha_{\text{ft}})\,\hat{\boldsymbol{z}} = U_z(\beta_{t2})U_x(\beta_{t1})\,\hat{\boldsymbol{B}}_{\text{samp}}\,. \tag{3.4}$$

One tilt of the sample can be balanced by the horizontal rotation axis, as can be seen in equation (3.4) by joining $U_z(\beta_{t2})$ with $U_z(\vartheta_{\text{step}} - \vartheta_0)$ and fusing the tilt parameter β_{t2} with ϑ_0. The rotation by β_{t2} is therefore eliminated in the following equations. A different choice for the rotations describing the sample tilt in (3.3) would not have allowed to remove β_{t2}. Because β_{t1} is expected to be a small angle, the rotation by β_{t2} and ϑ_0 (or ϑ_{step}) would still be around approximately the same axis. This would have resulted in a strong correlation of β_{t1} and ϑ_0 in the following least square fit on the Hall-voltage data, where the misorientation angles act as fitting parameters.

To describe the restriction of the field direction to a certain sample plane, one can use the scalar product of (3.2) with the normal vector of the plane tilted according to (3.3). For the zero voltage of a Hall-probe measurement, the normal vector is in the y direction, resulting in

$$0 = \left[U_z(\theta_{\text{stage}})U_y(\phi_{\text{stage}})U_x(\alpha_{\text{ft}})\,\hat{\boldsymbol{z}}\right] \cdot \left[U_x(\beta_{t1})\,\hat{\boldsymbol{y}}\right]\,. \tag{3.5}$$

To derive an explicit function for θ_{stage} in dependence of ϕ_{stage} the terms in the expanded equation (3.5) can be ordered in the general form

$$a\,\cos(\theta_{\text{stage}}) + b\,\sin(\theta_{\text{stage}}) = c\,, \tag{3.6}$$

where a, b and c are linear combinations of sines and cosines of the tilt angles in the rotational matrices. (3.6) describes the projection of a two dimensional unit vector onto the vector $(a, b)^T$. Therefore, except in the case of $c^2 = a^2 + b^2$, there are two solutions for θ_{stage} in the ϕ_{stage} interval $[-\pi, \pi]$ (assuming the arctan function applied is aware of the quadrant its arguments lie in)

$$\tan(\theta_{\text{stage}})_{1,2} = \frac{b\,c \pm a\sqrt{a^2 + b^2 - c^2}}{a\,c \mp b\sqrt{a^2 + b^2 - c^2}} \quad \text{where } c \leq \sqrt{a^2 + b^2} \tag{3.7}$$

and between θ_{stage} for solution 1 (2) at a certain c and the angle of solution 2 (1) for

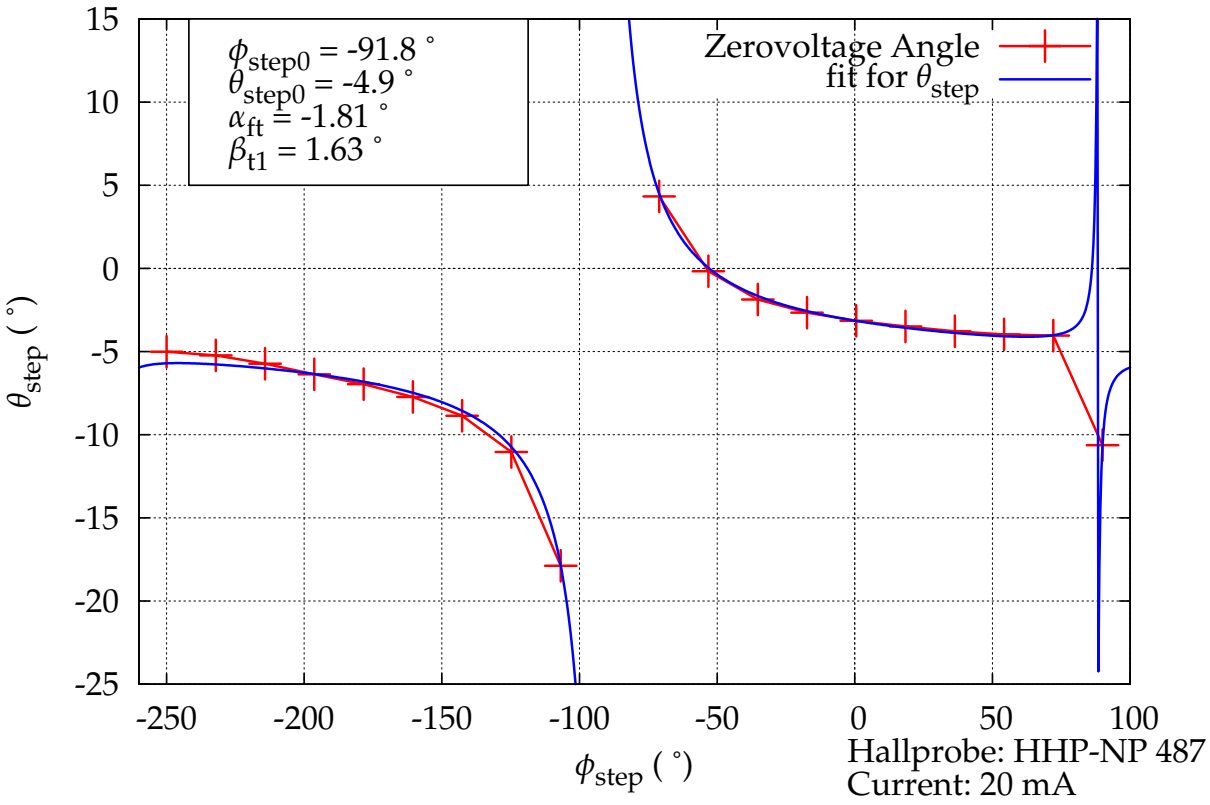

Figure 3.3: *Example for a fit of the calculated field rotation in a declined sample plane after (3.5). The data is measured with a Hall probe mounted on the sample stage. At several φ_{step} positions ϑ_{step} was rotated from $-30°$ to $+30°$ and the Hall voltage was recorded. The data points represent the ϑ_{step} values, where the Hall voltage is zero (without zero field voltage correction).*

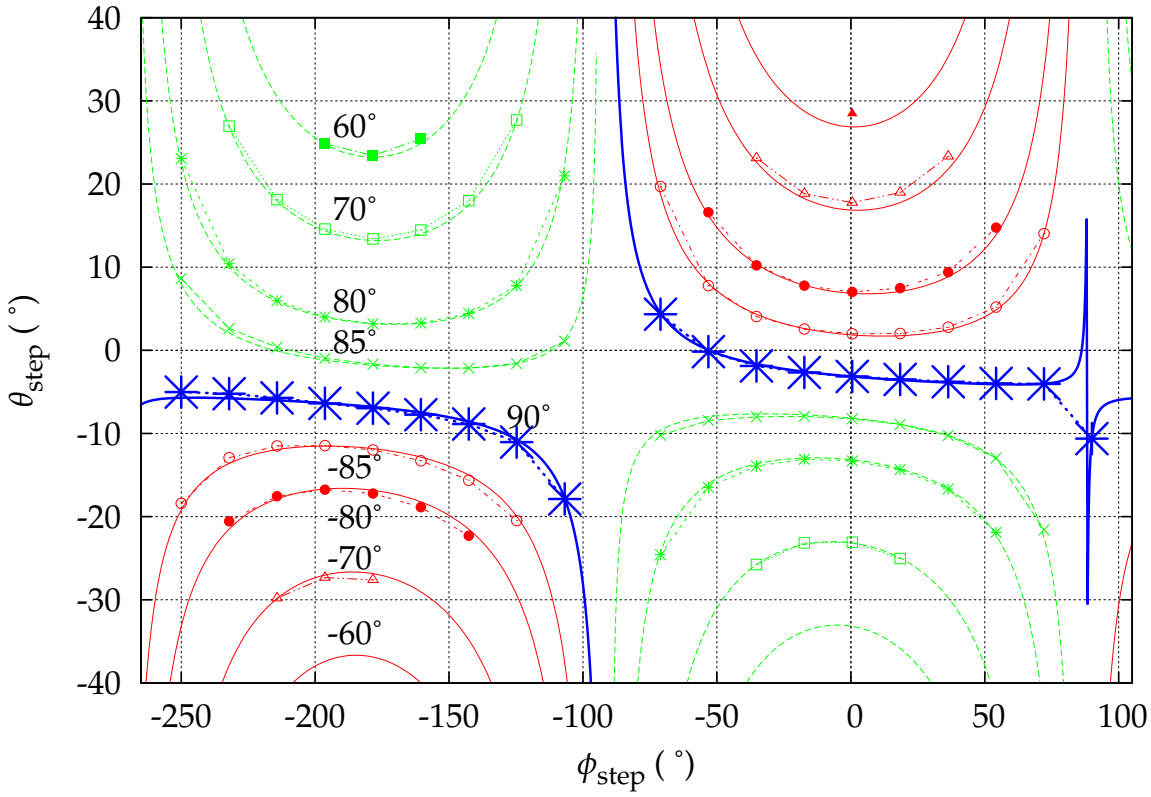

Figure 3.4: *The final result of the fit of the calculated field rotation against Hall probe data. The model described by (3.2) was refined to account also for a tilt of the horizontal rotation axis by an angle α_{at}. The graph is plotted with $\alpha_{at} = 0.43°$. Besides the zero Hall voltage data used for fitting (bold lines) it contains additional curves for field rotations at a constant angle between the field vector and the sample normal. This angle is given as a parameter. The curves with symbols are evaluated at a constant voltage corresponding to the field-normal angles from the same Hall measurement, where also the zero voltage points are taken from. The curves without symbols are calculated from the model simply by setting the left hand side of the modified equation (3.5) to the cosine of the angle between the sample normal and the field vector.*

$-c$ is a difference of 180 °. Solutions appropriate for our geometry are achieved by

$$\theta_{\text{stage}} = \begin{cases} \theta_{\text{stage}_1} & \text{for} \quad \phi_{\text{stage}} > 0\,, \\ \theta_{\text{stage}_2} & \text{for} \quad \phi_{\text{stage}} < 0\,, \\ 0 & \text{for} \quad \phi_{\text{stage}} = 0\,. \end{cases} \tag{3.8}$$

ϕ_{stage} has to be restricted to the interval $[-\pi, \pi]$, which can be achieved by a periodic sawtooth function

$$\phi_{\text{stage}} = \begin{cases} ((|\phi'_{\text{stage}}| + \pi) \bmod 2\pi) - \pi & \text{for} \quad \phi'_{\text{stage}} > 0\,, \\ \pi - ((|\phi'_{\text{stage}}| + \pi) \bmod 2\pi) & \text{for} \quad \phi'_{\text{stage}} < 0\,. \end{cases} \tag{3.9}$$

As an example Figure 3.3 shows the fit of the derived $\vartheta_{\text{step}}(\varphi_{\text{step}},\varphi_0,\vartheta_0,\alpha_{\text{ft}},\beta_{\text{t1}})$ function against data measured with a Hall probe (HHP-NP, sensitivity 178.8 mV/T at 100 mA) mounted at the sample stage. The Hall probe current was 20 mA, the field was 1 T and the temperature was not controlled. At several φ_{step} positions ϑ_{step} was rotated from $-30\,^{\text{o}}$ to $+30\,^{\text{o}}$ and the Hall voltage was recorded. Without any tilts, one would expect a constant Hall voltage for $\varphi_{\text{step}} = \varphi_0$ in this geometry.

The data points represent the ϑ_{step} values, where the Hall voltage is zero (without zero field voltage correction). The measured curve reproduces the distorted arctan shape expected from the model. All four parameters are necessary to achieve this fit.

The fit in Figure 3.3 is slightly better for $\theta_{\text{stage}} > 0$ than for the negative half circle. This suggests that another deviation from the ideal goniometer is not included in the model yet. A plausible choice introducing a different kind of distortion would be a tilt of the horizontal rotation axis relative to the vertical axis by an angle α_{at}. To test the effect of this tilt $U_{\text{z}}(\theta_{\text{stage}})$ in (3.2) was replaced by $U_{\text{x}}(\alpha_{\text{at}})U_{\text{z}}(\theta_{\text{stage}})U_{\text{x}}(-\alpha_{\text{at}})$. This modification only tilts the horizontal rotation axis and not the whole horizontal axle with the sample stage and the sample. The declination of the sample normal is still only covered by β_{t1}. The attempt to fit the data of Fig. 3.3 with the refined model was only partly successful. A fit with a full set of parameters leads to unreasonably large values of α_{at} the order of $10\,^{\text{o}}$. On the other hand testing the effect of small values of α_{at} on the fitted function with the parameter set of Fig. 3.3 shows at least a slight improvement. A least square fit with the parameter α_{at} alone and keeping all other parameters constant gives a value for α_{at} of $0.43\,^{\text{o}}$.

The final result including α_{at} is shown in Fig. 3.4. Besides the zero Hall voltage data used for fitting it contains additional curves for field rotations at the given angles between the field vector and the sample normal. The lines with symbols are

evaluated at a constant voltage corresponding to the field-normal angles from the same Hall measurement, where also the zero voltage points are taken from. The lines without symbols are calculated from the model simply by setting the left hand side of equation (3.5) to the cosine of the angle between the sample normal and the field vector.

3.3.7 Wiring

In the original design the current wires were pairwise twisted varnish coated copper wires. After about half a year of operation of the probe the lacquer insulation of these wires became brittle resulting in a high resistance electrical connection (of the order of MΩ) to the probe's shaft. The current wires were replaced by twisted standard electronic PTFE coated wires.

The wiring between the soldering tags on the bottom terminal plate of the probe to the devices inside the goniometer head needed some additional considerations. The first approach to protect them from abrasion on metal corners and to give the bundle of wires some guidance consisted of putting the wires into a shrink tubing. This attempt was not successful. The varnish coating became brittle due to the movement, the partly small bending radius required, and because of thermal stress. Assuming that wires with lacquer insulation will not be very durable under these circumstances, a quick and easy replacement of the wiring between the terminal plate and the horizontal axle was desirable. Therefore a second terminal board fixed to the horizontal axis was introduced, where all the devices in the axle were connected to. Only the wiring between the two terminals is affected by the relative movement and should be replaceable.

The advantage of lacquer insulation is that it is space saving and also very thin and flexible copper wires are available. Stranded wires were considered to take up too much space. Experience showed, that a copper wire with a diameter of 50 μm is not vulnerable to the permanent motion during the operation of the probe. It is used for all voltage and for low current leads, like the current supply for the Hall probes and the temperature sensor. The sample current and the heater supply wires are made from three to four 100 μm copper wires braided together. All voltage and current leads are pairwise twisted. The final bundle of wires is still quite thin and fits easily into the wire channel of the probe head. For further protection it is led through a PTFE hose down to the height of the horizontal rotational axis. Before the wires enter the probe's sample space they are wound several times to a loose spiral

and put between two plastic discs. The spiral compensates for the rotation motion of the axle. From there the wire bundle goes through a hole in the inner plastic disc and enters the sample space of the probe with the second terminal plate. Some experimentation was necessary to set this wiring up, but it now works quite reliably and is surprisingly durable.

The described wiring scheme breaks the concept of the direct voltage wires from the sample to the voltmeter. The experimental practice showed that it is desirable to have the possibility of shorting the sample without unplugging the voltage or the current lines when no measurements are performed. In the first approach the low temperature coax was directly connected to the nanovoltmeter plug, so this was not possible for the voltage wires. This was changed after some time, so that also the voltage coax where plugged into a simple switch box with BNC connectors. The voltage noise did not increase in comparison to the direct connection.

3.3.8 Stepper motors

The driving motors are two equal standard stepper motors (full step 1.8 °) with 45.56 : 1 planetary gears providing high momentum. Including an additional 2 : 1 reduction for each drive given by the toothed belt transfer and the bevel gears the resulting angular resolution is lower than 0.02 ° per full step. The motors are attached to two ETM245 micro stepping controllers working in a 1/8 step mode increasing this theoretical resolution down to $\approx$ 0.0025 ° per rising edge of the step signal. The EMT245 are interfaced to the standard parallel port of a PC by a self made stepping motor control unit.

3.3.9 Sample heater

The sample heater is made from a resistance wire loop twisted together and wound up as small as possible that it fits into the brass heater housing of the probe. After putting the wire into the housing it is filled up with a highly temperature conducting glue taking care to get an even contact surface on the open side. Care has to be taken not to scratch the varnish insulation of the wire when putting it into the housing. In the currently used heater, the heater wire had a diameter of 0.19 mm and a resistance of 33.5 Ω/m. With a starting length of $\approx$ 1.2 m a heater resistance of 40 Ω was achieved. The heater was controlled by a second ITC4 Oxford Instruments temperature controller, where the maximum output voltage was limited to 6 V. The

maximum heater power was therefore 0.9 W.

3.3.10 Electrical grounding

The grounding in the measurement setup is based on the protection earth (PE) of the wall plug. An extra grounding point was available at the site of the setup, but it seemed to be spoiled by some characteristic noise of unknown source and was therefore not used as a separate measurement ground.

The instrumentation rig is grounded by the metal housings of the 150 A and the 25 A current supplies. All digital ground lines of a personal computer (PC) are directly connected to the protection earth of these devices. Also the IEEE interface and the digital and analog output cards in the measurement PC, employed to control the measurement instrumentation, do not offer a separate zero volt signal ground. It is common practice to avoid ground loops to keep the ground lines free from voltages induced by varying magnetic fields emitted from practically all electrical devices. The ground wiring has therefore usually a star like topology starting at one or more well defined grounding points. In the current setup this concept could not be realised with the IEEE devices, because (besides their supply cables) the shielding of the IEEE cables introduces a second connection to PE over the PC housing. Instrumentation designed for measurement purposes usually separate the internal electronics strictly from protection earth and leave the grounding to PE as a user option. Therefore, it should be possible to keep the grounding loops out of the measurement circuit. For all other shielded cables inside the probe, between the probe, the rig and the control computer the shielding is always just contacted on one end. Especially ready made computer cables should be checked for their shielding connections before they are used in the measurement setup. On the side of the rig an electrically isolated copper bar was mounted to serve as a central grounding point, where the source of the ground line can be chosen according to the need of the operator.

For some time it was also tried to use a separation transformer to hold off disturbances from the main lines. The available separation transformer was specified for a power of $\approx$ 800 W, which is not sufficient for the whole setup. It was decided to connect only the current sources used for the very sensitive low current thin film samples to the transformer. IEEE devices were not powered by the transformer because they would have brought the already mentioned ground loops built up by the IEEE cable shieldings directly into the measurement circuit. The main disadvantage of this approach was, that it was necessary to have a low ohmic ground connection

in the measurement circuit. Because of this and the questionable protective value of the separation transformer it was removed from the setup after some time.

Currently the measurement circuit is not grounded at all. It can be connected to PE by a 1 MΩ resistor, but this did not seem necessary up to now. When the current source and the nanovoltmeter are connected to the sample, it is not possible to touch any wire of the measurement circuit directly. This is considered to be important to avoid voltage peaks on the measurement wires due to electrostatic discharges by touching the cryostat or the measurement rig which easily can damage a thin film sample.

3.3.11 Bearings

In the original design no special bearings for the moving parts in the goniometer head were provided. The smaller brass end piece of the horizontal axle and the smaller brass bevel gear were running directly on the stainless steel bore hole of the frame and the stainless steel bottom end part of the probe shaft. Brass is softer than stainless steel and should therefore deliver some dry lubrication for the bearing. Because of the relatively small diameter of the rotating part the difference in thermal expansion was considered not to be a problem. Only the large bevel gear was guided by a brass ring set into the side part of the goniometer frame because of its larger diameter.

In the first design the horizontal axis was blocking from time to time. To resolve this problem it was tried to use PTFE inserts in the stainless steel parts and to replace the brass ring by a PTFE ring. The brass parts were now running on softer PTFE bearings instead of stainless steel. It turned out that this did not solve the problem at all, but also did not make things worse, so the PTFE bearing were left on their place. Only the PTFE ring for the large bevel gear was exchanged by the previously used brass ring.

3.3.12 Hall probes

In the first design it was planned to equip the goniometer head with two Hall probes, one for each rotation axis. They should give at least an approximate feedback of the current position of the probe. This was desirable because especially the position of the horizontal axle cannot be checked from outside, when the probe is mounted in the VTI. This approach did not work well, because it complicated the operation

and maintenance of the probe. The main reason was the increased number of wires required for the Hall probes. A failure in the wiring of the goniometer head became more probable. The Hall probe for the horizontal axle was situated in the same housing as the heater, thus reducing the available volume for the heater and made the installation or replacement of the heater wire far more difficult. Finally, the only positional information one is interested in refers to the sample and therefore usually the measurements on the sample deliver the positional feedback anyway.

3.3.13 Measurement program

The original measurement program written for the high current probe was a simple sequencer. It allowed to define a sequence of predefined commands. Every command could be customized by a fixed set of constant parameters. The program was written in the C programming language and run under the DOS operating system.

It was considered to be easier to extend the existing program and to adopt it for the new probe. To use this program with the new probe, a new software module to access the stepper motor controller was necessary. This module features (not too accurate) software controlled stepper motor frequency with ramping at start and end of the motion, single and concurrent drive of the motors, automatic backlash correction, software limits for minimal and maximal angles and reading out of the end limit switches. Because the stepper motor control unit does not store the current angular positions of the motors, all bookkeeping has to done by the PC. To reduce the risk of loosing the current state of the stepper-motors due to unpredictable program crashes the data is written to the hard-disk after every change of stepper angles.

The original concept of a simple sequencer leads to very long sequences especially for angular measurements. These sequences were tedious to write and, because of the constant command parameters, could not be easily reused for different samples. Therefore, the sequencer was subsequently modified and extended, finally resulting in an interpreted programming language. The major extensions were the introduction of variables, preprocessed command arguments containing mathematical expressions and string operations, a loop command and conditionals to influence the program flow and functions for grouping commands together under a new name. Also some commands for a direct access of the IEEE interface, the serial port, the digital and the analog output boards and the servo motor controller were added. This made it possible to implement the software interfaces for devices in the measurement setup directly in the new programming language without modifications on the

C source code, which simplifies the incorporation of new devices in the setup.

3.4 Measurement setup

The main parts of the setup are a He gas flow cryostat with a split coil magnet, an experimental rig containing the measurement electronics and a standard PC for process control. The split coil magnet is situated in the He bath of the cryostat and delivers a horizontal magnetic field of up to 6 T. It is driven by an Oxford Instruments magnet power supply IPS 120-10. The variable temperature insert (VTI) in the magnet is supplied with a strong heater and allows sample temperatures from $\approx$ 3 K to more than 300 K. The inner diameter of the sample space is about 30 mm and the temperature is set by an Oxford Instruments ITC 503 temperature controller. Four externally programmable current supplies are available for the sample current, EA-PS 150 A, Heinzinger 25 A, Heinzinger 1 A (each with analog 0–10 V inputs) and a Keithley 224 with a maximal output current of 100 mA programmed over its IEEE interface. For constant sample currents up to 150 mA a Knick precision current source can be used. The sample voltage is measured with a Keithley 182 nanovoltmeter and all other voltage sources like He level-meter, the voltage on the sample current shunt or the voltage of the sample temperature sensor, are read out by a digital multimeter Keithley 199 with an eight channel scanner. A second Oxford Instruments ITC 4 temperature controller can be used for reading or even controlling the sample temperature alternatively. Two precision resistors, one with 1 Ω@1 W and one with 0.01 Ω@70 W are available as sample current shunt resistors. The Heinzinger 1 A current supply has a high electromagnetic emission level (no grounded housing) and must not be placed near the nanovoltmeter.

Besides its standard interfaces the process control PC is equipped with an IEEE card, an Burr Brown PCI carrier board and an DMC400 servo motor controller (one axis, high current probe). Via the PCI board the PC can deliver two 12 Bit analog output voltages (unfortunately grounded) and 16 digital in- and output channels. Voltmeters, magnet power supply, ITC 503 and the Keithley 224 current source are connected to the IEEE bus interface. The ITC4 communicates over the serial RS232 line and the stepper motor controller is attached to the parallel port. The analog output voltages can be used freely to program sample power supplies and are made ground free by a (self built) separation amplifier.

Bibliography

[1] P. Berghuis, R. Herzog, R. E. Somekh, J. E. Evetts, R. A. Doyle, F. Baudenbacher, and A. M. Campbell. Current-voltage measurements as a probe of the activation barriers for flux creep in thin films of $YBa_2Cu_3O_{7-\delta}$. *Physica C*, 256:13, June 1996.

[2] G. Blatter, M. V. Feigel'man, V. B. Geshkenbein, A. I. Larkin, and V. M. Vinokur. Vortices in high-temperature superconductors. *Reviews of Modern Physics*, 66:1126, October 1994.

[3] E. H. Brandt. Large range of validity of linear elasticity of the vortex lattice in high-T_c superconductors. *Physical Review Letters*, 69:1105, August 1992.

[4] E. H. Brandt. The flux-line lattice in superconductors. *Reports on Progress in Physics*, 58:1465, June 1995.

[5] E. H. Brandt, John R. Clem, and D. G. Walmsley. Flux-line cutting in type II superconductors. *Journal of Low Temperature Physics*, 37:43, March 1979.

[6] L. Bulaevskii and J. R. Clem. Vortex lattice of highly anisotropic layered superconductors in strong, parallel magnetic fields. *Physical Review B*, 44:10243, November 1991.

[7] L. N. Bulaevskii, M. Levij, and V. G. Kogan. Vortices in layered superconductors with Josephson coupling. *Physical Review B*, 46:366, July 1992.

[8] A. Diaz, L. Mechin, P. Berghuis, and J. E. Evetts. Evidence for vortex pinning by dislocations in $YBa_2Cu_3O_{7-\delta}$ low-angle grain boundaries. *Physical Review Letters*, 80:3855, April 1998.

[9] A. Diaz, L. Mechin, P. Berghuis, and J. E. Evetts. Observation of viscous flux flow in $YBa_2Cu_3O_{7-\delta}$ low-angle grain boundaries. *Physical Review B*, 58:R2960, August 1998.

[10] D. Dimos, P. Chaudhari, J. Mannhart, and F. K. LeGoues. Orientation dependence of grain-boundary critical currents in $YBa_2Cu_3O_{7-\delta}$ bicrystals. *Physical Review Letters*, 61:219, July 1988.

[11] J. H. Durrell. *Critical Current Anisotropy in High Temperature Superconductors*. PhD thesis, University of Cambridge, 2001.

[12] J. H. Durrell, M. J. Hogg, F. Kahlmann, Z. H. Barber, M. G. Blamire, and J. E. Evetts. Critical current of $YBa_2Cu_3O_{7-\delta}$ low-angle grain boundaries. *Physical Review Letters*, 90(24):247006–1, 2003.

[13] D. Feinberg. Vortex lines in layered superconductors: I: From 3d to 2d behaviour. *J. Physique III*, 4:169, 1994.

[14] A. Gurevich. Nonlocal Josephson electrodynamics and pinning in superconductors. *Physical Review B*, 46:3187, August 1992.

[15] A. Gurevich and E. A. Pashitskii. Current transport through low-angle grain boundaries in high-temperature superconductors. *Physical Review B*, 57:13878, June 1998.

[16] R. Herzog and J. E. Evetts. *Review of Scientific Instruments*, 65:3574, 1994.

[17] H. Hilgenkamp and J. Mannhart. Grain boundaries in high-T_c superconductors. *Reviews of Modern Physics*, 74:485, May 2002.

[18] P. H. Kes, J. Aarts, V. M. Vinokur, and C. J. van der Beek. Dissipation in highly anisotropic superconductors. *Physical Review Letters*, 64:1063, February 1990.

[19] A. E. Koshelev. Kink walls and critical behaviour of magnetization near the lock-in transition in layered superconductors. *Physical Review B*, 48:1180, July 1993.

[20] A. E. Koshelev. Vortex-chain phase in layered superconductors. *Physical Review B*, 71:174507, May 2005.

[21] E. Pardo, J. H. Durrell, and M. G. Blamire. Vortex deformation and breaking in superconductors: a microscopic description. *Philosophical Magazine*, 87:4359, October 2007.

[22] E. V. Thuneberg, J. Kurkijärvi, and D. Rainer. Pinning of a vortex line to a small defect in superconductors. *Physical Review Letters*, 48:1853, June 1982.

[23] M. Tinkham. *Introduction to superconductivity*. McGraw-Hill, 2nd. edition, 1996.

[24] U. Welp, W. K. Kwok, G. W. Crabtree, K. G. Vandervoort, and J. Z. Liu. Magnetic measurements of the upper critical field of $YBa_2Cu_3O_{7-\delta}$ single crystals. *Physical Review Letters*, 62:1908, April 1989.

Curriculum vitae

Personal data

Name: DI Karl Robert Schöppl

Address: Margaretengürtel 6/19
1050 Vienna
Austria

Affiliation: Vienna University of Technology
Atomic Institute of the Austrian Universities
Low Temperature Physics/Supercondutivity
1020 Vienna

Date of birth: 7th March 1973

Nationality: Austria

Education

1987–1992 Technical School for Electronics and Information Technology ("Höhere Technische Bundeslehranstalt"), Braunau/Inn.

1993–2002 Johannes Kepler University Linz
M. Sc. in Technical Physics, Thesis on *Pulsed Laser Deposition of c-axis oriented and polycrystalline YBCO– and STO layers* ("Laserabscheidung von c-achsenorientierten und polykristallinen YBCO– und STO Schichten").

2002–present Vienna University of Technology
Ph. D., *Grain Boundaries in High Temperature Superconductors.*

List of publications

- Schöppl K. R., Weber H. W., Durrell J. H.
  Angular dependence fo critical currents in $YBa_2Cu_3O_{7-\delta}$ vicinal films
  Journal of Physics: Conference Series **97** 012225 (2008)

- Schöppl K. R., Weber H. W., Durrell J. H.
  Angular dependence of critical currents across $YBa_2Cu_3O_{7-\delta}$ low angle grain boundaries
  Physica C **460** 1188 (2007)

- Eisterer M., Müller R., Schöppl R., Weber H. W., Soltanian S., Dou S. X.
  Universal influence of disorder on MgB_2 wires
  Supercond. Sci. Technol. **20** 117 (2007)

- Eisterer M., Schöppl K. R., Weber H. W., Sumption M. D., Bhatia M.
  Neutron Irradiation of SiC Doped and Magnesium Rich MgB_2 Wires
  IEEE Transactions on Appl. Supercond. **17** 2814 (2007)

- Kühberger M., Gritzner G., Schöppl K. R., Weber H. W., Olsen A. A. F., Johansen T. H.
  Preparation and characterization of superconducting MgB_2 films on alumina
  Supercond. Sci. Technol. **17** 764 (2004)

- Delamare M. P., Schöppl K. R., Pedarnig J. D., Bauerle D.
  Influence of $(Y_{0.8}Ca_{0.2})Ba_2Cu_3O_{7-\delta}$ top layer on the transport properties of a-axis oriented $YBa_2Cu_3O_{7-\delta}$ thin films
  Physica C **372** 638 (2002)